Forschungszentrum Jülich

Institut für Werkstoffe der Energietechnik

Loading Characteristics of the Material Interface in Brazed Divertor Joint Components under Fusion Relevant Thermal Loads

J.-H. You

Jül-3345

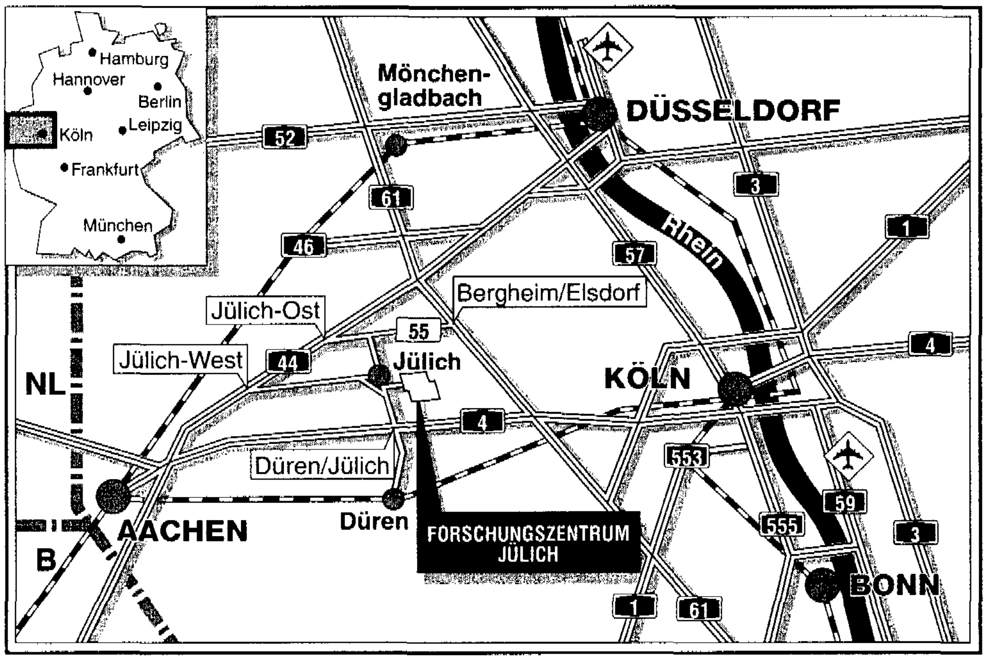

Berichte des Forschungszentrums Jülich ; 3345
ISSN 0944-2952
Institut für Werkstoffe der Energietechnik Jül-3345

Zu beziehen durch: Forschungszentrum Jülich GmbH · Zentralbibliothek
D-52425 Jülich · Bundesrepublik Deutschland
☎ 02461/61-6102 · Telefax: 02461/61-6103 · e-mail: zb-publikation@fz-juelich.de

Forschungszentrum Jülich

Jül-3345
January 1997
ISSN 0944-2952

Loading Characteristics of the Material Interface in Brazed Divertor Joint Components under Fusion Relevant Thermal Loads

J.-H. You

English version report Jül-3286 (Sept 1996)

Content

Chapter 4. Plastic deformation of the ductile braze layer in a CFC/TZM bond joint under cyclic thermal loads................................54

Chapter 5. Thermomechanical behavior of actively cooled, brazed divertor components under cyclic high heat flux loads..82

Appendix

Chapter 1. Introduction

1. Divertor components

ITER is a future tokamak fusion device which is being designed with a burn time of about 1000 seconds generating fusion power in the range of 1500 MW [1].
A divertor is an in-vessel component of ITER for power exhaust, impurity control, He and hydrogen pumping [2,3].

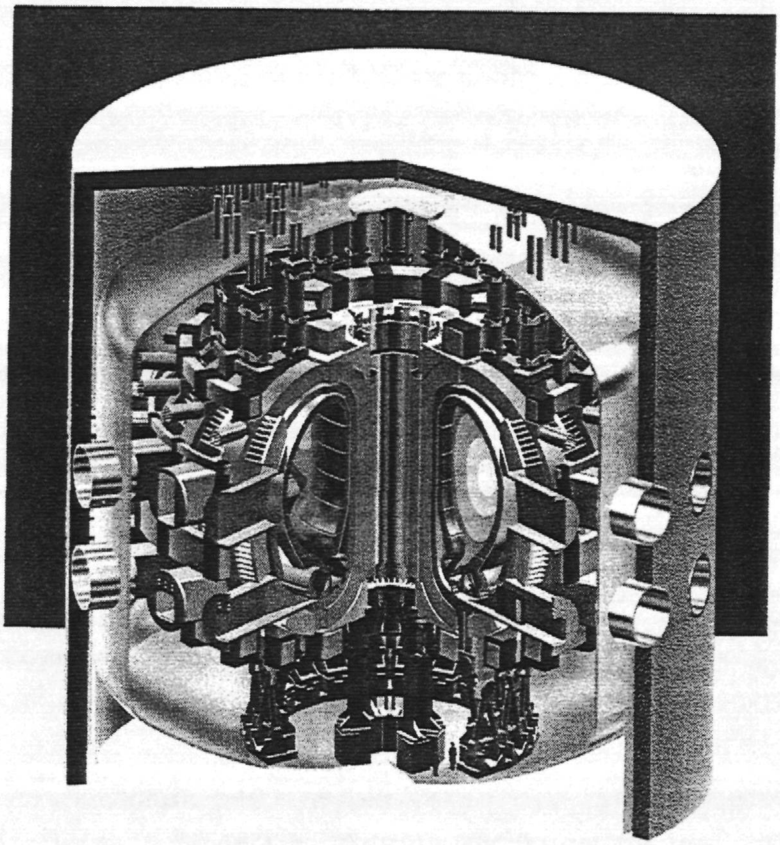

Fig. 1.1. Structure of the international thermonuclear experimental reactor (ITER).

Plasma facing and heat removing are two main functions of a divertor component during fusion operation.
The particle bombardment will result in an energy transfer in form of charged particles and neutrals flux onto the divertor plate. Divertor components experience severe thermal loads during pulsed operations. During normal operations, the resulting peak heat flux on the divertor plate in ITER EDA phase is expected to reach 5 MW/m^2. During power excursions, saw tooth collapses or so called ELMs, maximum heat loads up to 20 MW/m^2 may occur.

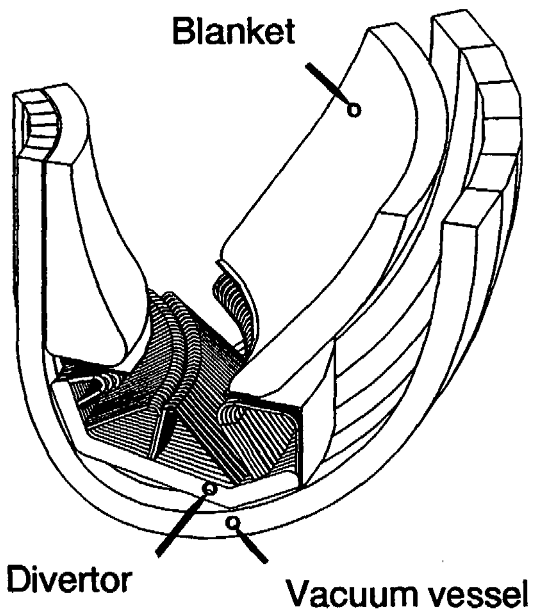

Fig. 1.2. Schematic view of the divertor plate in ITER.

The dual performance condition for divertor components gives rise to various material requirements which can be hardly met in a monolithic material [4,5].
The plasma facing materials should fullfill some plasma compatibility requirements to reduce the degradation of the plasma fuel: low atomic number and low sputtering yield. Further material issues are: high thermal conductivity, low tritium inventory, superior thermal shock resistance, easy fabrication and sufficient mechanical strength even after irradiation [6,7].
CFCs, SiC composites and graphite materials have been considered as a candidate material for plasma facing components. However, their structural reliability has been limited due to low structural toughness.

The duplex material configuration where plasma facing armor tiles are brazed onto the metallic cooling body has been the preferred design concept for divertor geometries due to their flexibility to fullfil the needed material properties [8,9]. This duplex structure is one of the candidate design concepts for ITER.
With this configuration the divertor plate can meet basic material requirements which are hardly satisfied in a monolithic material.
The duplex structure enables the divertors perform dual functions during the high heat flux (HHF) operation. The target material withstands the particle bombardment and heat flux without serious plasma contamination whereas the metallic body support the coolant tubes and transfer the heat from the tiles to the heat sink maintaining reasonable surface peak temperatures.

In Fig.1.3, a typical bonded structure of a divertor test module is shown. To maintain the constant surface temperature, active cooling systems are introduced in the metallic body.

This structure results in an almost one dimensional steady state heat flow during normal operations and then the temperature profile will be nearly bi-linear [8,10].

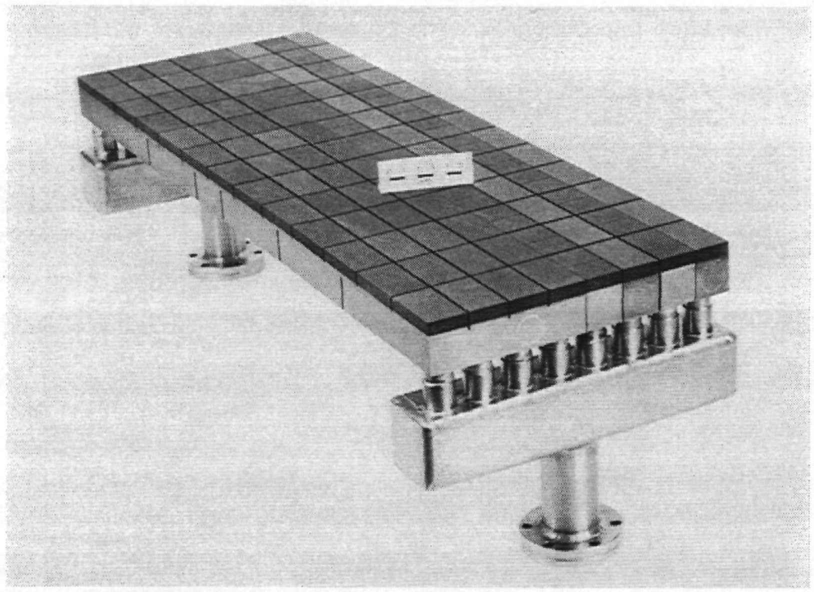

Fig. 1.3. A divertor test module. The component is a joint structure consisting of armor tiles brazed on the metallic heat sink.

2. Structural integrity problems

Due to the severe temperature gradient and the mismatch of the thermal expansion coefficients, significant thermal stresses can be generated in the actively cooled, brazed divertor structures during fusion operations. The structural integrity of the duplex divertor components should be confirmed to be applied to cyclic HHF operation.
It has been reported from many of the thermal loading experiments conducted on bond joints that most failures occur near or at the interface of the joints [11-16].

The stress level at the material interface is higher than that of other bulk regions and the stress components increase rapidly near the free surface edge of the interface [17,18].
The stress intensification near the free surface edge of the interface shows singularities for certain material combinations and wedge angle geometries [19-21].

The strength of these stress singularities is affected strongly by the Dundurs parameters which are combinations of elastic constants whereas the bulk stresses are mainly caused by the misfit of the thermal expansion coefficients [22,23].
The stress states near the singularities can be the most dominant factors which determine the fracture strength behavior of brazed components under thermal loads [18].
The stress intensification near the free surface edge of the interface may develop even during the brazing process. The strength of the joint is mostly influenced by the residual stress fields near the interface edge.

When the material is brittle, cracks initiate often in this region leading to structural failure. On the other hand, the interface of a joint can be also debonded by propagation and linking of preexisting cracks. The preexisting cracks may originate from intact joining faults. In this case, the crack propagation is driven by the singular stress concentration near the crack tip. Hence the singular stress fields occuring in the bond interface and their further evolution are significant to understand the thermomechanical behavior of the divertor joint component and to assess the failure criterion for the component [14,18].

When the stress singularity exists, the strength of the singularity is represented by the exponent of singularity. This parameter can be determined analytically [24-29].
In general, the stress state in the bulk of the divertor components is affected by the free edge effect due to the finite dimension.
On the other hand, the stress solution near the singularity in a finite body should also satisfy the far field boundary conditions [30].

It is useful to introduce the fracture mechanical parameter which relates boundary conditions to the resultant stress solutions. Stress intensity factors can be taken as such a representative quantity which describes the asymptotic stress fields near the free surface edge of the interface or near the crack tips in the interface [20,30].
While the exponent of singularity remains constant for a given material combination and wedge geometry, the stress intensity factor can represent the evolution of transient thermomechanical response.
A failure criterion can be provided from this parameter for a specific thermal load condition.

During the brazing process, as the materials are cooled from the brazing temperature to room temperature, residual stresses may develop [18]. When the brazed joint is subjected to additional thermal loads, the resulting thermal stresses will be superposed onto the residual stress fields.

In fabricating the brazed joint, ductile metallic foils are used as a braze. The thermal stresses in a bi-material joint system are relieved by introducing a ductile braze interlayer into the interface. Since this effect originates from the strain energy dissipation in the braze metal which undergoes plastic deformation, the stress state near the interface depends directly on the yield behavior and work hardening rate of the filler metal [31].

Informations on the stress, or strain amplitude of the structure under a cyclic thermal loading are important to predict the structural lifetime.
For a elasto-plastic material system, the stress evolution is related to the integral load path. Thus, to estimate the current stress and its amplitude, full loading history should be simulated with a proper constitutive model and detailed material data. The resultant stress level at any point of the load path affects the joint strength.
Since the most failures in brazed joints occur in or near the material interface, the interfacial stress field has a decisive effect on the fracture strength of the joint [18].

One of the main damages of the divertor joint structures is the thermomechanical fatigue, which is a characteristic feature of pulsed operation in tokamak fusion devices [8]. The thermally induced fatigue is a important issue related to the long term lifetime [32,33].
When the material is brittle or the strength of the bond interface is not sufficient, thermal stress may lead to abrupt failure of the joint structures [34].

Since the available database on interfacial toughness and fatigue behavior of candidate materials is poor, it is necessary to simulate the high heat flux (HHF) fatigue conditions by experiments to assess structural integrity, to characterize the overall thermal response, and to determine the critical heat fluxes.

In investigating the overall thermomechanical performance, it is also of importance to analyze the static thermal stress fields for the load conditions under consideration.
When the thermal load varies periodically with time, the corresponding stress changes can result in fatigue damage. In this case, the stress amplitude and the maximum stress level are the critical factors affecting the fatigue lifetime of the structures.
In addition, the mean stress value and the mode of the stress change have some influences on the fatigue behavior [35,36].

3. Reference

[1] P.-H. Rebut, Proc. 18th SOFT (Karlsruhe, FRG, 1994), Fus. Eng. Des. 30 (1995), pp. 85-118

[2] K.J. Dietz, S. Chiocchio, A. Antipenkov, G. Federici, G. Janeschitz, E. Martin, R.R. Parker, R. Tivey, Proc. ISFNT-3 (Los Angeles, CA, USA, 1994), Fus. Eng. Des. 27 (1995) Part A, pp. 96-108

[3] ITER Joint Central Team, Proc. ICFRM-6 (Stresa, Lago Maggiore, Italy, 1993), J. Nucl. Mater., 212-215 (1994), Part A, pp.3-10

[4] R.F. Mattas, D.L. Smith, C.H. Wu, T. Kuroda, G. Shatalov, Proc. ICFRM-5 (Clearwater, FL, USA, 1991), J. Nucl. Mater., 191-194 (1992), Part A, pp.139-145

[5] A. Miyahara, J.B. Whitley, Proc. ICFRM-4 (Kyoto, Japan, 1989), J. Nucl. Mater., 179-181 (1991), Part A, pp.19-24

[6] P. Schiller, J. Nihoul, Proc. ICFRM-3 (Karlsruhe, FRG, 1987), J. Nucl. Mater., 155-157 (1988), Part A, pp.41-48

[7] R.F. Mattas, D.L. Smith, C.H. Wu, T. Kuroda, G. Shatalov, Proc. ICFRM-5 (Clearwater, FL, USA, 1991), J. Nucl. Mater., 191-194 (1992), Part A, pp.139-145

[8] E. Zolti, Proc. ICFRM-3 (Karlsruhe, FRG, 1987), J. Nucl. Mater., 155-157 (1988), Part A, pp. 386-391

[9] G. Federici, R. Matera, S. Chioccio, J. Dietz, G. Janeschitz, D. Driemeyer, J. Haines, M.S. Tillack, M. Ulrickson, Fus. Eng. Des. 28 (1995), pp. 34-43

[10] I. Smid, M. Akiba, M. Araki, S. Suzuki, K. Satoh, "Material and Design Considerations for the Carbon Armored ITER Divertor", JAERI Report, JAERI-M 93-149, Japan Atomic Energy Research Institute (1993)

[11] M. Araki, M. Akiba, M. Dairaku, K. Iida, H. Ise, M. Seki, S. Suzuki, K. Yokoyama, J. Nucl. Sci. Tech., 29 9 (1992), pp. 901-908

[12] S. Deschka, A. Cardella, J. Linke, M. Lochter, H. Nickel, J. Nucl. Mater., 203 (1993), pp. 67-72

[13] Y. Yoshino, H. Ohtsu, T. Shibata, J. Am. Ceram. Soc., 75 (12) (1992), pp. 3353-3357

[14] R. Kußmaul, "Einfluß unterschiedlicher Fügeflächengeometrien auf die Eigenspannungen und die Festigkeit von gelöteten Keramik-Metall-Verbunden", Dr. Ing. Thesis, Univ. Karlsruhe (1994)

[15] J. M. Mcnaney, R.M. Cannon, R.O. Ritchie, Int. J. Fracture 66 (1994), pp. 227-240

[16] M. D. Drory, M. D. Thouless, A.G. Evans, Acta Metall 36 (8) (1988), pp. 2019-2028

[17] J.D. Whitcomb, I.S. Raju, J.G. Goree, Comput. & Struc. 15 (1) (1982), pp. 23-37

[18] O. Iancu, "Berechnung von thermischen Eigenspannungsfeldern in Keramik/Metall-Verbunden", Dr.-Ing. Thesis, Univ. Karlsruhe (1989)

[19] M. L. Williams, Bull. Seismol. Soc. Am. 49 (2) (1959), pp. 199-204

[20] K. Mizuno, K. Miyazawa, T. Suga, J. Faculty of Eng., Univ. Tokyo (B), Vol. XXXIX, No. 4 (1988), pp. 401-412

[21] R. Viola, E.B. Deksnis, JET-P (94) 54, JET Joint Undertaking (1994)

[22] D.B. Bogy, Trans. ASME. J. Appl. Mech. 35 (1968), pp. 460-466

[23] S. Timoshenko, J. Opt. Soc. Am., 11 (1925), pp. 233-255

[24] J.P. Blancard, N.M. Ghoniem, Trans. ASME. J. Appl. Mech. 56 (1989), pp. 756-762

[25] D.B. Bogy, Trans. ASME. J. Appl. Mech. 35 (1968), pp. 460-466

[26] S.S. Wang, I. Choi, Trans. ASME. J. Appl. Mech. 49 (1982), pp. 541-560

[27] G.C. Sih, J.R. Rice, Trans. ASME. J. Appl. Mech. 31 (1964), pp. 477-482

[28] A.H. England, Trans. ASME. J. Appl. Mech. 32 (1965), pp. 400-402

[29] F. Erdogan, Trans. ASME. J. Appl. Mech. 32 (1965), pp. 403-410

[30] J.P. Blancard, N.M. Ghoniem, J. Nucl. Mater., 172 (1990), pp. 54-70

[31] A. Levy, J. Am. Ceram. Soc., 74 (9) (1991), pp. 2141-2147

[32] M. Araki, M. Akiba, M. Dairaku, K. Iida, H. Ise, M. Seki, S. Suzuki, K. Yokoyama, J. Nucl. Sci. Tech., **29** 9 (1992), pp. 901-908

[33] S. Deschka, A. Cardella, J. Linke, M. Lochter, H. Nickel, J. Nucl. Mater., 203 (1993), pp. 67-72

[34] Y. Yoshino, H. Ohtsu, T. Shibata, J. Am. Ceram. Soc., 75 (12) (1992), pp. 3353-3357

[35] T.V. Duggan, J. Byrne, "Fatigue as a Design Criterion", Mcmillan Press, London, 1977

[36] J.A. Bannantine, J.J. Comer, J.L. Handrock, "Fundamentals of Metal Fatigue Analysis", Prentice Hall, New Jersey, 1990

Chapter 2. Loading nature of the material interface in a joint component under fusion relevant thermal loads

1. Introduction

The simple beam theory can be used to calculate the stresses in the bulk of brazed joints [1-3]. The stress field based on the beam theory is uniaxial depending on the distance from the neutral axis of the strip.
In this model, it is assumed that the longitudinal length of the bonded strip is sufficiently larger than the thickness of each layer. Under this limitation, the solution is valid only for the region distant from the edge boundary according to the Saint Venant's principle.
Beam theory breaks down at distances less than the order of the beam thickness from the end where plane sections do not remain plane.

More rigorous analysis is required to describe the stress fields near the free surface edge [4]. The stress fields near the tip of interfacial cracks show a similar stress concentration as in the free edge region.
In general these stress fields consist of all three relevant stress components with substantial contributions, as opposed to the uniaxial stress field occuring in bulk region.
The stress fields near the free surface edge of the interface and near the interfacial crack tips have been investigated extensively. Several plane solutions were given from various analytical procedures [5-10].

In this chapter, the thermomechanical loading nature of a bond interface under a transient HHF pulse is quantitatively investigated in terms of the stress intensity factors.
For a perfect bond interface, bulk stresses and singular stress fields near the free surface are analyzed. A semi analytical procedure is employed to describe the stress singularity in terms of the stress intensity factor by the fracture mechanical analogy.
Stress singularities at the tip of the interfacial cracks are characterized quantitatively applying the crack flank displacement analysis. The evolution of the stress intensity factors and the strain energy release rates during a typical high heat flux load are determined. The difference in the thermal load characteristics between the edge crack and the center crack is discussed.
In addition, some experimental results of HHF cycling tests for a CFC/TZM brazed joint are presented.

2. Theoretical models

2.1. Bulk stress in a bond joint

Solution for the bulk thermal stresses in a perfectly bonded joint consisting of two layered strips was given by Timoshenko [3]. The model for this analysis is shown in Fig.2.1.

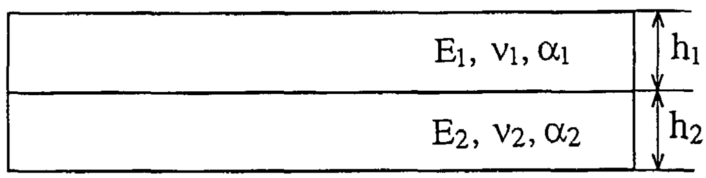

Fig. 2.1. Two dimensional joint model used for the Timoshenko's theory.

E_i is the Young´s modulus, ν_i is the Poisson´s ratio, h_i is the thickness of each strip and α_i is the thermal expansion coefficient. Subscript i denotes the material 1 and material 2.
The maximum stress occuring at the material interface is found to be

$$\sigma_{max} = \frac{1}{\rho}\left[\frac{2(E_1I_1 + E_2I_2)}{h_1(h_1 + h_2)} + \frac{1}{2}E_1h_1\right], \qquad (2.1)$$

where I_i is the moment of inertia of the individual layers and ρ is the radius of curvature of the strip. I_i is of the form

$$I_i = \frac{h_i^3}{12} \quad (i = 1, 2) \qquad (2.2)$$

and ρ is given by

$$\rho = \frac{(h_1 + h_2)\left[3(1+m)^2 + (1+mn)(m^2 + \frac{1}{mn})\right]}{6(\alpha_2 - \alpha_1)\Delta T(1+m)^2}, \qquad (2.3)$$

where ΔT is the temperature change and m, n are given by

$$m = \frac{h_1}{h_2}, \quad n = \frac{E_1}{E_2} \qquad (2.4)$$

As was mentioned in the introduction, the stress solution given in eq.(2.1) is uniaxial and there is no normal and shear stress components.
For a interfacial crack of a thermally stressed bond joint, the crack extension is driven by the combination of three modes of fracture. This mixed mode deformation of the crack tip is related to normal-, and shear components of the near tip stress fields. The axial stress component in the bulk region has therefore no direct correlation with the stress intensity factors required for the fracture mechanical consideration.
The bulk stress level is proportional to the misfit of the thermal expansion coefficients and the temperature change. It was shown by Timoshenko that the solution depends weakly on the mismatch of the elastic modulus.

The solution is valid only for elastic, isotropic materials subjected to uniform temperature change. Thus it cannot yield correct predictions for the thermal stress fields by the HHF load.

2.2. Stress state near free surface edge of interface

The beam theory breaks down at the edge of the bi-material interface due to the deformation of the traction free surfaces. A more rigorous analysis is needed to investigate the stress fields in this region.

For the special geometry shown in Fig.2.2, in which the free surface intersects the interface at right angles, the stress state near the free edge of the interface was formulated by Yang as [11]

$$\sigma_{ij}(r,\theta) = \frac{K}{(r/L)^{\omega}} f_{ij}(\theta) + \sigma_{ijo}(\theta), \tag{2.5}$$

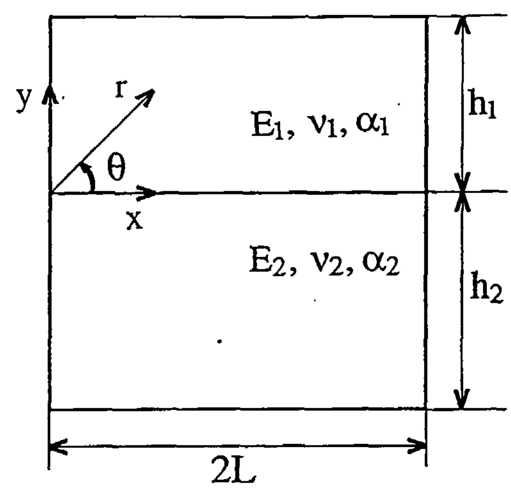

Fig. 2.2. Two dimensional joint model to analyze the stress singularity.

where r and θ are the polar coordinates and L is a characteristic dimension of the geometry. For a given wedge angles, the order of singularity ω and the angular functions $f_{ij}(\theta)$ are a function of the elastic constants E and ν.
The order of singularity ω is obtained by solving the following equation,

$$\lambda^2(\lambda^2-1)\alpha^2 + 2\lambda^2\left[\sin^2(\pi\lambda/2)-\lambda^2\right]\alpha\beta + \left[\sin^2(\pi\lambda/2)-\lambda^2\right]^2\beta^2 + \sin^2(\pi\lambda/2)\cos^2(\pi\lambda/2) = 0, \tag{2.6}$$

where

$$\lambda = 1 - \omega, \tag{2.7}$$

$$\alpha = \frac{m_2 - km_1}{m_2 + km_1},$$

$$\beta = \frac{(m_2 - 2) - k(m_1 - 2)}{m_2 + km_1}, \tag{2.8}$$

$$k = \frac{\mu_2}{\mu_1}, \tag{2.9 a}$$

$$m_i = 4(1 - \nu_i) \quad \text{(plane strain)} \tag{2.9 b}$$

The stress intensity factor K and the constant stress term $\sigma_{ijo}(\theta)$ depend on the loading conditions, the elastic constants E, ν and the thermal expansion coefficients. They are proportional to temperature difference ΔT.
ω, $f_{ij}(\theta)$ and $\sigma_{ijo}(\theta)$ can be calculated analytically whereas K is determined by means of numerical methods.
For a given material combination and a wedge geometry, the three analytic parameters ω, $f_{ij}(\theta)$ and $\sigma_{ijo}(\theta)$ are constant. Then the stress intensity factor K can be taken for a parameter which provides the failure criterion corresponding to specific thermal loading conditions.
From the multiple dependence of the stress components on ω, $\sigma_{ijo}(\theta)$, and K in eq.(2.5), it can be seen that the stress intensification near the singularity is affected by the loading conditions and the mismatch of the elastic constants as well as the misfit of the thermal expansion coefficient.
The solutions given in eq.(2.5) can be applied for the thermal stresses associated with non uniform temperature fields which is a general feature of the HHF load condition. Eq.(2.5) was deduced for elastic, isotropic materials.

2.3. Stress state near interfacial cracks

The linear elastic fracture mechanics predicts the presence of the stress singularity of the order of 0.5 + $i\varepsilon$ at the tip of an interfacial crack, where the coefficient of the imaginary part ε depends on the elastic constants [10].
As the brazed joint is residually stressed even in the absence of thermal loads, the singular stress intensification at the crack tip still exists.
The extension of the cracks in the bi-material interface is driven by the mixed mode fracture that gives rise to a complex dependence of the stress intensity factors on the elastic properties of the materials.
An analytic relation which relates crack flank displacements to the stress intensity factors was presented by Stern and Hong [12]. It was demonstrated by Smelser that this model can be used to calculate the complex stress intensity factors of the interfacial cracks by use of the crack flank displacement data that can be obtained by numerical analysis [13].
In Fig.2.3, the model used for this method is shown.

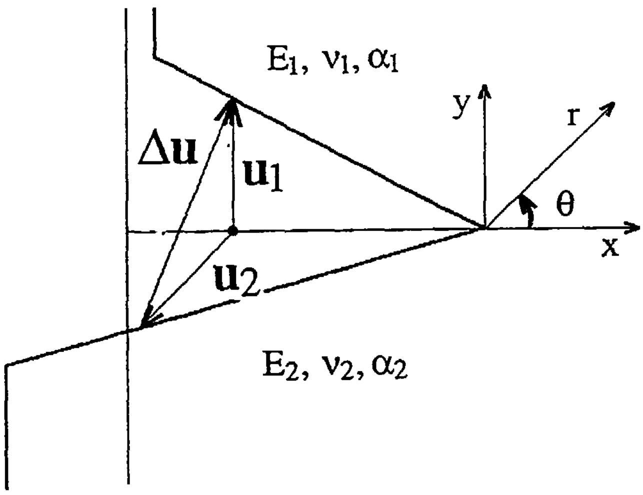

Fig. 2.3. Schematic representation of the interfacial crack displacement.

The complex stress intensity factor **K** for a elastic, isotropic material is defined as

$$\lim_{r\to 0} \sigma_\theta \big|_{\theta=0} = \lim_{x\to +0} (\sigma_{yy} - i\tau_{xy})\big|_{y=0} = \overline{\mathbf{K}}\, r^{\lambda-1}, \tag{2.10}$$

where $\overline{\mathbf{K}}$ is the complex conjugate of **K** which can be separated into two fracture mode components as

$$\mathbf{K} = K_I + i K_{II} = K_o e^{i\beta}. \tag{2.11}$$

The order of singularity λ is written as

$$\lambda = 0.5 + \mathbf{i}\varepsilon, \tag{2.12}$$

where

$$\varepsilon = \frac{1}{2\pi} \ln \frac{\mu_2 + \mu_1\kappa_2}{\mu_1 + \mu_2\kappa_1}, \tag{2.13 a}$$

$$\kappa_i = 3 - 4\nu_i \quad \text{(plane strain)}, \tag{2.13 b}$$

μ_i: shear modulus.

A complex crack opening displacement $\Delta\mathbf{u}$ is defined as

$$\Delta u = u_1|_{\theta=\pi} - u_2|_{\theta=-\pi} = |\Delta\mathbf{u}|\, e^{i\phi} \tag{2.14}$$

The magnitude of $\Delta\mathbf{u}$, $|\Delta\mathbf{u}|$ is written as

$$|\Delta\mathbf{u}| = \sqrt{|\Delta\mathbf{u}_x|^2 + |\Delta\mathbf{u}_y|^2}, \tag{2.15}$$

where $\Delta\mathbf{u}_x$ and $\Delta\mathbf{u}_y$ are the tangential and normal component of $\Delta\mathbf{u}$.
$\Delta\mathbf{u}$ is related to $\mathbf{K}$ as

$$\Delta\mathbf{u} = |\Delta\mathbf{u}|\, e^{i\phi} = \frac{\mu_2+\mu_1\kappa_2}{\mu_1\mu_2}\frac{\cosh \varepsilon\pi}{(1+\gamma)\lambda}\, \overline{\mathbf{K}}\, r^{\lambda} e^{-\frac{i\pi}{2}}, \tag{2.16}$$

where the bi-material constant γ is given by

$$\gamma = \frac{\mu_2+\mu_1\kappa_2}{\mu_1+\mu_2\kappa_1} \tag{2.17}$$

$|\Delta\mathbf{u}|$ can then be described in terms of K_o as

$$|\Delta\mathbf{u}| = \frac{(\mu_1+\mu_2\kappa_1)(\mu_2+\mu_1\kappa_2)}{\mu_1\mu_2(\mu_1+\mu_2+\mu_1\kappa_2+\mu_2\kappa_1)}\frac{\cosh \varepsilon\pi}{\lambda_o} K_o\sqrt{r}, \tag{2.18}$$

where

$$\lambda = \lambda_o\, e^{i\delta}, \tag{2.19}$$

$$\lambda_o = \sqrt{\frac{1}{4}+\varepsilon^2}, \tag{2.20 a}$$

$$\delta = \tan^{-1} 2\varepsilon. \tag{2.20 b}$$

From eq.(2.11), (2.16) and (2.20 b), the angle of the complex crack opening displacement ϕ is written as

$$\phi = \varepsilon \ln r - \beta - \delta - \frac{\pi}{2} \tag{2.21}$$

ϕ is calculated from the crack flank displacement data for a given radial position r_o by

$$\phi|_{r=r_o} = \tan^{-1}\left|\frac{\Delta\mathbf{u}_\theta}{\Delta\mathbf{u}_r}\right|_{r=r_o} \tag{2.22}$$

From eq.(2.21), (2.22), the angle of complex stress intensity factor β is given by

$$\beta = \varepsilon \ln r_o - \delta - \frac{\pi}{2} - \phi|_{r=r_o} \tag{2.23}$$

Using eq.(2.11) and (2.23), the mixed mode nature of the interfacial fracture can be analyzed by dividing the complex stress intensity factors into the components corresponding to each mode.
The stress intensity factor **K** in eq.(2.16) is also valid for the thermal loads which generate non uniform temperature fields as it is determined by the local displacement field around the crack faces.

2.4. J-integral for interfacial cracks

The energy release rate can be directly calculated from the numerically obtained field solutions.
For a linear elastic material, it can be shown by definition that the strain energy release rate G for each particular mode of fracture is identical with a path independent integral, termed J integral, which is defined as follows

$$J = \int_{\Gamma} \left(W\,dy - n_i \sigma_{ij} \frac{\partial u_j}{\partial x}\, ds \right), \qquad (2.24)$$

where Γ is an arbitrary contour (Fig.2.4) from the bottom crack surface around the tip to the top surface, n_i is the outward unit vector normal to Γ, W is the strain energy density, u_j are the displacements and ds is an infinitesimal element of contour arc length [14].

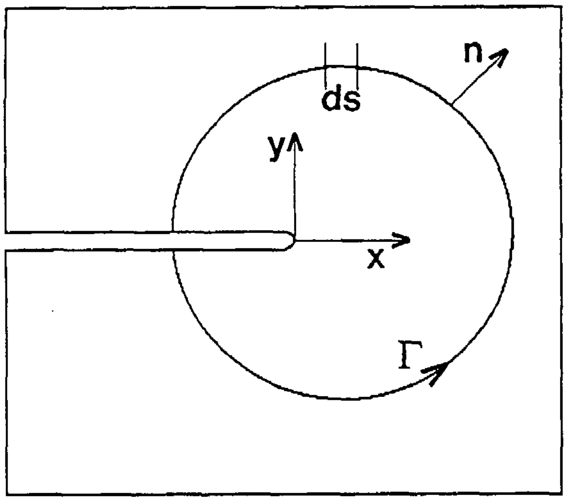

Fig. 2.4. Concept of the J-integral.

The standard J integral of fracture mechanics extends without a change to bi-materials provided the material under consideration is homogeneous at least in the x direction [15]. Thus eq.(2.24) can be applied to bonded systems when the material interface is straight and parallel to the crack faces.

The J-integral can be estimated from the finite element field solutions. By converting the line integral form into the domain integral expression, the J-integral representation becomes more compatible with the finite element formulation.
The validity of the domain integral method for calculating the energy release rate under thermo-mechanical loading was verified by Shih, et al. [16].
The domain integral expression for the J-integral in the absence of body force and crack face traction is

$$J = \int_A \left\{ \left[\sigma_{ij} \frac{\partial u_j}{\partial x} - W\delta_{xi} \right] \left(\frac{\partial q_x}{\partial x} + \frac{\partial q_x}{\partial y} \right) + \left[\alpha\sigma_{ii} \frac{\partial \Delta T}{\partial x} \right] q_x \right\} dA , \qquad (2.25)$$

where A is the area enclosed by Γ, C_O and the crack face contours C_+ and C_- (Fig.2.5). q_x is any smooth function in A with the value ranging from zero on the outer contour C_O to unity on the inner contour Γ.
As the eq.(2.24) requires no restriction on the material field and loading conditions, the numerical method according to eq.(2.25) provides the most wide generality in the fracture mechanical simulations.

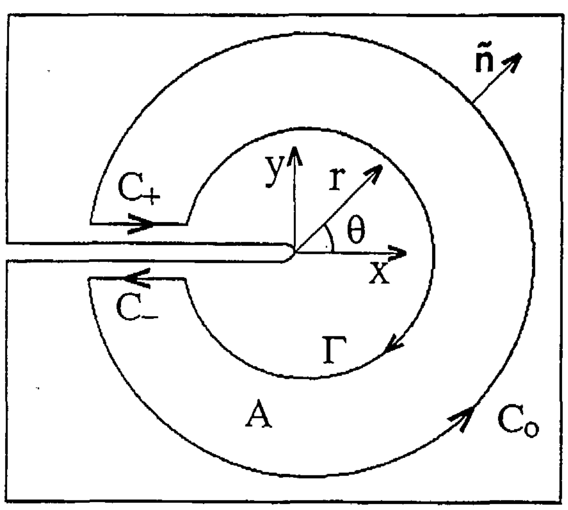

Fig. 2.5. Domain integral expression for the J-integral calculation.

According to the energy criterion, a crack in a brittle material under plane strain condition will advance when the J value of the crack for a given load exceeds its critical value, Jc which is the measure of the crack resistance of the material. The idea of the energy criterion can be applied to a bond interface.

2.5. Transient thermal conduction

To obtain the thermal stress-, and the deformation field solutions, the transient temperature fields generated by the HHF irradiation is determined applying the following theoretical model.
In the HHF simulation, radiation heat transfer is assumed to take place on the free boundaries except for the bottom face that is put to thermal isolation.

The governing equation for the transient heat conduction is

$$k_i \nabla^2 T = \rho_i C_i \frac{\partial T}{\partial t}, \qquad (2.26)$$

where k_i is the thermal conductivity, ρ_i is the density and C_i is the molar specific heat.

The initial condition is

$$T(x,y,0) = T_i = 20\ ^\circ C \qquad (2.27)$$

Considering the radiation heat transfer on the free surfaces, the boundary conditions are written as

$$k_1 \frac{\partial T(x,-h_1,t)}{\partial y} = 0, \qquad (2.28)$$

$$-k_2 \frac{\partial T(x,h_2,t)}{\partial y} = -\dot{q} + \varepsilon_2 \sigma (T^4 - T_a^4) \quad (0\ s. \le t \le 2\ s.), \qquad (2.29)$$

$$-k_2 \frac{\partial T(x,h_2,t)}{\partial y} = \varepsilon_2 \sigma (T^4 - T_a^4) \quad (2\ s. < t \le 6\ s.), \qquad (2.30)$$

where h_1 and h_2 is the thickness of the material 1 and 2 in Fig.2.2, $\dot{q}$ is the magnitude of input heat flux, ε is the emissivity of the materials, σ is the Stefan-Boltzmann constant and T_a is the ambient temperature, which is equal to the initial temperature T_i.
In addition,

i) for the edge crack

$$k_i \frac{\partial T(0,y,t)}{\partial x} = \varepsilon_i \sigma (T^4 - T_a^4), \qquad (2.31)$$

$$\frac{\partial T(L,y,t)}{\partial x} = 0 \qquad (2.32)$$

ii) for the center crack

$$-k_i \frac{\partial T(L,y,t)}{\partial x} = \varepsilon_i \sigma (T^4 - T_a^4), \tag{2.33}$$

$$\frac{\partial T(0,y,t)}{\partial x} = 0, \tag{2.34}$$

where eq (2.32) and (2.34) represent the symmetry condition for the model considered.

Assuming that no heat transfer occurs across the crack faces, interface conditions are given as

$$\frac{\partial T(x,0,t)}{\partial y} = 0 \quad (0<x<a), \tag{2.35}$$

$$T(x,0^+,t) = T(x,0^-,t) \quad (a<x<L), \tag{2.36}$$

$$k_2 \frac{\partial T(x,0^+,t)}{\partial y} = k_1 \frac{\partial T(x,0^-,t)}{\partial y} \quad (a<x<L), \tag{2.37}$$

where a is half of the crack length.

It is assumed that, the temperature distribution in the joint is maintained uniform during the brazing process, where the joint is bonded at 1070 °C and cooled down to 20 °C.
Thus the heat transfer problem does not need to be solved for the brazing simulation.

3. Computation

The thermo-elastic analyses were carried out by the finite element code ABAQUS assuming the generalized plane strain condition [17]. 8-noded isoparametric quadrilateral elements were used for the thermal and stress analyses. In addition, interface elements were employed for crack surfaces to keep them from overlapping. For J-integral estimation, 1/4 point crack tip elements were used in the near tip domain.
In Fig.2.6, the geometry of the two dimensional CFC/TZM joint model used for the analyses is shown. A 2D CFC material Sepcarb N112 and a Mo alloy TZM were used as the armor tile and the metallic substrate material, respectively. Due to the symmetry, only the left half part was considered. The problem size of the computation models is listed in table 2.1.
Some selected material properties of the CFC and TZM are listed in table 2.2. In numerical analysis, the temperature dependence of the material properties and material anisotropy were taken into account. On the contrary, all analytical parameters in section 2.1, 2.2 and 2.3 were calculated using constant material properties at room temperature. In addition, the anisotropic material properties were given in averaged values.
The simulation of the brazing process precedes the HHF step to generate the residual stresses on which the following thermal stresses are superposed.

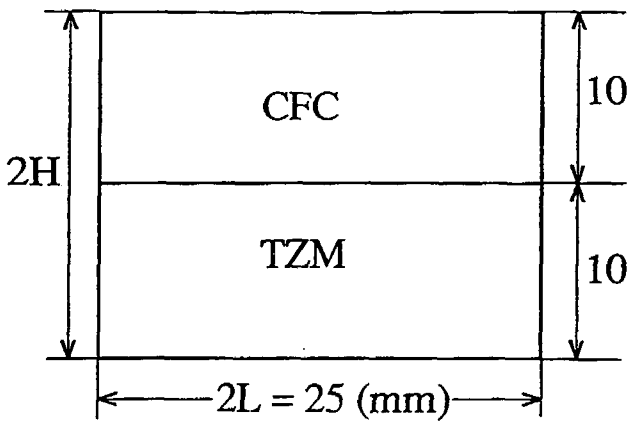

Fig. 2.6. Geometry of the CFC/TZM joint model used for the analysis.

Table 2.1
Problem size of the finite element analysis for each theoretical model

Models	Number of elements	Number of node points
Timoshenko (σ_{max})	900	2945
Yang (K)	1250	4054
Stern (K_0)	1250	4054
Rice (J)	1106	3770

Table 2.2
Selected material properties at RT. [18]

	2D CFC Sepcarb N112	TZM (Mo 0.5 Ti 0.1 Zr)
Elastic modulus (GPa)	28 (//) 24 ($\perp$)	300
Thermal expansion coefficient ($^{\circ}K^{-1}$)	1.5 (//) 2.7 ($\perp$)	5.3
Strength (tens./comp.) (MPa)	65/160 (//) 35/180 ($\perp$)	550 ($R_{p0,2}^{400^{\circ}C}$)/ 1150 (R_m)/
Thermal conductivity (W/m°K)	280 (//) 210 ($\perp$)	125

4. Experimentals

In the HHF simulation tests, the same material combination as in the theoretical analysis was used. A sample element is shown in Fig.2.7. Both the armor tile and the substrate have a common geometry of $25\times25\times10$ (mm^3).
Thermal cycling tests were conducted with ten cycles of HHF pulse. The HHF tests were carried out in a 60 kW electron beam teststand in Research Centre Jülich (KFA).
The tests were performed for two different temperature levels at the braze layer. The load parameters are listed in table 2.3.
To promote the heat removal during the HHF cycles, the specimens were mechanically clamped on a copper cooling plate.

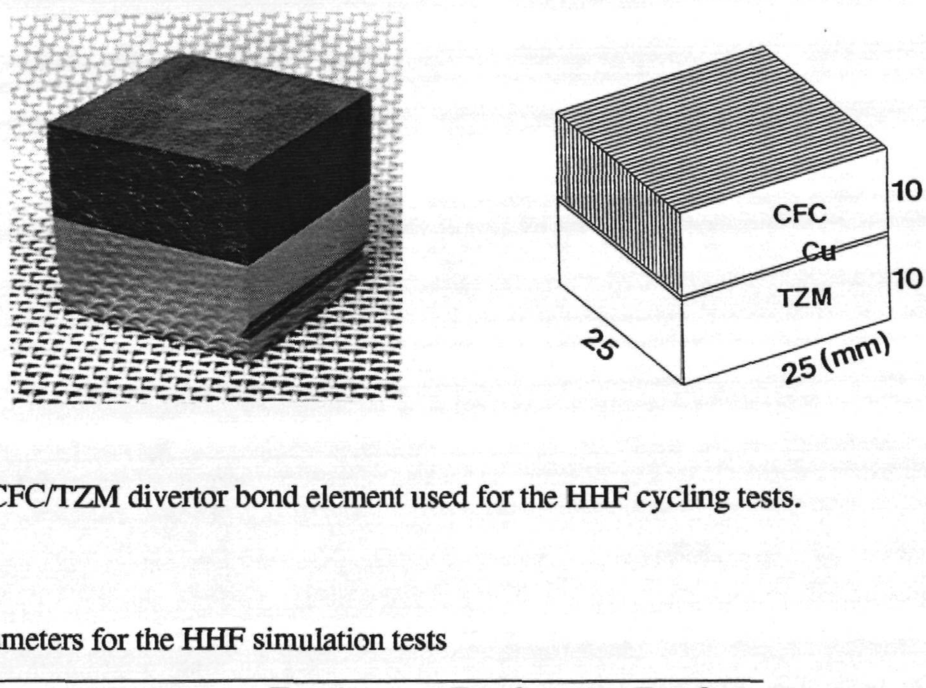

Fig. 2.7. CFC/TZM divertor bond element used for the HHF cycling tests.

Table 2.3
Load parameters for the HHF simulation tests

	Test 1	Test 2	Test 3
Net power density (MW/m^2)	14.5	14.5	14.5
Pulse duration in full power (s)	1.1	1.8	2.2
Maximum temperature of braze layer (°C)	600	790	899
Number of cycles	10	10	10

5. Results and Discussion

5.1. Thermal analysis

Fig.2.8 shows the reference thermal load history and the calculated temperature evolution which was applied for the numerical- and theoretical analyses.
It was assumed that a uniform surface heat flux of 20 MW/m^2 was deposited on the CFC tile surface with a pulse duration of 2 seconds. The bond joint was assumed to exist in a adiabatic state. This is a typical thermal loading condition in high heat flux simulations.

The joint was thermally equilibrated in 4 seconds after the load-off point. At the endpoint of the load pulse, a maximum temperature gradient has developed, where the surface temperature reached its maximum. The temperature at the bond interface has increased monotonically.

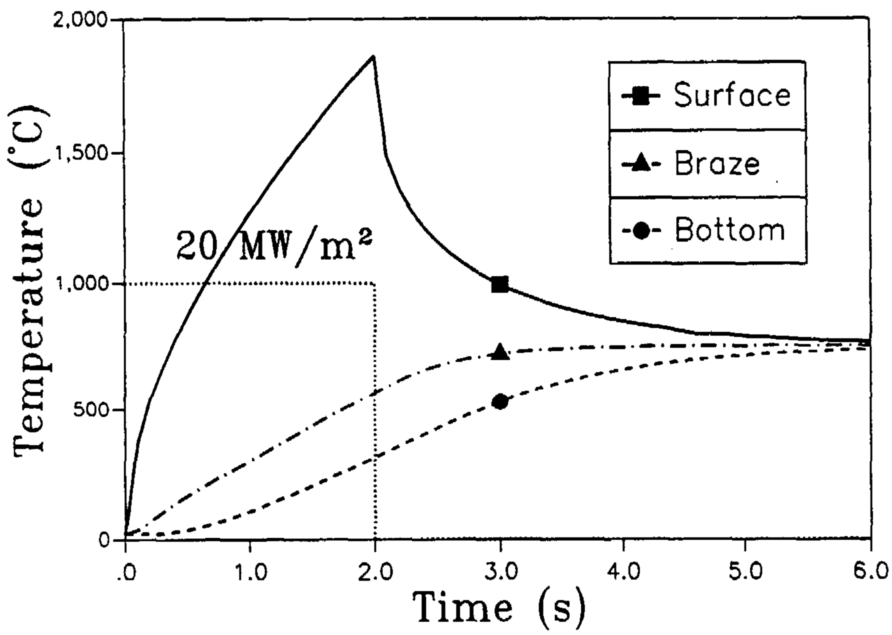

Fig. 2.8. Reference thermal load history and the corresponding temperature evolution applied for the numerical analysis.

5.2. Bulk stress analysis

The behavior of bulk stresses at the joint interface is shown in Fig.2.10. The finite element mesh used for the analysis is shown in Fig.2.9.
Two cases of thermal load conditions, that is, the HHF load and isothermal heating are considered. The axial component of the interfacial stress in center of the CFC side is given. Since it is the bond interface region where the misfit of CTE produces the maximum stress level, the interfacial temperature curve in Fig.2.8 was taken as the reference load history for the isothermal heating simulation.

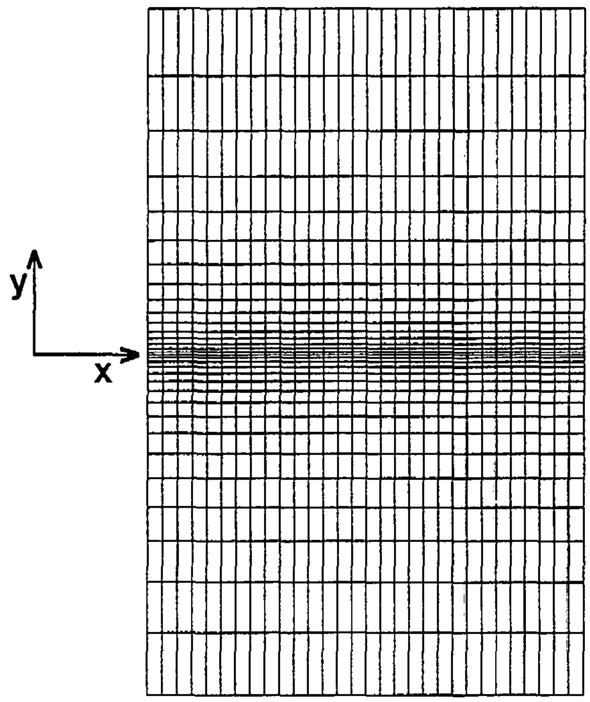

Fig. 2.9. Finite element mesh for the bulk stress calculation.

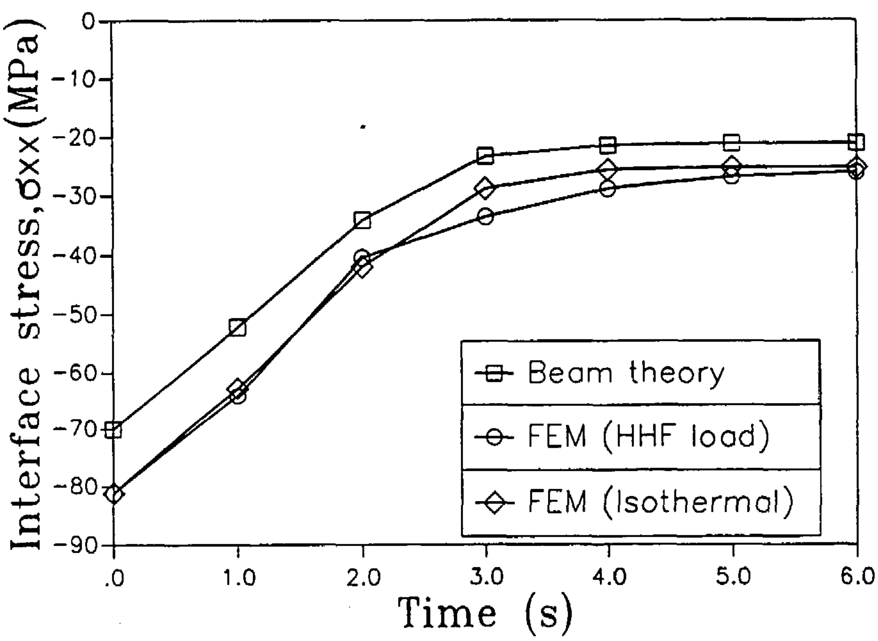

Fig. 2.10. Evolution of the bulk stress at the interface center.

The numerical result is compared to the maximum bulk stress value obtained from the Timoshenko's beam theory. In the beam theory approach, uniform temperature field was assumed, the time history of which was identical to that used for the isothermal heating simulation. There is some discrepancy between the numerical results and the values from the beam model ranging from 12.5 ~ 25 %. This difference is mainly due to the limitations assumed in the Timoshenko's model.
In residual stress state at room temperature, the joint exists in mostly stressed state. As the joint is heated during the thermal loading, the stress reduction takes place being coupled with the difference between the brazing-, and current temperature at interface. It can be seen from Fig.2.10 that the temperature gradient induced by the transient HHF load affects the bulk stress only slightly.

5.3. Stress distribution in the bond interface

Fig.2.12 shows the residual stress distribution in the bond interface of CFC side. X-axis means the normalized x coordinate along the interface with origin at its free surface edge. In Fig.2.11, the corresponding finite element mesh is shown. The mesh near the free surface edge of the interface was refined for the precise determination of the singular stress fields. Axial stress component σ_{xx} parallel to the bond interface (Fig.2.12 (a)) and normal stress component σ_{yy} vertical to the bond interface (Fig.2.12 (b)) are plotted.

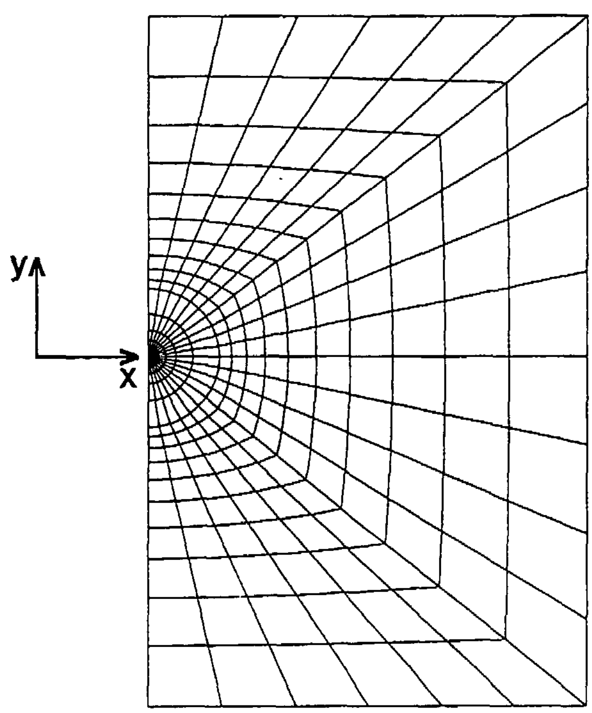

Fig. 2.11 (a)

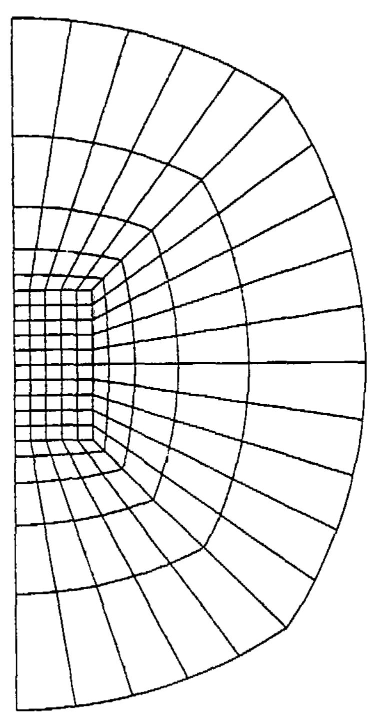

Fig. 2.11 (b)

Fig. 2.11. Finite element mesh to calculate the singular stress fields.
(a) Mesh for the whole geometry.
(b) Mesh for the singular region.

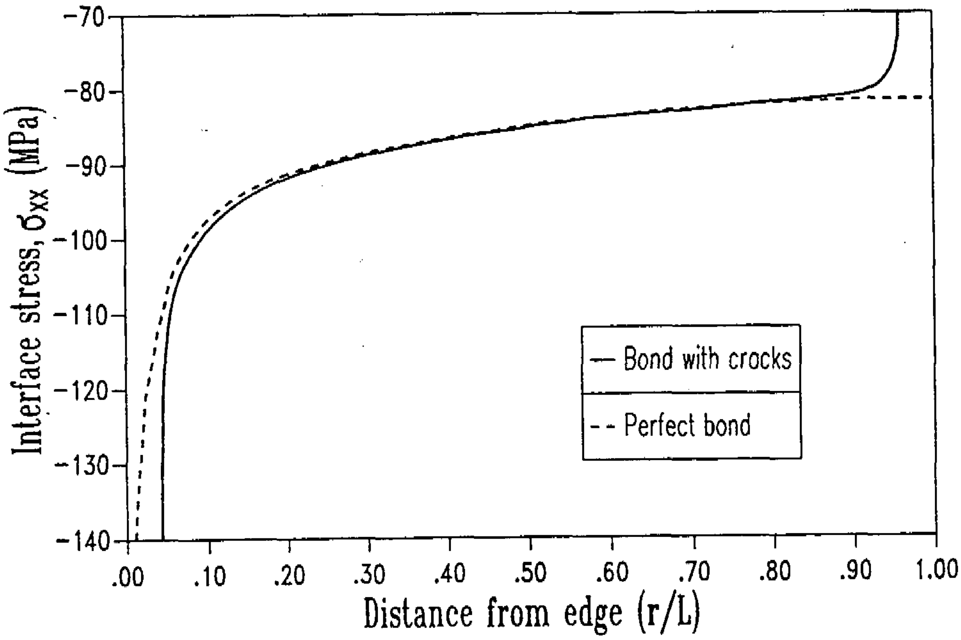

Fig. 2.12 (a)

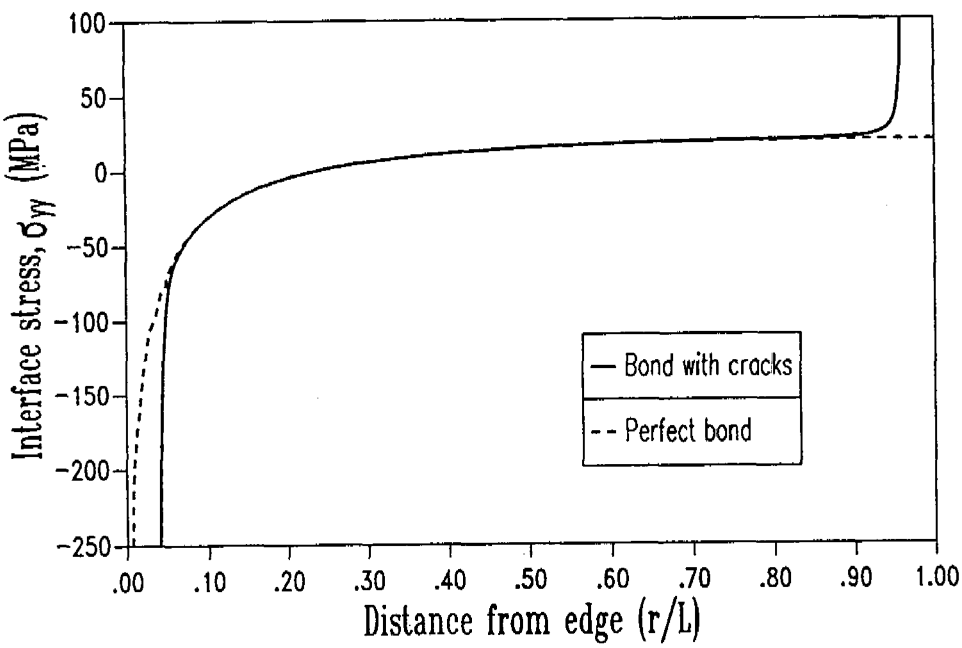

Fig. 2.12 (b)

Fig. 2.12. Distribution of the residual stress in the perfect-, and in the cracked bond interface.

(a) Axial stress component

(b) Normal stress component

A cracked interface as well as a perfect interface is considered. The former was assumed to have two cracks which locate at the free boundary and at the symmetry center. To calculate the stress field near the center crack, the symmetry axis boundary was combined with the refined mesh region. The length of the interfacial cracks was 0.5 mm, that amounts 4 % of the whole interface length.

In front of the crack tips and near the free surface edge, stress concentration is found in form of singularities as was predicted by the theoretical models.
Compared to the bulk stress level, the rate of stress intensification is very high. In bulk region distant from these singularities, the stress values for both interfaces coincide each other, that means that the interfacial cracks affect the stress fields just in the vicinity of the crack tips.
Since the numerical results for the singular stress fields are normally influenced by the degree of the mesh refinement, the convergence of the solutions was confirmed by optimizing the element size. The bulk stress values of the axial component near the center of the interface agree with the results in Fig.2.10.
In Fig.2.12 (b), it is shown that the normal component of the bulk stresses are negligible as was predicted in the beam theory. However, the normal component near the crack tips and near the free surface edge shows singular stress fields. Together with the shear stress component, it puts these regions into multiaxial stress state.
The behavior of the singular stress field near the free surface boundary and the interfacial cracks is analyzed in the following sections.

5.4. Analysis for the perfect interface

Applying the numerical stress solutions to eq.(2.5), the stress intensity factor K for the perfect interface in Fig.2.2 is obtained. The stress intensity factor K represents the complete singular stress field near the free surface edge of the interface. The calculated analytical parameters for the given joint system is as follows.

$\omega = 0.1805$
$\sigma_o = 148.1$ MPa
$f_{xx} = f_{rr}(0) = 0.2616$
$f_{yy} = f_{\theta\theta}(0) = 1$
$f_{xy} = f_{r\theta}(0) = 0.2083$

The variation of this stress intensity factor K under the HHF load in Fig.2.8 is shown in Fig.2.13. The results for the transient HHF loading is compared to that for the uniform heating case.

A discrepancy of the two curves is found in the vicinity of the load-off point (at the end of the HHF pulse) where the maximum temperature gradient develops in the joint. The maximum relative difference between the two load cases is about 6.9 %.
Under the HHF load, the thermal deformation near the stress singularity cause higher stressing than the isothermal deformation. This is due to the forced axial bending generated by the temperature gradient under HHF load. The unit of the stress intensity factor is same as that of stress because the coordinate in eq.(2.5) is normalized.

The tendency of the curve variations in Fig.2.13 is similar to that in Fig.2.10, which indicates that the behavior of the singular edge stress fields has similar qualitative pattern to the bulk stresses.

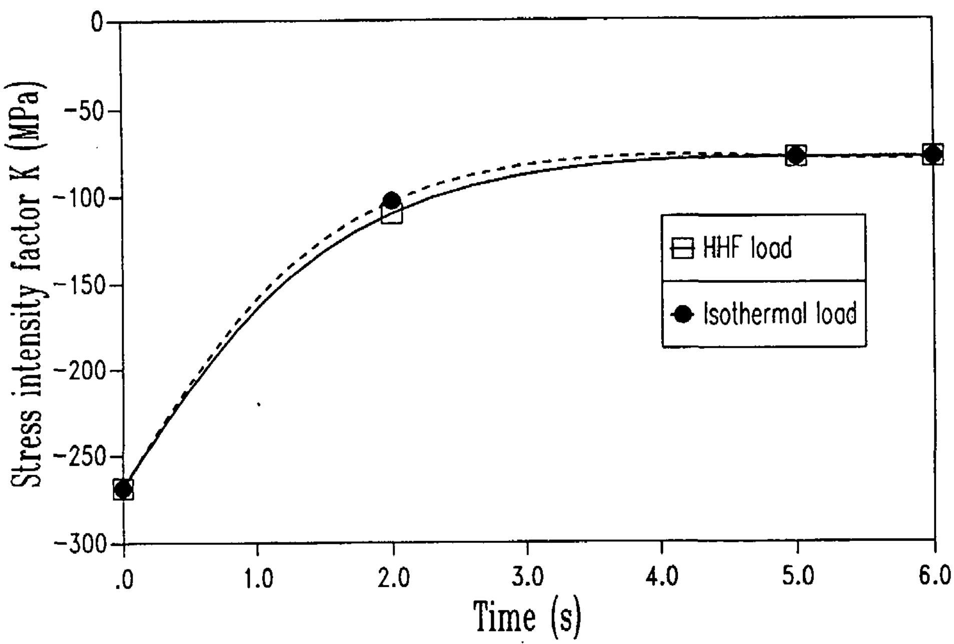

Fig. 2.13. Variation of the stress intensity factor K for the stress singularity at the interface edge.

5.5. Analysis for the cracked interface

The relative crack flank displacements defined in eq.(2.14) and (2.15) were calculated using the numerical displacement field data around the crack face. The change of the relative crack flank displacements under the HHF load given in Fig.8 is shown in Fig.2.14.
The in-plane (ΔUx)-, and the normal (ΔUy) components of the relative displacements are plotted for both edge crack and the center crack, respectively.

According to the numerical stress analysis in Fig.2.12, the normal stress component vertical to the interface is highly compressive in the edge crack region whereas it exerts a weak tensile traction on the center crack faces.
Thus, the normal component of the relative displacement for the edge crack should be zero to prevent the crack flank overlapping.
Due to the tensile traction on the center crack faces, crack opening is found in Fig.2.14.
Since the crack faces at the free surface edge undergoes unconstrained sliding, large in-plane displacement of edge crack was generated.
From the patterns of the curve variations in Fig.2.14, different deformation behaviors for both cracks can be suggested.

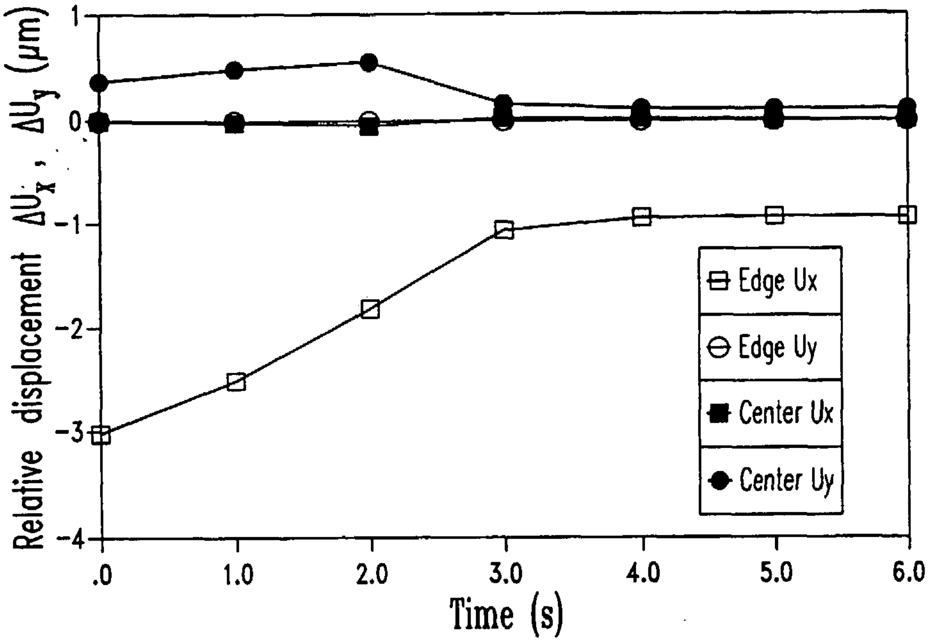

Fig. 2.14. Change of the relative crack flank displacement of the interfacial cracks.

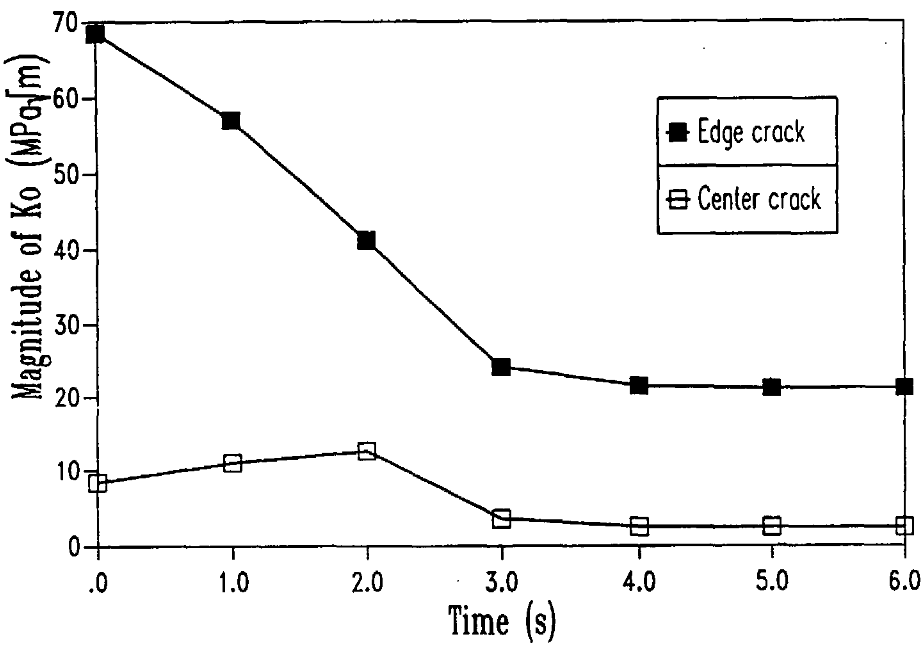

Fig. 2.15. Variation of the magnitude of the complex stress intensity factor K_o for the interfacial cracks.

The magnitude of the complex stress intensity factor, K_O was obtained by eq.(2.18) using the relative crack flank displacement data in Fig.2.14. The calculated analytical parameters for the stress singularity at the interfacial crack tips are as follows.

ε = -0.0878, λ_o = 0.5076, δ = -0.1738

In Fig.2.15, the time history of the K_O for the thermal load given in Fig.2.8 is shown. Since the K_O is a parameter representing the stress states and their intensifications, Fig.2.15 shows the characteristic loading nature of the interfacial cracks under HHF type thermal loads.

The edge crack experiences the maximum loading in the residual stress state at room temperature. When the additional thermal load is imposed on the joint, the degree of loading is reduced.
Such a behavior is not different from that of the bulk stress field or the singular stress field in the uncracked interface as was already seen in Fig.2.10 and 2.13.
On the other hand, the loading nature of the center crack seems to be unique. The loading on the center crack reaches its maximum at the end of the HHF pulse. After this point, K_O decreases and during the thermal equilibration phase, it becomes lower even than the value of the residual stress state. This indicates that the opening mode displacement of the center crack is related to the vertical temperature gradient in the joint.

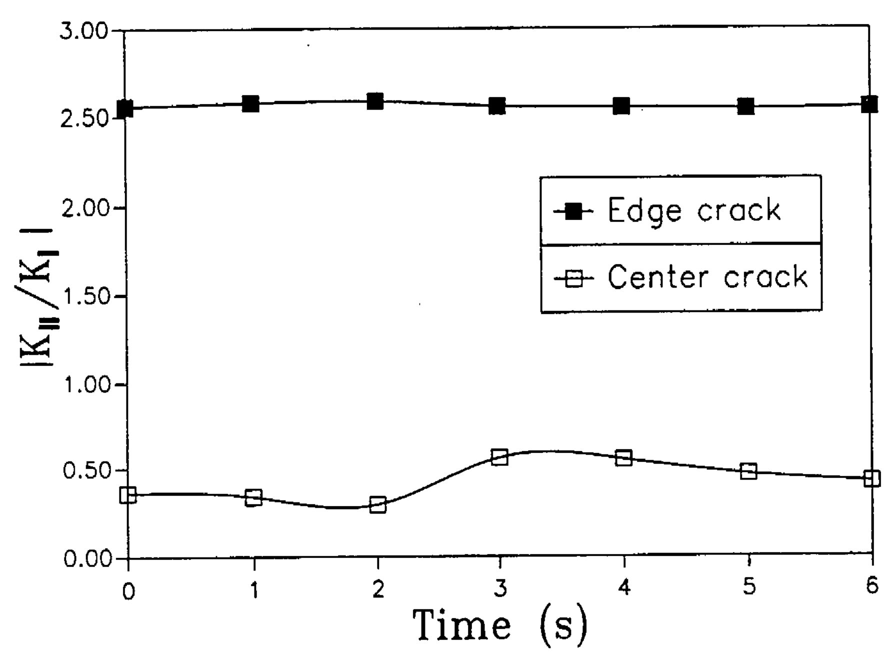

Fig. 2.16. Ratio of the fracture modes in the complex stress intensity factors (mode I to mode II component).

The K_O values for the edge crack are much higher than for the center crack. For example, the K_O for the center crack is only 12.2 % of the K_O for the edge crack in the residual stress state and 30.6 % at the load-off point.

In Fig.2.14, it can be seen from the relative amount of the displacement components that the deformation of the center crack is more related to opening mode whereas the edge crack deforms mostly by sliding mode.
This behavior can be quantified using eq.(2.11) and (2.22), by which the complex stress intensity factor can be divided into component of fracture mode I and II. The ratio of each component was determined to represent the relative contribution of each fracture mode to the mixed mode crack deformation under the given thermal load (Fig.2.16).

For the edge crack, the mode II component is 2.5 times more dominant than the mode I component. The ratio remains almost constant during the thermal load.
For the center crack, however, the mode I component prevails during the whole load history. There occurs a curve fluctuation after the load-off point. Having arrived at thermal equilibration, the value of the ratio recovered its initial value.

5.5. J-integral estimation for the interfacial cracks

The J-integrals for both cracks under the given HHF load were obtained by use of ABAQUS. The finite element mesh used for the J-integral evaluation is shown in Fig.2.17.

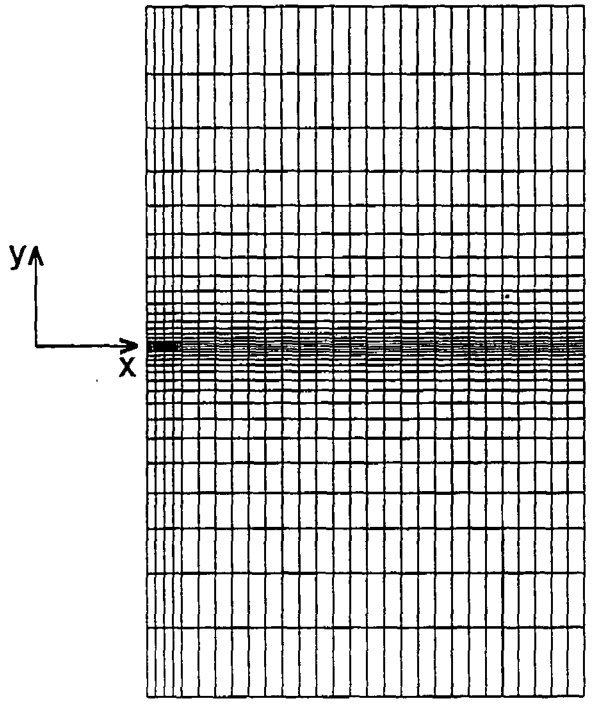

Fig. 2.17 (a)

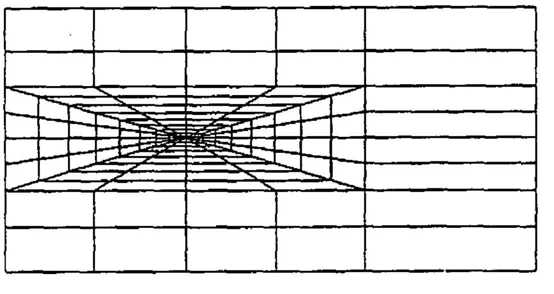

Fig. 2.17 (b)

Fig. 2.17. Finite element mesh for the J-integral evaluation.
(a) Mesh for the whole geometry
(b) Mesh near the crack tip

A fracture mechanical mesh was applied to the crack tip region. The elements surrounding the crack faces were so refined that the path independence of the J-integral was confirmed. Each concentric square track in Fig.2.17(b) represents the individual integration path. Except the first path around the crack tip, all the other paths showed excellent coincidence in J-integral values. In numerical estimation of J-integrals, the realistic material properties were used considering their temperature dependence and anisotropy.

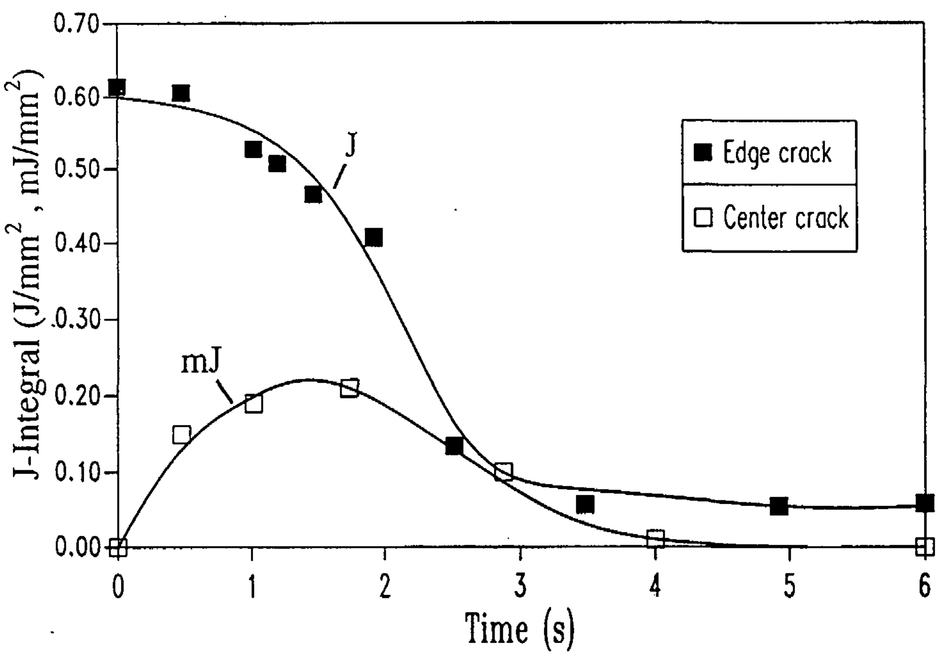

Fig. 2.18. Variation of the J-integral value for the interfacial cracks.

In Fig.2.18, the calculated J-integral values are plotted.
Under the given HHF load, the driving force of crack extension is much higher for the edge crack than for the center crack. Therefore, the most prefered location of crack initiation and propagation would be the free surface edge region of the interface.
The time history of J and K_0 for the reference HHF load case shows a similarity. The behavior of the J curves suggests that the edge crack will propagate during the cooling phase of the thermal cycling. If sufficient driving force of crack extension can be provided, the center crack would propagate during the heat pulse duration.

5.6. Microstructures of the damaged interface

The microstructures of the damaged interface after cyclic HHF loads are shown in Fig.2.19. Cracks propagate along the interface cutting through the fibers arrayed normal to the interface (Fig.2.19 (a)). The crack extension of this type is opening fracture mode where normal stress component plays a major role.

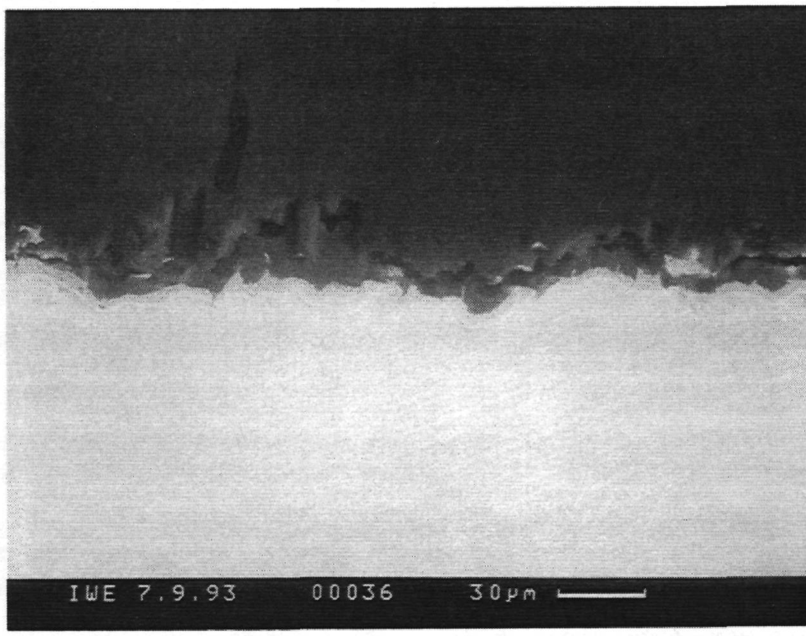

Fig. 2.19 (a) Test 1

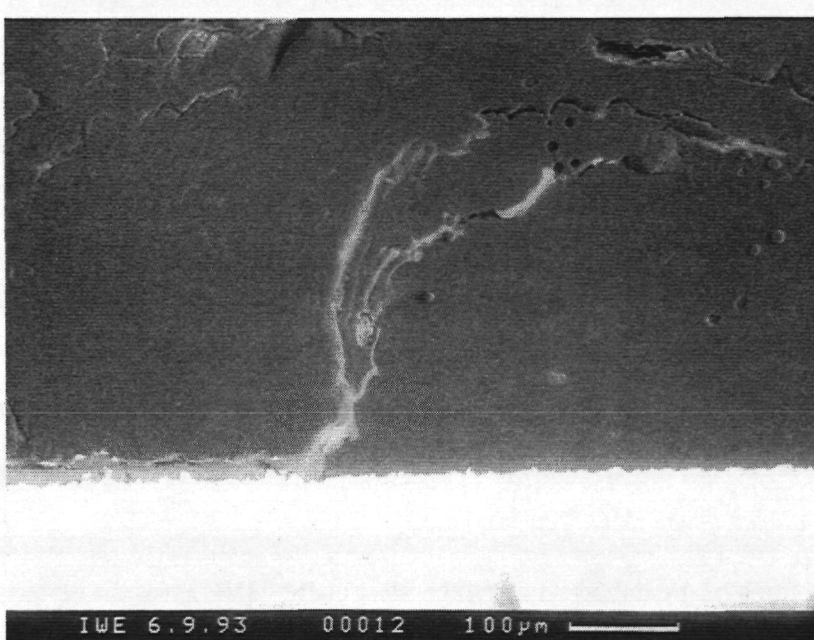

Fig. 2.19 (b) Test 2

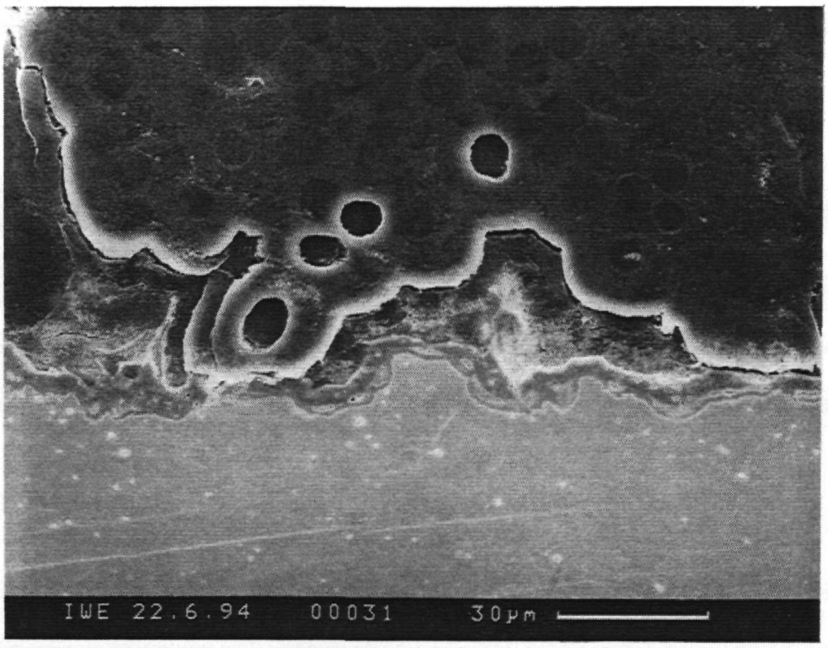

Fig. 2.19 (c) Test 2

Fig. 2.19. SEM micrographs for the damaged interface after the HHF cycling tests.
(a) Test 1, (b) Test 2, (c) Test 2

Cracks deviate sometimes from the initial path (Fig.2.19 (b)).
The shear stress induces a shearing mode fracture where fiber pulling out and shearing of the cracked planes are included (Fig.2.19 (c)). The cracks under shearing stress can extend by linking the crack segments lying on the fiber bundle boundary. The relative displacement between the subsided and upheaved regions is revealed by contrast in the micrograph.

6. Conclusions

One of the standard design concepts for divertor components in a fusion reactor is the bonded duplex structure.
The stress intensification near the free surface edge of the interface or near the interfacial crack tip is singular for certain material combinations and wedge angle geometries. The singular stress fields occuring in the material interface is significant to understand the loading nature of the bond interface in a joint system and may be critical for the structural integrity. To define and determine the interfacial loading, fracture mechanical approach can be applied together with the finite element calculations.
In this work, the interface of a bimaterial joint consisting of CFC/TZM system was investigated. High heat flux shock pulse was used as the thermal load which simulates the fusion operation condition.

Both perfect- and cracked interface were considered. Thermomechanical behavior was described in terms of the fracture mechanical parameters quantitatively.

The stress intensity factors of the singular stress fields both for the free surface edge of the interface and for the edge crack show a similar time variation. These are actually identical to that of bulk stress. They attain their maximum in the residual stress state and relieve monotonically coupled with the increase of the interface temperature. The center crack, however, has maximum stress intensity at the power-off point.
The magnitude of the stress intensity factor of the center crack amounts only to 12 - 31 % of that of the edge crack.
Tearing is a predominant fracture deformation mode for the edge crack whereas the center crack is related more to opening mode.

High heat flux cycling tests were conducted on the brazed CFC/TZM joint elements. The micrographs of the damaged interface reflect the mixed mode nature of the interfacial fracture.

7. Reference

[1] R. Kußmaul, "Einfluß unterschiedlicher Fügeflächengeometrien auf die Eigenspannungen und die Festigkeit von gelöteten Keramik-Metall-Verbunden", Dr. Ing. Thesis, Univ. Karlsruhe (1994)

[2] O. Iancu, "Berechnung von thermischen Eigenspannungsfeldern in Keramik/Metall-Verbunden", Dr.-Ing. Thesis, Univ. Karlsruhe (1989)

[3] S. Timoshenko, J. Opt. Soc. Am., 11 (1925), pp. 233-255

[4] J.P. Blancard, N.M. Ghoniem, J. Nucl. Mater., 172 (1990), pp. 54-70

[5] J.P. Blancard, N.M. Ghoniem, Trans. ASME. J. Appl. Mech. 56 (1989), pp. 756-762

[6] D.B. Bogy, Trans. ASME. J. Appl. Mech. 35 (1968), pp. 460-466

[7] S.S. Wang, I. Choi, Trans. ASME. J. Appl. Mech. 49 (1982), pp. 541-560

[8] G.C. Sih, J.R. Rice, Trans. ASME. J. Appl. Mech. 31 (1964), pp. 477-482

[9] A.H. England, Trans. ASME. J. Appl. Mech. 32 (1965), pp. 400-402

[10] F. Erdogan, Trans. ASME. J. Appl. Mech. 32 (1965), pp. 403-410

[11] D. Munz, Y.Y. Yang, Trans. ASME. J. Appl. Mech. 59 (1992), pp. 857-861

[12] M. Stern, C-C. Hong, "Advances in Engineering Science", Proc. 13th Annual Meeting, Soc. Eng. Sci. (Hampton, Virginia, 1976), NASA CP-2001, 2, pp. 699-710

[13] R.E. Smelser, Int. J. Fracture 15 (1979), pp. 135-143

[14] J.R. Rice, Trans. ASME. J. Appl. Mech. (1968), pp. 379-386

[15] J.R. Rice, "Mathematical Analysis in the Mechanics of Fracture", Fracture (Ed. H. Liebowitz) Vol. 2, S. 210, Academic Press, New York, 1968

[16] F.Z. Li, C.F. Shih, A. Needleman, Eng. Frac. Mech., 21 (2) (1985), pp. 405-421

[17] "ABAQUS User's Manual 5.4", Hibbit, Karlson and Sorenson Inc., Providence, RI, USA., 1994

[18] I. Smid, M. Akiba, M. Araki, S. Suzuki, K. Satoh, "Material and Design Considerations for the Carbon Armored ITER Divertor", JAERI Report, JAERI-M 93-149, Japan Atomic Energy Research Institute (1993)

Chapter 3. Behavior of stress singularities in a CFC / TZM bond interface under transient high heat flux loads

1. Introduction

The asymptotic stress states near the singular point can be effectively represented by the fracture mechanical approach which is based on the stress intensity factors and the order of the singularity [1,2]. For a given material combination, the order of singularity remains fixed and the stress intensity factors are the varing parameters corresponding to specific boundary conditions.

Extensive investigations have been performed to solve the bonded systems. Most of them has been analyzed for uniform temperature change or steady state heat conduction [1-5].
In case of off-normal operations like as plasma disruption or sudden loss of cooling, transient thermal flow will occur, which produces non-linear temperature profile in the direction normal to the material interface [6]. The non linear distribution of bulk temperature can also appear in a passively cooled bond joint under high heat flux irradiation.
Sweeping the X-point of separatrix may be necessary to reduce the peak temperature of the divertor plate surface. If the frequency of the sweeping is not high enough, the heat flow in the divertor component cannot reach a steady state [6-8]. Thus even under normal operations, the divertor would undergo the stress induced by the transient thermal flows.

In this work, the behavior of the singular stress fields in bonded interface is analyzed considering the transient thermal loads relevant to fusion conditions. Using the finite element method, electron beam irradiation with various heat fluxes is simulated for a passively cooled divertor bond element. The effect of the transient temperature gradient on the stress singularity and the interfacial stress is investigated quantitatively.

2. Theory

The problems of plane elasticity are solved by way of the Airy stress function Φ [9]. In the absence of body forces, the equations of static equilibrium are

$$\frac{\partial \sigma_{rr}}{\partial r} + \frac{1}{r}\frac{\partial \tau_{r\theta}}{\partial \theta} + \frac{\sigma_{rr} - \sigma_{\theta\theta}}{r} = 0, \qquad (3.1\text{-a})$$

$$\frac{1}{r}\frac{\partial \sigma_{\theta\theta}}{\partial \theta} + \frac{\partial \tau_{r\theta}}{\partial r} + \frac{2\tau_{r\theta}}{r} = 0, \qquad (3.1\text{-b})$$

where r, θ represent the radial and the azimuthal component in polar coordinate, respectively.

The compatibility equation for plane strain is

$$\nabla^2(\sigma_{rr}+\sigma_{\theta\theta})+\frac{E\alpha}{1-\nu}\nabla^2 T(r,\theta)=0, \qquad (3.2)$$

where E, ν, α are the Young´s modulus, poisson´s ratio and coefficient of thermal expansion, respectively.

The constitutive relations for plane strain are given by

$$\varepsilon_{rr}=\frac{1-\nu^2}{E}(\sigma_{rr}-\frac{\nu}{1-\nu}\sigma_{\theta\theta})+\alpha(1+\nu)\Delta T, \qquad (3.3\text{-a})$$

$$\varepsilon_{\theta\theta}=\frac{1-\nu^2}{E}(\sigma_{\theta\theta}-\frac{\nu}{1-\nu}\sigma_{rr})+\alpha(1+\nu)\Delta T, \qquad (3.3\text{-b})$$

$$\varepsilon_{r\theta}=\frac{1}{2\mu}\tau_{r\theta}, \qquad (3.3\text{-c})$$

where μ is the shear modulus and ΔT is temperature change.

The kinematic conditions are written as

$$\varepsilon_{rr}=\frac{\partial u_r}{\partial r}, \qquad (3.4\text{-a})$$

$$\varepsilon_{\theta\theta}=\frac{u_r}{r}+\frac{1}{r}\frac{\partial u_\theta}{\partial\theta}, \qquad (3.4\text{-b})$$

$$\varepsilon_{r\theta}=\frac{1}{2}(\frac{1}{r}\frac{\partial u_r}{\partial\theta}+\frac{\partial u_\theta}{\partial r}-\frac{u_\theta}{r}) \qquad (3.4\text{-c})$$

There exists a function Φ such that

$$\sigma_{rr}=\frac{1}{r}\frac{\partial\Phi}{\partial r}+\frac{1}{r^2}\frac{\partial^2\Phi}{\partial\theta^2}, \qquad (3.5\text{-a})$$

$$\sigma_{\theta\theta}=\frac{\partial^2\Phi}{\partial r^2}, \qquad (3.5\text{-b})$$

$$\tau_{r\theta}=\frac{1}{r^2}\frac{\partial\Phi}{\partial\theta}-\frac{1}{r}\frac{\partial^2\Phi}{\partial r\partial\theta} \qquad (3.5\text{-c})$$

so that the equations of equilibrium are satisfied automatically.

Substituting eq.(3.5) into eq.(3.2), the biharmonic equation of the Airy stress function Φ is derived.

$$\nabla^4\Phi(r,\theta)+\frac{E\alpha}{1-\nu}\nabla^2 T(r,\theta)=0 \qquad (3.6)$$

When the temperature field is harmonic,

$$\nabla^4\Phi(r,\theta)=0 \tag{3.7}$$

Inserting eq.(3.4) and eq.(3.5) into eq.(3.3) yields the displacement in terms of the Φ.

$$\frac{\partial u_r}{\partial r}=\frac{1}{2\mu}\left[\frac{1}{r}\frac{\partial\Phi}{\partial r}+\frac{1}{r^2}\frac{\partial^2\Phi}{\partial\theta^2}-\nu\nabla^2\Phi\right]+(1+\nu)\alpha\Delta T, \tag{3.8-a}$$

$$\frac{\partial u_\theta}{\partial r}-\frac{u_\theta}{r}+\frac{1}{r}\frac{\partial u_r}{\partial\theta}=\frac{1}{\mu}\left[\frac{1}{r^2}\frac{\partial\Phi}{\partial\theta}-\frac{1}{r}\frac{\partial^2\Phi}{\partial r\partial\theta}\right] \tag{3.8-b}$$

The stress solutions in eq.(3.5) can then be found by solving the fourth order partial differential equation for Φ with the boundary and interface conditions concerning the continuity of displacements and the balance of forces on the bond line and traction free surfaces.

The model for the analysis of singular stress fields is shown in Fig.3.1.
In this paper, a special geometry of $\theta_1=-\theta_2=\frac{\pi}{2}$ will be considered assuming the crack free, perfect bond interface.

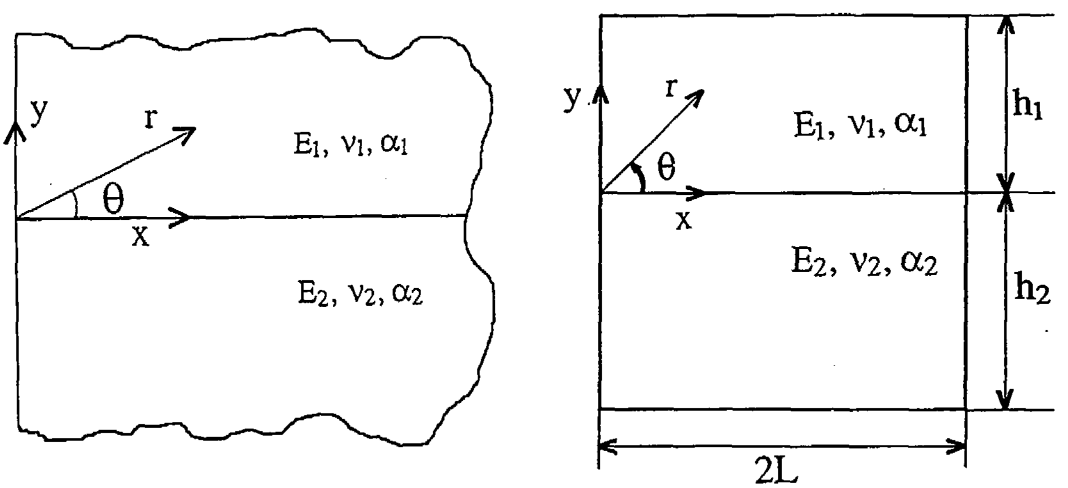

Fig. 3.1 (a) Fig. 3.1 (b)

Fig. 3.1
(a). Two dimensional, semi-infinite quarter plane model to analyze the stress singularity.
(b). A special case of the two dimensional joint model with a right angle wedge geometry.

To determine the stress states near the free surface edge of the interface, following boundary and interface conditions are deduced for the model in Fig.3.1 (a).

i) At the traction free boundary

$$\sigma_{1\theta\theta}(r,\frac{\pi}{2}) = \sigma_{2\theta\theta}(r,-\frac{\pi}{2}) = 0, \qquad (3.9\text{-a})$$

$$\tau_{1r\theta}(r,\frac{\pi}{2}) = \tau_{2r\theta}(r,-\frac{\pi}{2}) = 0 \qquad (3.9\text{-b})$$

ii) At the bond interface

$$\sigma_{1\theta\theta}(r,0) = \sigma_{2\theta\theta}(r,0), \quad \tau_{1r\theta}(r,0) = \tau_{2r\theta}(r,0), \qquad (3.10\text{-a,b})$$

$$u_{1r}(r,0) = u_{2r}(r,0), \quad u_{1\theta}(r,0) = u_{2\theta}(r,0), \qquad (3.10\text{-c,d})$$

where the subscript 1 and 2 represent the material 1 and 2 in Fig.3.2 (a), respectively.

The problem can be solved by direct application of a solution form given in eq.(3.11) for the stress function in eq.(3.7) [10]

$$\Phi_j(r,\theta) = \sum_{k=1}^{N} r^{(2-\omega_k)} \left\{ A_{jn}\sin(\omega_k\theta) + B_{jn}\cos(\omega_k\theta) + C_{jn}\sin[(2-\omega_k)\theta] + D_{jn}\cos[(2-\omega_k)\theta] \right\} \qquad (3.11)$$

where the subscript j means each material [j=1,2].

Eq.(3.11) is then substituted into eq.(3.5) and (3.8). By imposing the boundary and interface conditions, a system of eight linear homogeneous equations is produced for $\omega_k \neq 0$.

$$[A_k]\{X_k\} = \{0\}, \qquad (3.12)$$

where $[A_k]$ is an 8×8 coefficient matrix associated with $A_{jk}, B_{jk}, C_{jk}, D_{jk}$ in the homogeneous equations system, and $\{X_k\} = \{A_{1k}, B_{1k}, C_{1k}, D_{1k}, A_{2k}, B_{2k}, C_{2k}, D_{2k}\}^T$.
For the condition that the equation system has a non-trivial solution, the determinant of the matrix should be zero

$$|A_k| = 0. \qquad (3.13)$$

The roots of this transcendental characteristic equation are the parameters ω_k which are the order of the singularity. For a special geometry with wedge angles of $\theta_1 = -\theta_2 = \frac{\pi}{2}$ (Fig.3.1 (b)), there exists only one ω_k, that is $\omega_k = \omega$.
The stress terms corresponding to $\omega_o = 0$ can also be calculated for this geometry. Knowing the parameter ω, the vector of the unknown constants $\{X_k\}$ is determined by solving the equations system.

The stress field near the free surface edge of the interface in Fig.3.1 (b) will be of the form

$$\sigma_{ij} \propto r^{-\omega}, \tag{3.14}$$

where ω is real ranging from zero to 0.41.

The asymptotic form of eq.(3.14) suggests that the singular stress fields in the free edge domain of the bond interface can be expressed with parameters analogous to those for the crack tip stress fields in linear elastic fracture mechanics (LEFM).
In LEFM, the stress field near a crack tip is given by

$$\sigma_{ij}(r,\theta) = \frac{K}{(2\pi r)^{0.5}} f_{ij}(\theta) + \sigma_r, \tag{3.15}$$

where r, θ are polar coordinates having origin at the tip of the crack, $f_{ij}(\theta)$ is a function of angle depending on the particular fracture mode and σ_r is the remainder of higher order terms.

The stress intensity factor K is considered to be a measure of the stress intensification near the singularity and has been taken for a useful criteron to predict crack extension. According to the fracture mechanical analogy suggested by Yang [10,11], the stress state near the singularity in Fig.3.1 (b) can be described by

$$\sigma_{ij}(r,\theta) = \frac{K}{(r/L)^{\omega}} f_{ij}(\theta) + \sigma_{ijo}(\theta), \tag{3.16}$$

where the radial component of polar coordinates is normalized by the characteristic dimension of the joint geometry.

Given a wedge angle geometry, $\omega, f_{ij}(\theta)$, K and $\sigma_{ijo}(\theta)$ are dependent on the elastic constants E and ν. In addition, the stress intensity factor K and the non singular term σ_{ijo} are dependent on the thermal expansion coefficient α and proportional to the temperature difference ΔT. The order of singularity ω, the angular function f_{ij} and the stress term σ_{ijo} can be determined analytically.

The order of singularity ω is obtained by solving the eq.(3.13) in which the determinant is given by

$$|A| = \lambda^2(\lambda^2-1)\alpha^2 + 2\lambda^2\left[\sin^2(\pi\lambda/2)-\lambda^2\right]\alpha\beta + \left[\sin^2(\pi\lambda/2)-\lambda^2\right]^2\beta^2 + \sin^2(\pi\lambda/2)\cos^2(\pi\lambda/2), \tag{3.17}$$

where

$$\lambda = 1-\omega, \tag{3.18}$$

$$\alpha = \frac{m_2 - km_1}{m_2 + km_1}, \tag{3.19-a}$$

$$\beta = \frac{(m_2-2)-k(m_1-2)}{m_2+km_1}, \tag{3.19-b}$$

with

$$k = \frac{\mu_2}{\mu_1}, \tag{3.20-a}$$

$$m_i = 4(1-\nu_i) \quad \text{(plane strain)} \tag{3.20-b}$$

From eq.(3.13) and (3.17), it is seen that the roots of the equation depend only on the Dundurs parameters α and β. Eq.(3.17) can also be derived by applying the Mellin transformation to eq.(3.5) and (3.7) [2].

The components of the non singular term σ_{ijo} are

$$\sigma_{rro} = \frac{\sigma_o}{2}(1-\cos 2\theta) \tag{3.21-a}$$

$$\sigma_{\theta\theta o} = \frac{\sigma_o}{2}(1+\cos 2\theta) \tag{3.21-b}$$

$$\tau_{r\theta o} = \frac{\sigma_o}{2}\sin 2\theta, \tag{3.21-c}$$

where

$$\sigma_o = \Delta\alpha \cdot \Delta E \cdot \Delta T \tag{3.22-a}$$

$$\Delta\alpha = \alpha_1(1+\nu_1) - \alpha_2(1+\nu_2) \tag{3.22-b}$$

$$\Delta E = \left[\frac{1}{E_1^*} - \frac{1}{E_2^*}\right]^{-1} \tag{3.22-c}$$

$$E_i^* = \frac{E_i}{\nu_i(1+\nu_i)} \quad \text{(plane strain)} \tag{3.22-d}$$

The stress intensity factor K can be determined using the stress field solution σ_{ij}^{FEM} obtained from the finite element method. Eq.(3.23) shows a double logarithmic expression of eq.(3.16), where the stress term σ_{ij} is replaced by σ_{ij}^{FEM}.

$$\log_{10}\left[\frac{\sigma_{ij}^{FEM}(r,\theta) - \sigma_{ijo}(\theta)}{f_{ij}(\theta)}\right] = -\omega \log_{10}\left(r/L\right) + \log_{10}(K) \tag{3.23}$$

Plotting the eq.(3.23) gives rise to a straight line in the range near the singularity. The intercept of the straight line on the ordinate corresponds to $\log_{10}(K)$ whereas the slope of the line yields ω.
Since σ_{ij}^{FEM} is obtained for a finite body under specific thermal load, the effects of finite dimension and inhomogeneity of the temperature field are included in the procedure to determine the stress intensity factor K.

In contrast to this, ω and f_{ij} are independent on the thermal gradient because these parameters are determined only for the local domain near the singularity. It was shown numerically that σ_{ijo} is hardly affected by the thermal gradient [12].
Therefore using eq.(3.23), the stress intensity factor K can be found even for transient thermal load condition which causes a non-harmonic temperture field. With ω, $f_{ij}(\theta)$, K and $\sigma_{ijo}(\theta)$, the stress components near the free surface edge of the interface are reproduced from eq.(3.16).

3. Computation

The thermo-elastic analyses were carried out by the finite element code ABAQUS assuming generalized plane strain conditions [13]. 8-node isoparametric quadrilateral elements were used for the thermal and stress analyses.

In Fig.3.2, the geometry of the two dimensional CFC/TZM joint model used for the analyses is shown.

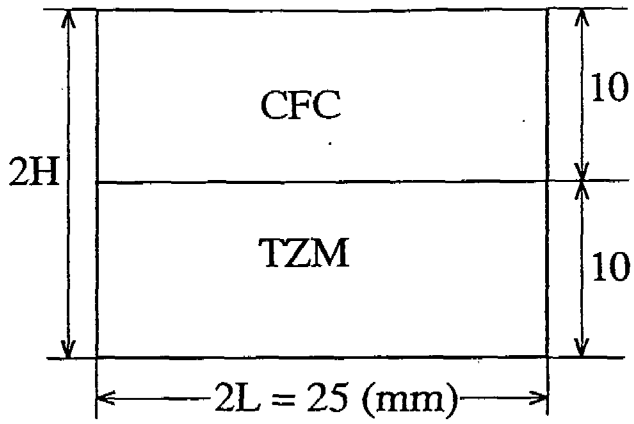

Fig. 3.2. CFC/TZM joint model used for the analysis.

A 2D CFC material Sepcarb N112 and a Mo alloy TZM were selected as the armor tile and the metallic substrate material, respectively. Due to the symmetry, only the left half part was considered. 1250 elements and 4054 node points were generated.
In numerical analysis, temperature dependence of the material properties was taken into account. On the contrary, all analytical parameters in section 2 were calculated using constant material properties for room temperature.
The simulation of the brazing process was carried out prior to the HHF step to generate the residual stresses on which the following thermal stresses are superposed.

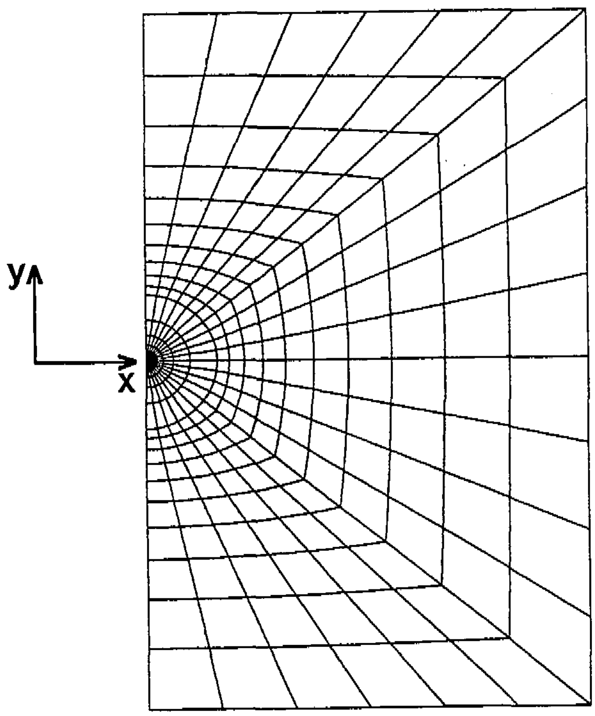

Fig. 3.3 (a)

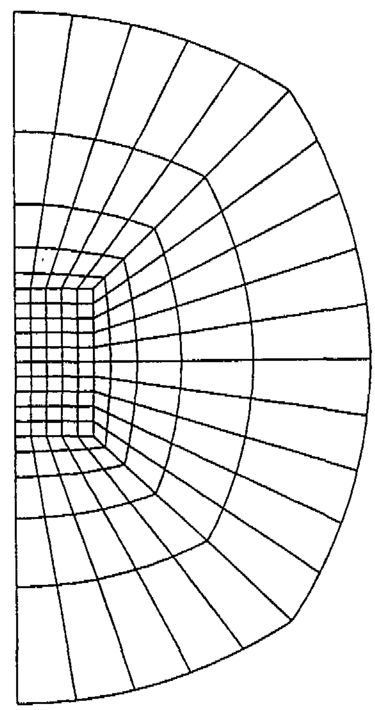

Fig. 3.3 (b)

Fig. 3.3. Finite element mesh to calculate the singular stress fields near the free surface edge of the bond interface.
(a) Mesh for the whole geometry.
(b) Mesh for the singular region.

4. Results and discussion

The singular thermal stress field near the free surface edge of the bond interface in Fig.3.2 was analyzed. To determine the stress intensity factor for the stress singularity using eq.(3.23), finite element mesh shown in Fig.3.3 was used. The elements near the singular point were refined confirming the solution convergence. Perfect bonding of the interface was assumed.
To simulate a fusion loading condition which produces non harmonic temperature fields, a transient shock load of a heat flux pulse was assumed.

Fig.3.4 shows the reference thermal load history and the calculated temperature evolution that was applied for the numerical-, and theoretical analyses. It was assumed that a uniform surface heat flux of 20 MW/m^2 was deposited on the CFC surface with a pulse duration of 2 seconds. After the load pulse, the bonded joint was assumed to exist in a adiabatic state.
The joint was thermally equilibrated in 4 seconds after the load-off point. At the endpoint of the load pulse, a maximum temperature gradient has developed, where the surface temperature has reached its maximum. The temperature at the bond interface has increased

monotonically. This is a characteristic feature of thermal loads being found in HHF operations. The stress fields were calculated for the load-off point.

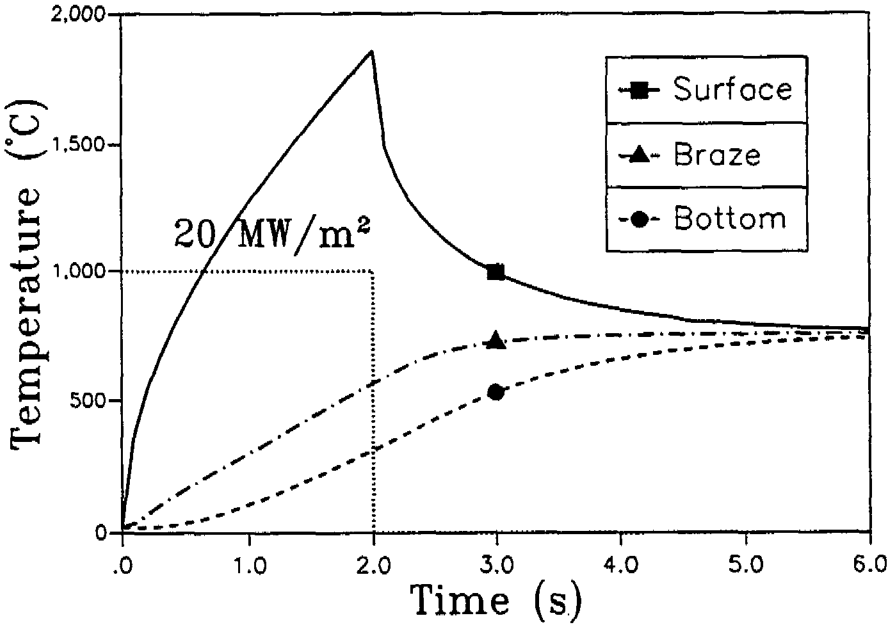

Fig. 3.4. Reference thermal load history and the corresponding temperature evolution applied for the numerical analysis.

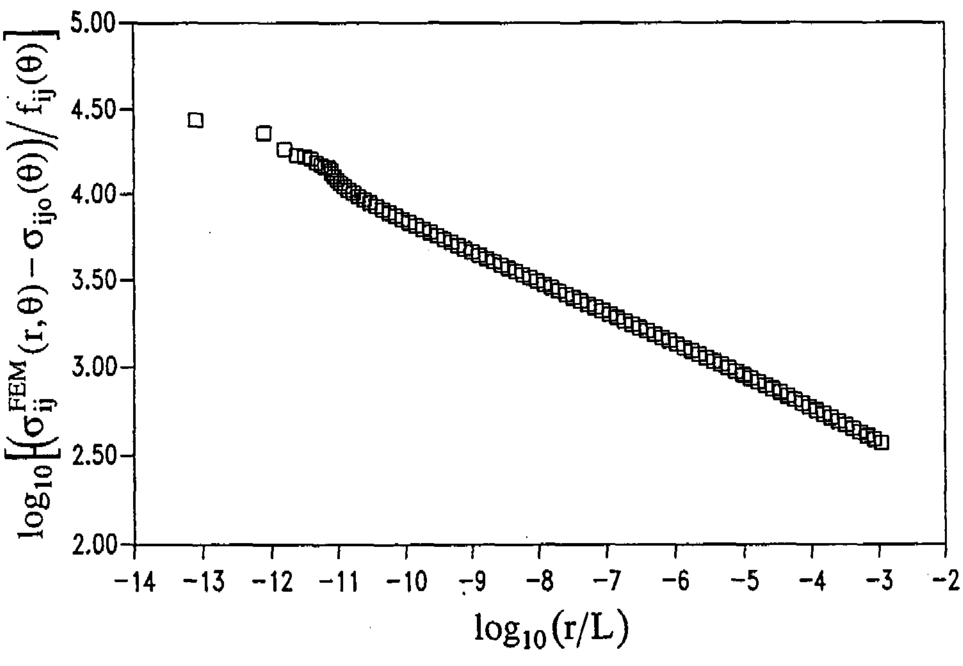

Fig. 3.5. Double logarithmic representation of the singular stress field.

The analytical parameters calculated for the model in Fig.3.2 are as follows.

$\omega = 0.1805$
$\sigma_o = 148.1$ MPa
$f_{xx} = f_{rr}(0) = 0.2616$
$f_{yy} = f_{\theta\theta}(0) = 1$
$f_{xy} = f_{r\theta}(0) = 0.2083$

Using the analytical parameters above and the numerical stress solutions, the double logarithmic relation in eq.(3.23) is plotted in Fig.3.5. In the results given in Fig.3.5, the residual stress field generated from the brazing process is included.
The plot shows a excellent linearity except for the region $r/L < 10^{-11}$. The curve was fitted to a first order function to determine the stress intensity factor K. The obtained K value was -109.6 MPa. The unit of the K is the same as that of stress due to the normalization of the coordinate in eq.(3.16).
The order of singularity ω can be also determined numerically from the fitted linear function. The relative discrepancy between the numerical-, and the analytical values of ω was about 0.16 %. This indicates that the order of singularity ω is hardly influenced by the thermal gradient induced by the transient thermal load.

In Fig.3.6, the spatial distribution of the interfacial stresses on the CFC side is shown. The σ_{yy} component of the stresses obtained from both finite element analysis and the theoretical model are plotted. It is seen that drastic stress intensifications near the free surface edge have occurred. In the bulk region distant from the free surface edge, the curve for the Yang's model deviates from the curve for the finite element analysis. This is mainly due to the fact that the analytical parameters in the theoretical model were derived satisfying the boundary conditions only near the singular point. In spite of this limitation, the two curves show relatively good agreement over the whole interface.

In Fig.3.7, the normal component of the interfacial stress (σ_{yy}) near the singular point is plotted again with magnification of 10^3 times. A good agreement between two curves is found in this region where $r/L < 10^{-3}$. Considering the whole range of the stress values, the difference between two curves seems to be minute. Approaching to the singular point, the magnitude of the stress increases further rapidly. But in real materials, it is thought that the stress would not go to infinity at the free surface boundary [14].
Fig.3.7 indicates that the theoretical model presented above can predict relatively accurate stress state near the singularity.

The axial-, and shear component of the interfacial stresses (σ_{xx} and σ_{xy}, respectively) on the CFC side are shown in Fig.3.8 and 3.9. The singular stress distribution is found near the free surface edge. As in the case of the normal stress component, the theoretical values deviate from the numerical values in the bulk region.

From Fig.3.7-3.9, it is seen that there exists a multiaxial stress state near the free boundary of the interface. The normal-, and shear stress components are secondary stress fields induced by the free surface effect. As each stress component has singular distribution near the free surface edge, a crack initiates effectively at this location by interaction between the intensified normal-, and shear components.

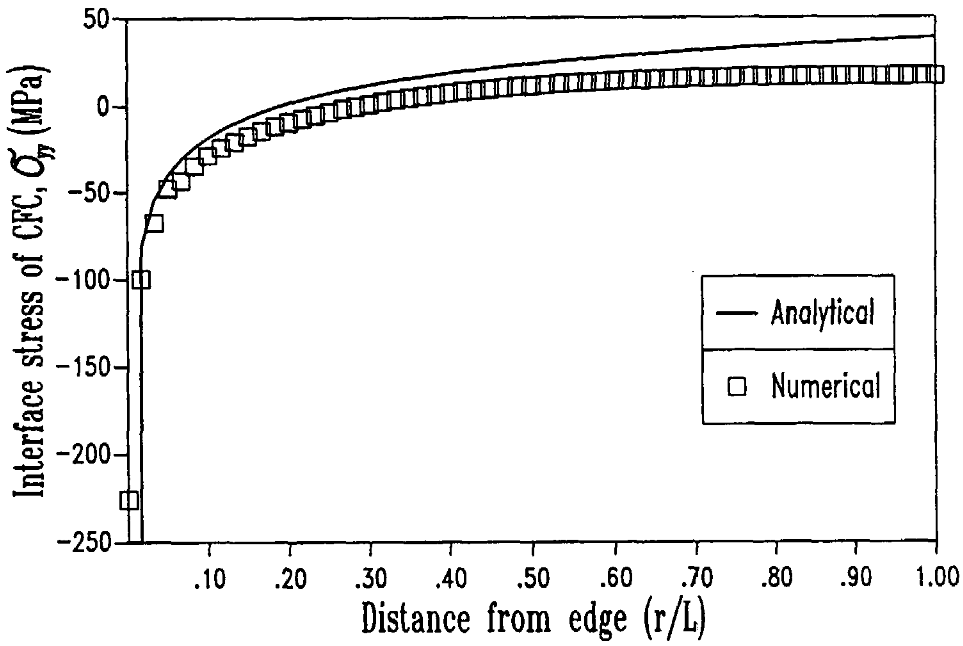

Fig. 3.6. Distribution of the normal stress component in the whole interface. ($\sigma_{yy} = \sigma_{\theta\theta}(r,0)$)

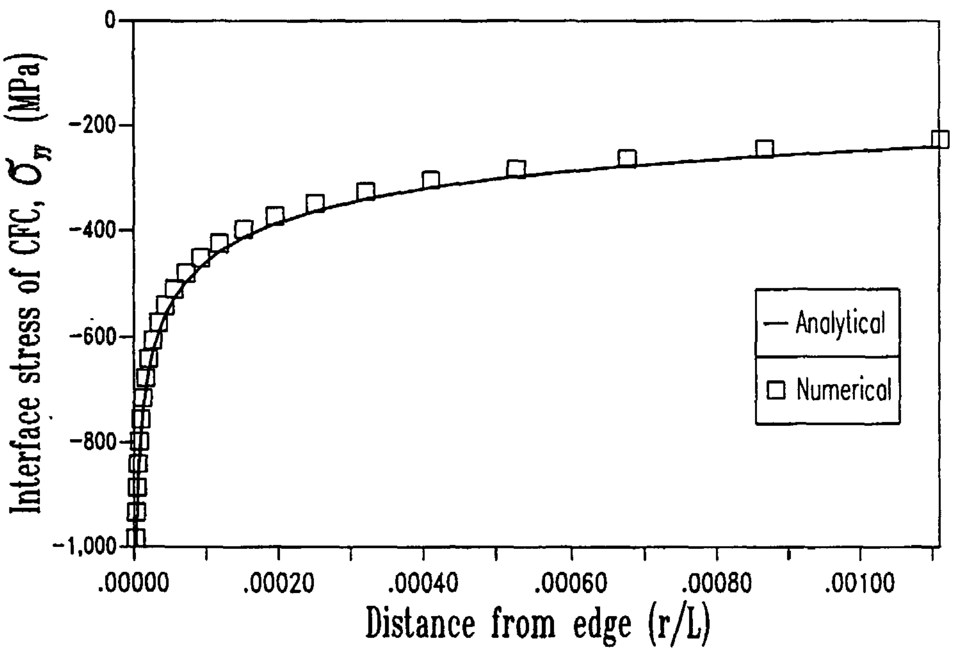

Fig. 3.7. Distribution of the normal stress component near the free surface edge of the interface. ($\sigma_{yy} = \sigma_{\theta\theta}(r,0)$)

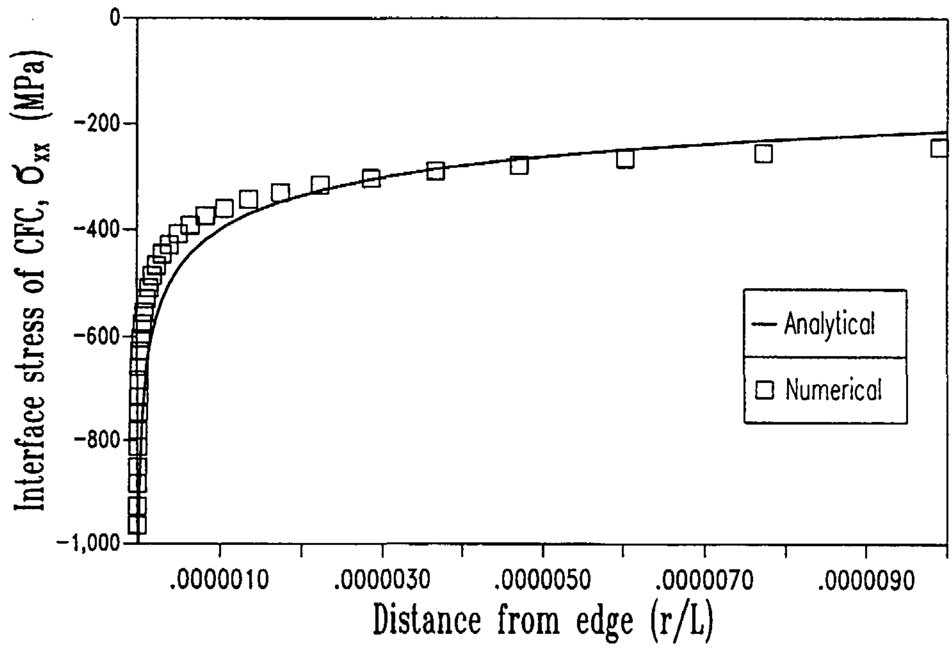

Fig. 3.8. Distribution of the axial stress component near the free surface edge of the interface. ($\sigma_{xx} = \sigma_{rr}(r,0)$)

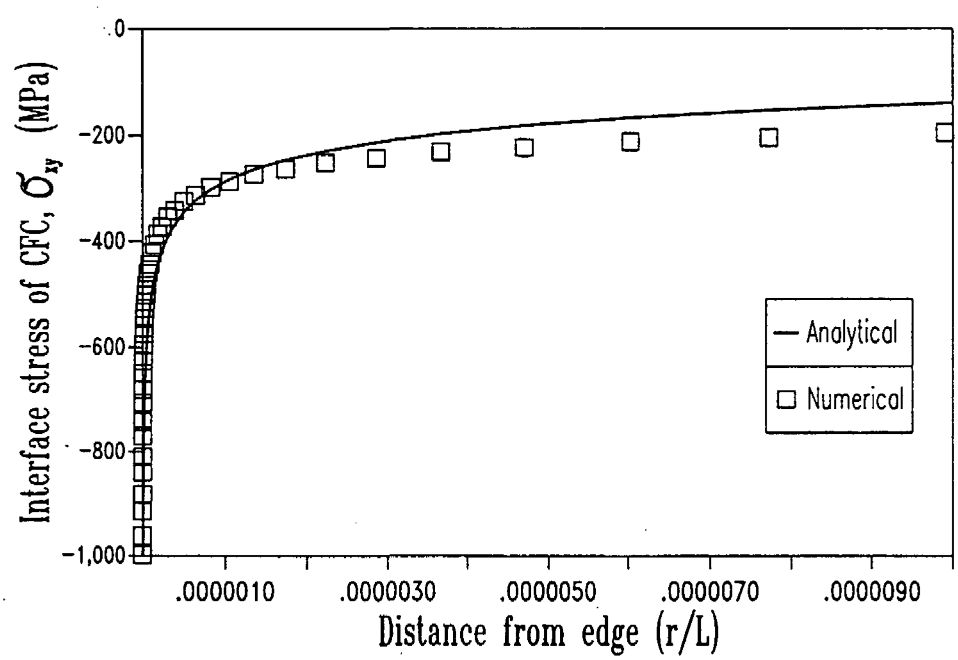

Fig. 3.9. Distribution of the shear stress component near the free surface edge of the interface. ($\sigma_{xy} = \sigma_{r\theta}(r,0)$)

To investigate the effect of a transient thermal gradient on the stress fields near the singularity, various transient HHF loadings were simulated. The applied power densities were 20-, 30-, 60- and 80 MW/m^2, respectively. The nature of the load history is identical to that shown in Fig.3.4. The pulse duration for each power density was taken in such a manner that the four different load conditions produce a common interface temperature. The pulse durations to meet this requirement were obtained numerically.
The reason why the interface temperature was taken as the reference temperature is that the temperature value near the interface is the most important loading parameter to determine the maximum thermal stress level in the joint.

In Fig.3.10, the vertical temperature profiles for the load-off points are shown. On the abscissa, the entire y coordinate of the joint is drawn.
The surface temperatures of the CFC are much higher than the interface temperature resulting in the considerable thermal gradients in upper half of the joint. The non-linear profiles of the temperatures represent the transient thermal distribution in the joint. The variation of the power densities caused dominant differences in the profiles only in the CFC region. It should be noticed that no other thermophysical process was considered in calculating these temperature fields except for the thermal conduction. Therefore, the numerical results for the range 3000 - 5000 °C are hypothetical.
The temperature profiles in Fig.3.10 (a) are shown again in Fig.3.10 (b) for the region ranging from 5 mm to 15 mm from the bottom of the joint. It is seen that the temperature profile curves, except for the region near the top surface and the bottom of the joint, can be approximated as linear functions. Then, a mean temperature gradient near the interface can be defined as the slop of the tangent line at the interface position of each curve.

The stress intensity factors of the stress singularity were calculated for these transient thermal load conditions. The behavior of the stress intensity factor K under the variation of thermal gradient across the interface is shown in Fig.3.11.
The strength of the stress singularity increases as the thermal gradient becomes steeper. The relative difference in the K values between the uniform heating and the HHF heating with 30 MW/m^2 is about 12.0 %. This means that the stress singularity in the joint will be just slightly affected by the transient thermal gradient in the range of fusion relevant HHF loads.

Using the stress intensity factors in Fig.3.11 together with the analytical parameters, the interfacial stress distributions near the singularity can be reproduced. In Fig.3.12, the normal component of the interfacial stress in CFC side is plotted for the region $r/L < 0.001$.
Increase of the stress due to the transient thermal gradient is found. The relative difference in the normal stress component at $r/L = 0.001$ between the uniform heating and the HHF load with 30 MW/m^2 is about 12.0 %.

In practice, CFC armor tile is bonded to TZM substrate by use of ductile filler metal. The flow behavior of the braze interlayer affects thermal stresses in the joint. Considering Cu braze layer, interfacial stress was calculated for the given transient HHF load to investigate the influence of the ductile braze on the interfacial stress field. The thickness of the interlayer was assumed to be 0.15 mm.
In Fig.3.14, the distribution of three stress components on the interface of CFC side is shown. The results for the bond interface including the braze interlayer is compared with that for the bond interface without interlayer. In the bulk region for $r/L > 0.2$, the braze layer does not influence the normal-, and shear stress components.

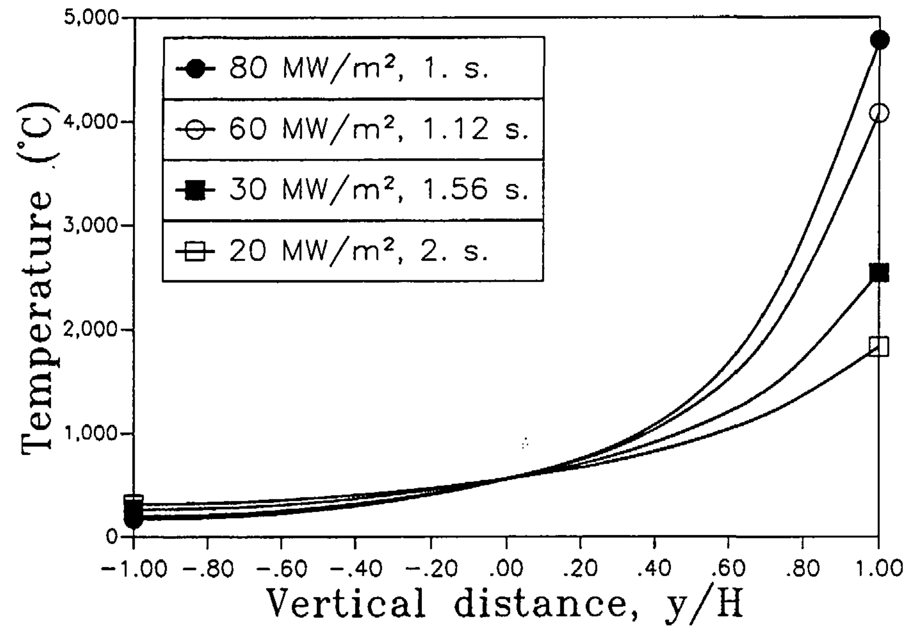

Fig. 3.10 (a)

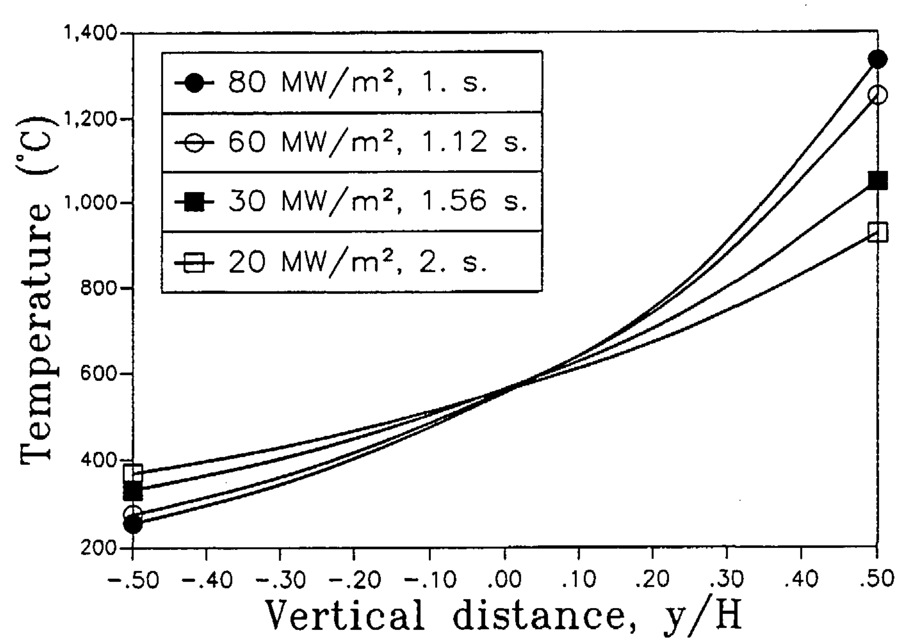

Fig. 3.10 (b)

Fig. 3.10. Vertical temperature profiles generated by the various thermal loads considered in the analysis.

(a) Whole range of the y coordinate.

(b) Middle range of the y coordinate.

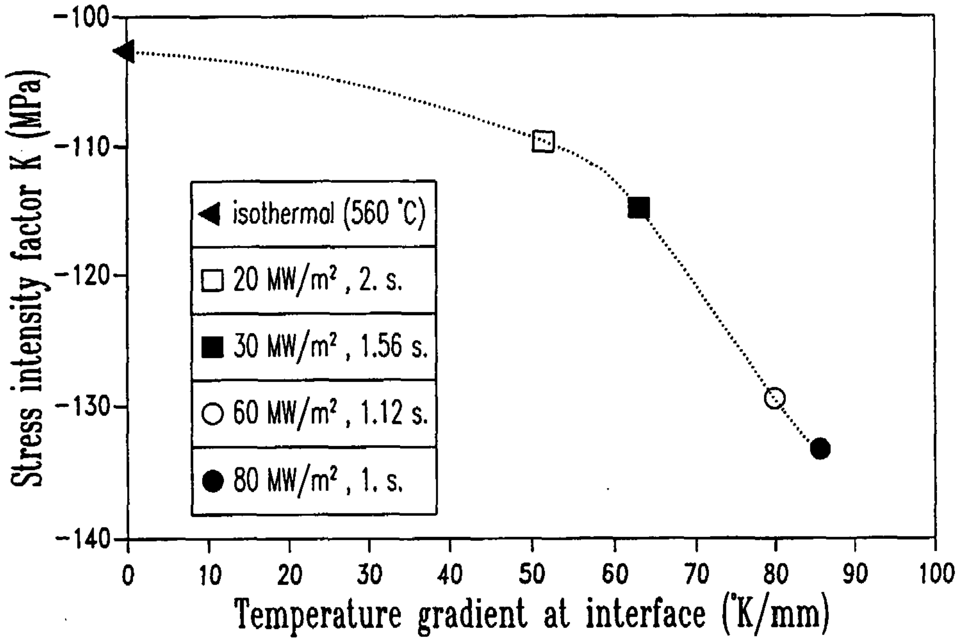

Fig. 3.11. Influence of the thermal gradient on the stress intensity factor.

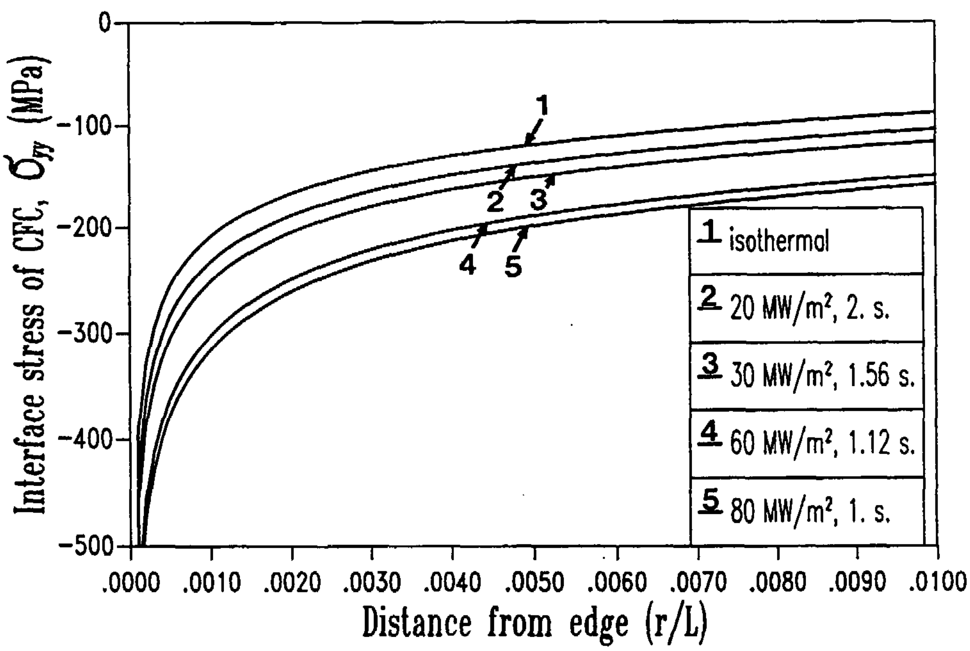

Fig. 3.12. Behavior of the singular stress field under the variation of the thermal gradient. (The normal stress component is plotted.)

The axial component, however, is relieved to some extent by the ductile braze.
In the presence of the ductile braze layer, the singular stress field becomes blunt since the stress level in this region is limited by the yield stress of the braze. In Fig.3.14, it is seen that the stress field in this region is disturbed by the plastic flow of the Cu interlayer.

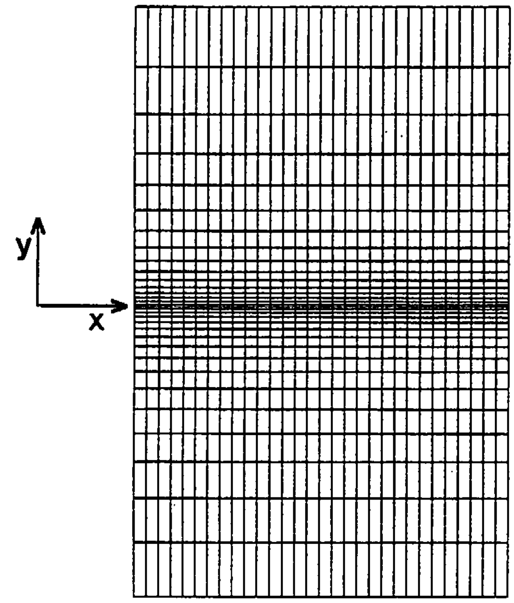

Fig. 3.13. Finite element mesh for the elasto-plastic analysis.

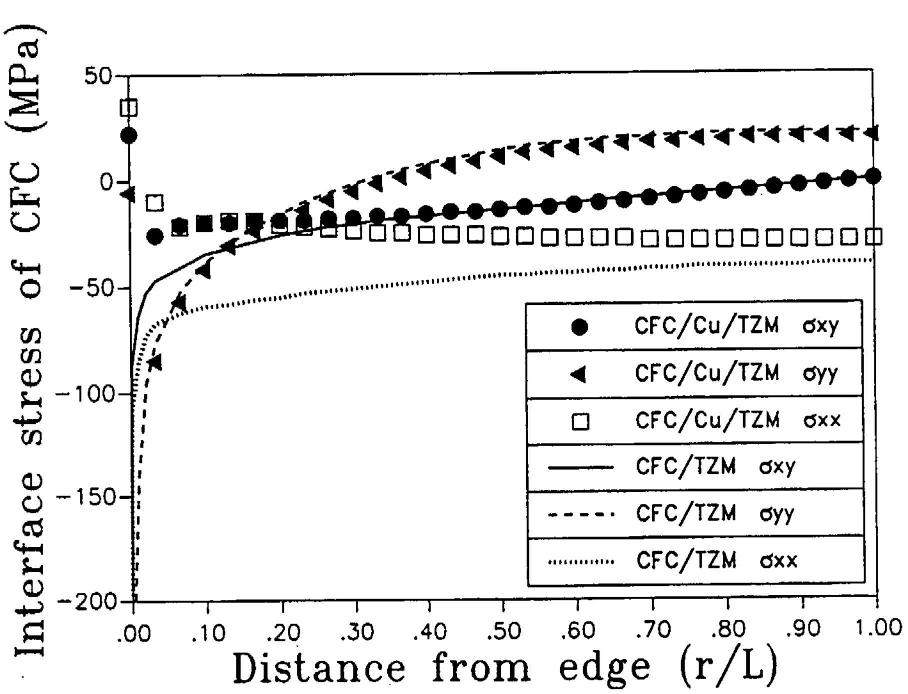

Fig. 3.14. Distribution of the actual stresses in the interface of CFC side. (power density of the HHF load: 20 MW/m^2, pulse duration: 2 seconds.)

5. Conclusions

The singular stress fields occuring near the free surface edge of the interface in a bond joint were characterized by introducing the linear elastic fracture mechanical approach. Together with the analytical procedures, finite element analysis was applied to calculate the stress solutions and determine the stress intensity factors. A two dimensional bi-material model consisting of CFC tile bonded to TZM substrate was investigated.
It was shown that the Yang's formulation could describe the singular stress fields in good approximation even for the non harmonic temperature fields caused by transient thermal load. The stress solutions for the singular field reproduced from the analytical parameters showed a good agreement with the numerical results.
High heat flux loading situation was simulated with different power densities and pulse durations in which various temperature gradients with a common interface temperature were generated. The degree of stress intensification near the singularity increased when the vertical temperature gradient became steeper. However, for the power density range of normal fusion operation, the influence of the thermal gradient on the strength of the stress singularity seemed to be negligible.
When there existed a ductile braze interlayer between the two materials, the singular stress field was disturbed due to the plastic flow of the interlayer.

6. Reference

[1] M. L. Williams, Bull. Seismol. Soc. Am. 49 (2) (1959), S. 199-204

[2] D.B. Bogy, Trans. ASME. J. Appl. Mech. 35 (1968), pp. 460-466

[3] K. Mizuno, K. Miyazawa, T. Suga, J. Faculty of Eng., Univ. Tokyo (B), Vol. XXXIX, No. 4 (1988), pp. 401-412

[4] J.P. Blancard, N.M. Ghoniem, Trans. ASME. J. Appl. Mech. 56 (1989), pp. 756-762

[5] R. Viola, E.B. Deksnis, JET-P (94) 54, JET Joint Undertaking (1994)

[6] A. Hassanein, Proc. ICFRM-5 (Clearwater, FL, USA, 1991), J. Nucl. Mater., 191-194 (1992), Part A, pp.499-502

[7] E. Zolti, Fus. Eng. Des. 18 (1991), pp. 163-171

[8] A. Hassanein, D.L. Smith, Proc. ICFRM-5 (Clearwater, FL, USA, 1991), J. Nucl. Mater., 191-194 (1992), Part A, pp.503-507

[9] S.P. Timoshenko, J.N. Goodier, "Theory of Elasticity" 3rd ed., Mcgraw-Hill Inc., New York, 1970

[10] D. Munz, T. Fett, Y.Y. Yang, Eng. Frac. Mech., 44 (2) (1993), pp. 185-194

[11] D. Munz, Y.Y. Yang, Trans. ASME. J. Appl. Mech. 59 (1992), pp. 857-861

[12] M. Fränkle, "Spannungssingularitäten in Zweistoffverbunden bei inhomogenen Temperaturfeldern", Diploma Thesis, Univ. Karlsruhe, (1994)

[13] "ABAQUS User's Manual 5.4", Hibbit, Karlson and Sorenson Inc., Providence, RI, USA., 1994

[14] D. Post, J.D. Wood, B. Han, V.J. Parks, F.P. Gerstle Jr., Trans. ASME. J. Appl. Mech. 61 (1994), pp. 192-198

Chapter 4. Plastic deformation of the ductile braze layer in a CFC/TZM bond joint under cyclic thermal loads

1. Introduction

In this chapter, thermomechanical behavior of the Cu braze layer in a CFC (carbon fiber reinforced carbon) to metal brazed joint is analyzed.

To indicate how the temperature dependence of the flow stress exerts influence on the thermomechanical behavior of the braze metal, the evolution of the stress and strain during the brazing process are presented.
For a assessment of fatigue behavior, cyclic thermal loadings are simulated for both cases of homogeneous and transient temperature changes. The evolution of the stress and strain in the interface and in the braze layer under these thermal cycling is investigated. The fatigue lifetime of the braze layer for the given thermal cycling conditions is estimated.

The microstructures of the copper braze in CFC/TZM bond joints are investigated after thermal cycling tests. The deformation damage and the slip mechanisms are discussed.

2. Theoretical model

2.1. Constitutive relations

The fundamentals of the model used for the copper braze is based on the isotropic, thermo-elasto-plastic material behavior.
Following considerations are developed under the assumption that total strain increment $d\varepsilon_{ij}$ can be devided into an elastic, plastic and thermal component as [1]

$$d\varepsilon_{ij} = d\varepsilon_{ij}^{el} + d\varepsilon_{ij}^{pl} + d\varepsilon_{ij}^{th}, \qquad (4.1)$$

where $d\varepsilon_{ij}$, $d\varepsilon_{ij}^{el}$, $d\varepsilon_{ij}^{pl}$ and $d\varepsilon_{ij}^{th}$ represent the increment of total, elastic, plastic and thermal strain tensor, respectively.

For an isotropic material, the thermal strain increment is given by

$$d\varepsilon_{ij}^{th} = \delta_{ij}\,\alpha(T - T_r) = \delta_{ij}\,\alpha\,\Delta T, \qquad (4.2)$$

where α is the coefficient of thermal expansion, T is the instantaneous temperature, T_r is the reference temperature and δ_{ij} is Kronecker Delta.

The elastic strain increment is combined with the stress increment $d\sigma_{ij}$ through the Hooke's law [2].

$$d\sigma_{ij} = D_{ijkl}\left(d\varepsilon_{ij} - d\varepsilon_{ij}^{pl} - d\varepsilon_{ij}^{th}\right) \tag{4.3}$$

with

$$D_{ijkl} = \mu\left(\delta_{ik}\delta_{jl} + \delta_{il}\delta_{jk}\right) + \lambda\delta_{ij}\delta_{kl} \tag{4.4}$$

and

$$\mu = \frac{E}{2(1+\nu)}, \quad \lambda = \frac{\nu E}{(1+\nu)(1-2\nu)} \tag{4.5-a, b}$$

μ is the shear modulus, λ is the Lamē's constant, E is the Young's modulus and ν is the Poisson's ratio.

The plastic contribution of the strain increment can be determined by applying an adequate yield criterion and flow rule.
The initial yielding for copper can be represented by the von Mises yield criterion [3,4],

$$F(\sigma_{ij}, \kappa, T) = \sigma_{eq} - \sigma_o(\kappa, T) = 0, \tag{4.6}$$

with

$$\sigma_{eq} = (3J_2')^{\frac{1}{2}} = \left(\frac{3}{2}\, S_{ij}\, S_{ij}\right)^{\frac{1}{2}} \quad \text{(von Mises equivalent stress)}, \tag{4.7}$$

$$S_{ij} = \sigma_{ij} - \frac{1}{3}\delta_{ij}\, \sigma_{kk}, \quad \text{(deviatoric stress tensor)} \tag{4.8}$$

where,

$F(\sigma_{ij}, \kappa, T)$: homogeneous function representing the yield surface in stress space,
J_2': second deviatoric stress invariant,
σ_o: uniaxial tensile yield stress,
κ: hardening parameter depending on the previous deformation history.

From the convexity and the normality conditions for the loading surface, associated flow rule is assumed to describe the flow process [5],

$$d\varepsilon_{ij}^{pl} = d\lambda\, \frac{\partial F}{\partial \sigma_{ij}}, \tag{4.9}$$

where $d\lambda$ is a scalar function of proportionality.
When isotropic strain hardening hypothesis is assumed to determine the subsequent development of the loading surface, following relation holds [1]

$$\kappa = \varepsilon_{eq}^{pl} = \int_0^{\varepsilon_{ij}^{pl}} \left(\frac{2}{3} \, d\varepsilon_{ij}^{pl} \, d\varepsilon_{ij}^{pl} \right)^{\frac{1}{2}}, \tag{4.10}$$

where ε_{eq}^{pl} represents the equivalent plastic strain.

In the finite element program based on the displacement, the stress increment is to be described as a function of $d\varepsilon_{ij}$, $d\varepsilon_{ij}^{th}$ and state variables. Therefore the aim of task is to eliminate the term $d\varepsilon_{ij}^{pl}$ from eq.(4.3) using the relation eq.(4.6), (4.9) and (4.10).

Some useful relations are listed in table 4.1.

Table 4.1

$$D_{ijkl} \, S_{kl} = 2\mu \, S_{ij} \quad \text{oder} \quad S_{ij} \, D_{ijkl} = 2\mu \, S_{kl}$$

$$\frac{\partial F(\sigma_{ij}, \kappa, T)}{\partial \sigma_{ij}} = \frac{3}{2} \frac{S_{ij}}{\sigma_{eq}}$$

$$d\varepsilon_{eq}^{pl} = \int_0^{\varepsilon_{ij}^{pl}} \left(\frac{2}{3} \, d\varepsilon_{ij}^{pl} \, d\varepsilon_{ij}^{pl} \right)^{\frac{1}{2}} = \left(\frac{2}{3} d\lambda^2 \frac{\partial F}{\partial \sigma_{ij}} \frac{\partial F}{\partial \sigma_{ij}} \right)^{\frac{1}{2}}$$
$$= \left(\frac{2}{3} d\lambda^2 \frac{3}{2} \frac{S_{ij}}{\sigma_{eq}} \frac{3}{2} \frac{S_{ij}}{\sigma_{eq}} \right)^{\frac{1}{2}} = \left(d\lambda^2 \right)^{\frac{1}{2}} = d\lambda$$

$$d\sigma_{eq} = \frac{3}{2} \frac{S_{ij}}{\sigma_{eq}} dS_{ij} = \frac{3}{2} \frac{S_{ij}}{\sigma_{eq}} d\sigma_{ij}.$$

A variation of plastic strain or temperature in a plastic state (i.e. $F = \sigma_{eq} - \sigma_0 = 0$) will lead to a change in σ_o as follows

$$d\sigma_o\left(\varepsilon_{eq}^{pl}, T\right) = \left(\frac{\partial \sigma_o}{\partial \varepsilon_{eq}^{pl}} \right)_T d\varepsilon_{eq}^{pl} + \left(\frac{\partial \sigma_o}{\partial T} \right)_{\varepsilon_{eq}^{pl}} dT = d\sigma_{eq} = \frac{3}{2} \frac{S_{ij}}{\sigma_{eq}} d\sigma_{ij}$$
$$= \frac{3}{2} \frac{S_{ij}}{\sigma_{eq}} D_{ijkl} \left(d\tilde{\varepsilon}_{kl} - d\lambda \frac{\partial F}{\partial \sigma_{kl}} \right) = 3\mu \frac{S_{kl}}{\sigma_{eq}} d\tilde{\varepsilon}_{kl} - 3\mu \, d\lambda, \tag{4.11}$$

where $d\tilde{\varepsilon}_{kl} = d\varepsilon_{kl} - d\varepsilon_{kl}^{th}$.

From eq.(4.11) and considering $d\lambda = d\varepsilon_{eq}^{pl}$, $d\lambda$ can be represented by following equations

$$d\lambda\left[\left(\frac{\partial\sigma_o}{\partial\varepsilon_{eq}^{pl}}\right)_T + 3\mu\right] = 3\mu\frac{S_{kl}}{\sigma_{eq}}d\tilde{\varepsilon}_{kl} - \left(\frac{\partial\sigma_o}{\partial T}\right)_{\varepsilon_{eq}^{pl}} dT \tag{4.12}$$

or

$$d\lambda = \frac{3\mu}{\left(\frac{\partial\sigma_o}{\partial\varepsilon_{eq}^{pl}}\right)_T + 3\mu}\frac{S_{mn}}{\sigma_{eq}}d\tilde{\varepsilon}_{mn} - \frac{\left(\frac{\partial\sigma_o}{\partial T}\right)_{\varepsilon_{eq}^{pl}}}{\left(\frac{\partial\sigma_o}{\partial\varepsilon_{eq}^{pl}}\right)_T + 3\mu} dT \tag{4.13}$$

Substituting eq.(4.13) and (4.9) into eq.(4.3) gives

$$d\sigma_{ij} = D_{ijkl}d\tilde{\varepsilon}_{kl} - D_{ijkl}\left[\frac{3\mu}{\left(\frac{\partial\sigma_o}{\partial\varepsilon_{eq}^{pl}}\right)_T + 3\mu}\frac{S_{mn}}{\sigma_{eq}}d\tilde{\varepsilon}_{mn} - \frac{\left(\frac{\partial\sigma_o}{\partial T}\right)_{\varepsilon_{eq}^{pl}}}{\left(\frac{\partial\sigma_o}{\partial\varepsilon_{eq}^{pl}}\right)_T + 3\mu} dT\right]\frac{3}{2}\frac{S_{kl}}{\sigma_{eq}} \tag{4.14}$$

$$= D_{ijkl}d\tilde{\varepsilon}_{kl} - 3\mu\, S_{kl}\left[\frac{3\mu}{\left(\frac{\partial\sigma_o}{\partial\varepsilon_{eq}^{pl}}\right)_T + 3\mu}\frac{S_{mn}}{\sigma_{eq}}d\tilde{\varepsilon}_{mn} - \frac{\left(\frac{\partial\sigma_o}{\partial T}\right)_{\varepsilon_{eq}^{pl}}}{\left(\frac{\partial\sigma_o}{\partial\varepsilon_{eq}^{pl}}\right)_T + 3\mu} dT\right] \tag{4.15}$$

$$= \left[D_{ijkl} - \frac{9\mu^2}{\left(\frac{\partial\sigma_o}{\partial\varepsilon_{eq}^{pl}}\right)_T + 3\mu}\frac{S_{ij}}{\sigma_{eq}}\frac{S_{kl}}{\sigma_{eq}}\right]d\tilde{\varepsilon}_{kl} + \frac{3\mu\left(\frac{\partial\sigma_o}{\partial T}\right)_{\varepsilon_{eq}^{pl}} dT}{\left(\frac{\partial\sigma_o}{\partial\varepsilon_{eq}^{pl}}\right)_T + 3\mu}\frac{S_{ij}}{\sigma_{eq}} \tag{4.16}$$

Due to $S_{ij}\,\delta_{ij} = 0$ $\left(d\varepsilon_{kl}^{th} = \delta_{kl}\,\alpha\, dT\right)$, eq.(4.16) can be rearranged as

$$d\sigma_{ij} = \left[D_{ijkl} - \frac{9\mu^2}{\left(\frac{\partial\sigma_o}{\partial\varepsilon_{eq}^{pl}}\right)_T + 3\mu}\frac{S_{ij}}{\sigma_{eq}}\frac{S_{kl}}{\sigma_{eq}}\right]d\varepsilon_{kl} - \left[D_{ijkl}\,\alpha\,\delta_{kl} - \frac{3\mu\left(\frac{\partial\sigma_o}{\partial T}\right)_{\varepsilon_{eq}^{pl}}}{\left(\frac{\partial\sigma_o}{\partial\varepsilon_{eq}^{pl}}\right)_T + 3\mu}\frac{S_{ij}}{\sigma_{eq}}\right]dT \tag{4.17}$$

2.2. Fatigue lifetime

In Fig.4.1, the geometry of the two dimensional CFC/Cu/TZM joint model used for the analysis is shown.

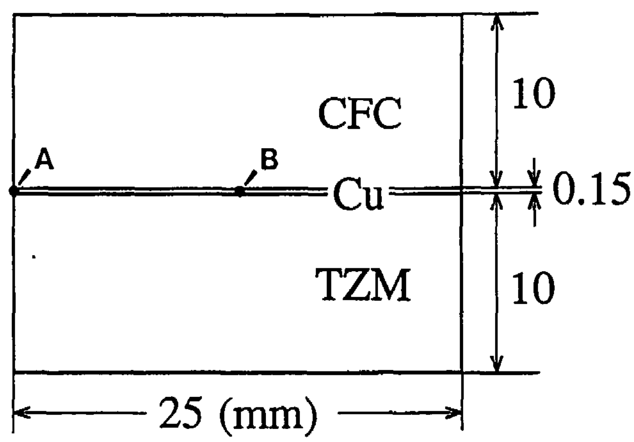

Fig. 4.1. Geometry of the CFC/Cu/TZM joint model used for the numerical analysis.

Under a uniform temperature change, the thermal stress in the thin ductile Cu interlayer stems from following contributions, respectively [6].

i) Strains due to the thermal expansion mismatch between the braze itself and the adherends
ii) Strains due to the thermal expansion mismatch between the adherends relative to each other

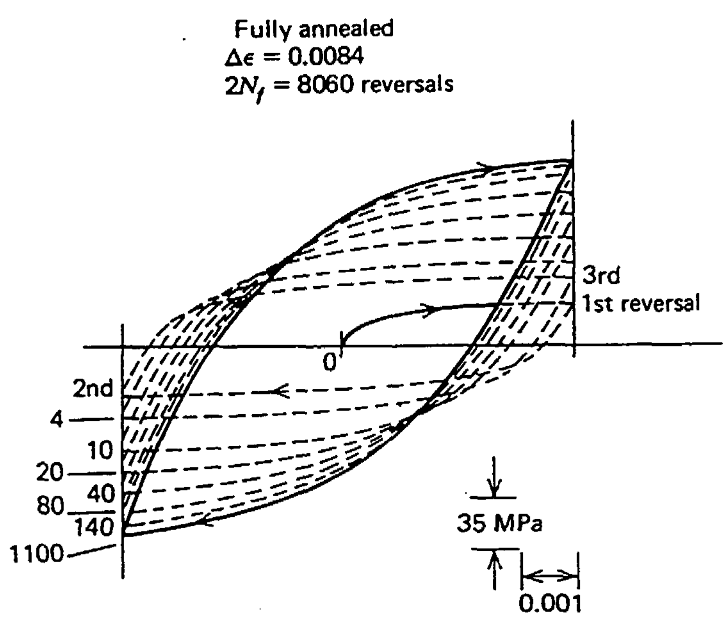

Fig. 4.2. Hysteresis loops for the cyclic stress-strain response of the annealed copper.

When the thermal strains described above are continually imposed on the braze layer under cyclic temperature reversals with a temperature amplitude of several hundred degree Celsius, this situation may correspond the high amplitude, low cycle fatigue.
The hysteresis loops in Fig.4.2 [7] show typical changes with increasing cycles in the cyclic stress-strain response of the annealed copper.
The hysteresis loops after only a few cycles become symmetric in tension and compression. This behavior of the annealed copper implies that the yield surface would expand under cyclic loading. To simplify the theoretical treatment, an isotropic hardening model is applied to the copper braze layer.
In low cycle fatigue, the stresses and strains are no longer linearly related. In general, a strain-based approaches are used in this regime.

According to [8], the fatigue lifetime of annealed OFHC copper is given by following formula.

$$\begin{aligned}\Delta\varepsilon^{t} &= \Delta\varepsilon^{el} + \Delta\varepsilon^{pl} \\ &= A\cdot N_f^{-0.12} + B\cdot N_f^{-0.6},\end{aligned} \qquad (4.18)$$

$$A = \frac{R_m - \bar{\sigma}}{E} A_o \qquad (4.19\text{-a})$$

$$B = \ln\left(\frac{1}{1-Z}\right)^{0,6} B_o, \qquad (4.19\text{-b})$$

$A_o = 6.0939,\ B_o = 0.155,$

where $\Delta\varepsilon^{t}$: total strain range, $\Delta\varepsilon^{el}$: elastic strain range, $\Delta\varepsilon^{pl}$: plastic strain range,
N_f: number of cycles to failure, R_m: ultimate tensile stress, $\bar{\sigma}$: mean stress of a cycle,
E: Young's modulus, Z: reduction in area after tensile fracture.

The strain-life relation given in eq.(4.18) was obtained from uniaxial fatigue tests. A multiaxial fatigue theory is required to apply eq.(4.18) to a complex stress state. Based on the equivalent strain range criterion, the ASME code provides a method for multiaxial cases [9-10].

$$\Delta\varepsilon_{eq}(t) = max\left\{\frac{\sqrt{2}}{3}\left[(\Delta\varepsilon_1(t)-\Delta\varepsilon_2(t))^2 + (\Delta\varepsilon_2(t)-\Delta\varepsilon_3(t))^2 + (\Delta\varepsilon_3(t)-\Delta\varepsilon_1(t))^2\right]^{1/2}\right\} \qquad (4.20)$$

where $\Delta\varepsilon_i(t) = \varepsilon_i(t_r) - \varepsilon_i(t)$
$\varepsilon_i(t_r)$: principal strain at the reference time t_r
$\varepsilon_i(t)$: principal strain at time t
$(\varepsilon_1 > \varepsilon_2 > \varepsilon_3)$

The fatigue life of the braze layer under thermal cycling can then be estimated using this procedure.

3. Computation

The non-isothermal elastoplastic problem was solved using the finite element code ABAQUS. The computational strategies for the integration of strain increments are found in [11].
In Fig.4.3, the finite element mesh for the model is shown. Due to the symmetry, only the left half part was considered. 8-noded isoparametric quadrilateral elements were used for the thermal and stress analyses assuming the generalized plane strain condition. 960 elements and 3251 node points were generated.

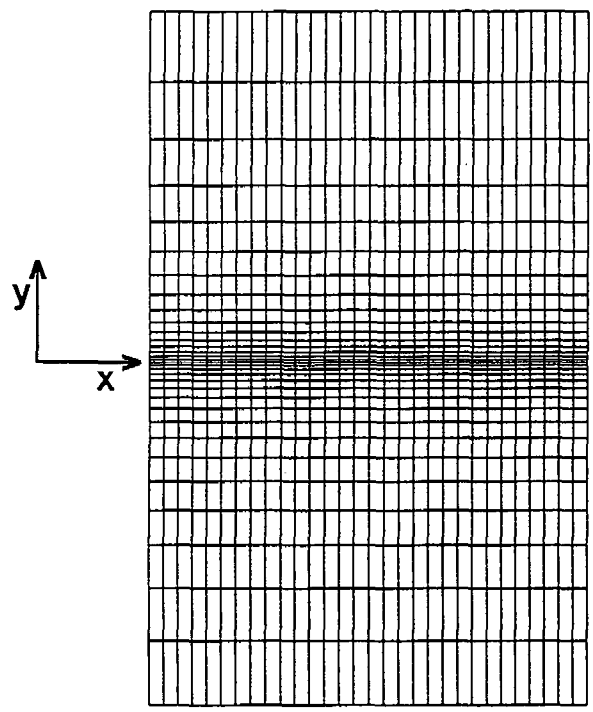

Fig. 4.3. Finite element mesh for the elasto-plastic analysis.

Some selected material properties of the CFC, TZM and copper are shown in Fig.4.4 and 4.5 [12]. The symbols // and ⊥ represent the in-plane and the normal direction to layered plies of the CFC.
All material properties were given as a function of temperature in the analysis. The time dependent effect was not included.

The simulation of the brazing process was carried out prior to the thermal cycling steps to generate the residual stress field on which the following thermal stresses are superposed. Firstly, it was assumed that the CFC tile is brazed on TZM body with Cu foil at 1070 °C (solidus temperature of copper) in a stress free state. Then the joint is cooled down homogeneously to room temperature in which the joint exists in a residually stressed state. Subsequently, the joint is subjected to sequential temperature changes to simulate the cyclic thermal loading.

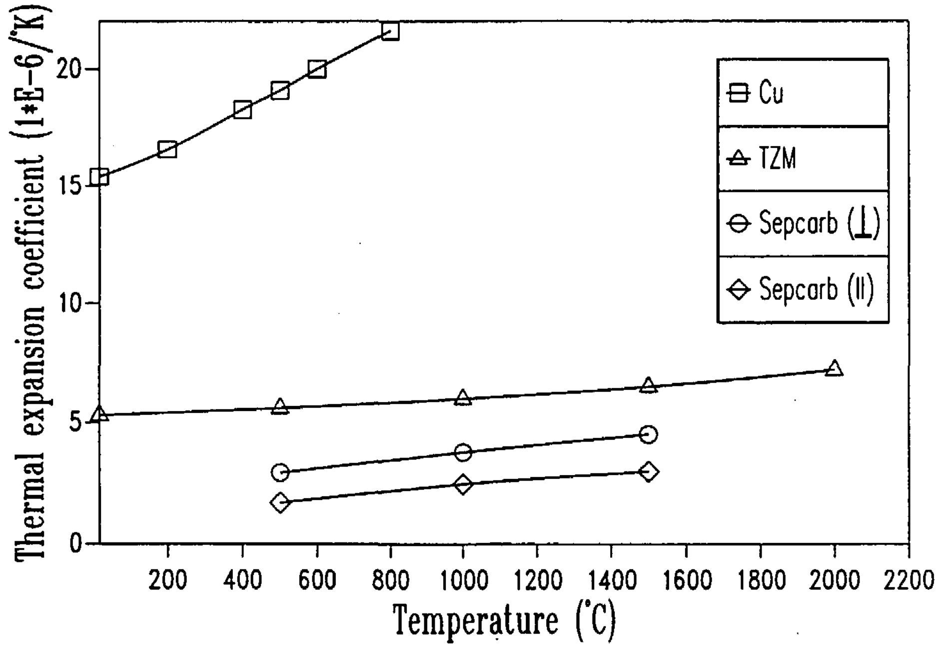

Fig. 4.4. Coefficient of thermal expansion for the materials considered (CFC (Sepcarb N112), OFHC Cu and TZM).

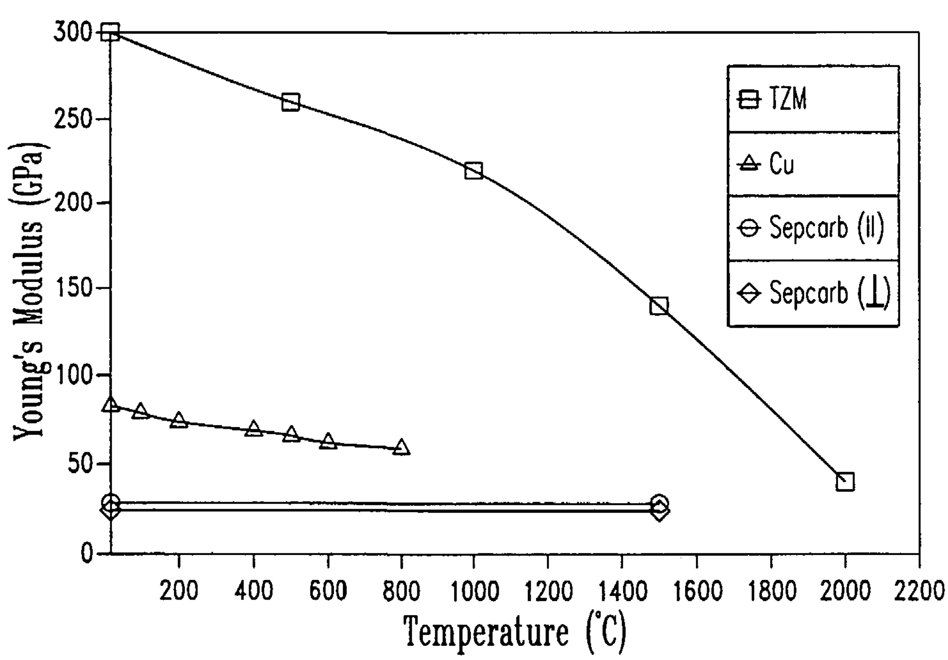

Fig. 4.5. Modulus of elasticity for the materials considered (CFC (Sepcarb N112), OFHC Cu and TZM).

4. Experiments

The sample element for the thermal cycling tests is already shown in Fig.2.7 in chapter 2.

The CFC/TZM pairs were brazed at 1150 °C in a vacuum atmosphere. A copper alloy Cu1Cr was used as the filler metal. The thickness of the braze layer after bonding was 130 - 150 μm. The alloying of Cr in Cu was intended to form a stable carbide reaction film which should contribute to strong adhesion between the adherends.
Thermal fatigue tests were conducted with ten cycles of HHF pulses. The load parameters are listed in table 2.3 in chapter 2.
In addition, thermal cycling tests were also carried out in a vacuum furnace. Ten cycles of temperature change between 20 °C and 600 °C were imposed.
The period of one thermal cycle in the HHF tests was in the order of some minutes whereas it took several hours in case of the furnace tests.

5. Results and discussion

5.1. Brazing process simulation

In Fig.4.6, the yield stress of OFHC Cu is presented as a function of both temperature and strain. The initial yield stress of the annealed copper shows a weak temperature dependence. On the contrary, the cold worked copper experiences considerable mechanical softening by thermal recovery and recrystallization. Above 600 °C, there exists no significant work hardening effect.

Fig.4.7 shows the stress-strain relation of the OFHC copper for two selected temperatures. The data in Fig.4.7 were obtained from uniaxial tensile tests. At 600 °C, copper shows a nearly perfect plasticity. For the numerical stress analysis, the input data were approximated to piecewise linear segments.

Fig.4.8 shows the deformed structure of the brazed joint at room temperature after the brazing process. The step formed at the free surface edge of the interface suggests that a large plastic deformation has occured in the Cu braze.

The flow behavior of the braze layer is significantly influenced by the surrounding temperature as can be seen in Fig.4.6. The loading path of the thermal history is important for incremental stress evolution in the braze due to the interplay between temperature and strain. Since the strength of the joint is mainly determined by the residual stress which is again affected by the plastic deformation of the braze, it is essential to analyze the development of the plastic flow in the braze layer during the brazing process.
The von Mises equivalent stress σ_{eq} and the equivalent plastic strain, ε_{eq}^{pl}, were investigated for the cooldown process from the brazing temperature. Uniform temperature change with a constant cooling rate was assumed for the brazing simulation.

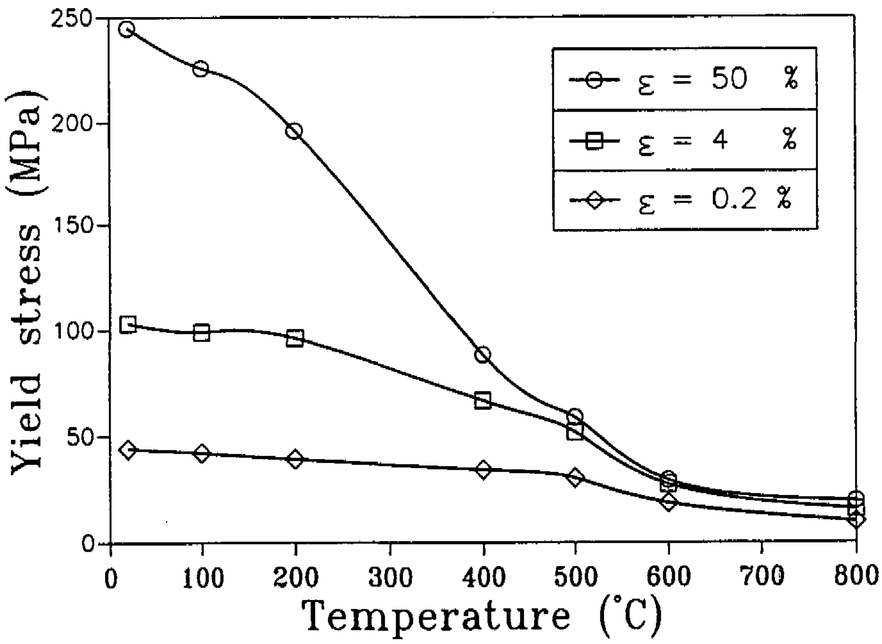

Fig. 4.6. Yield stress of OFHC Cu as a function of temperature. (Yield stress values are plotted for three different strains.)

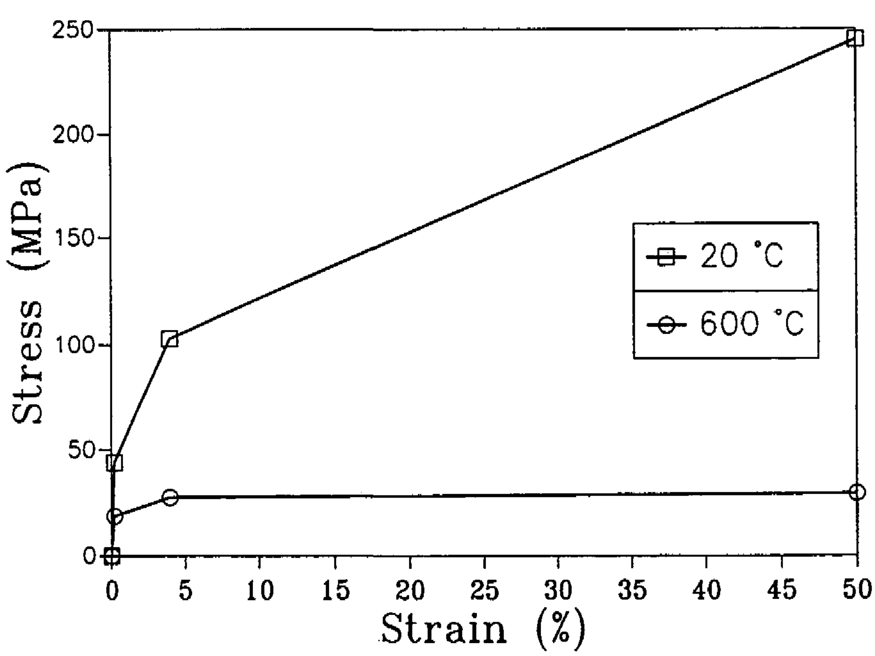

Fig. 4.7. Stress-strain relation of OFHC Cu for the temperatures of 20 °C and 600 °C.

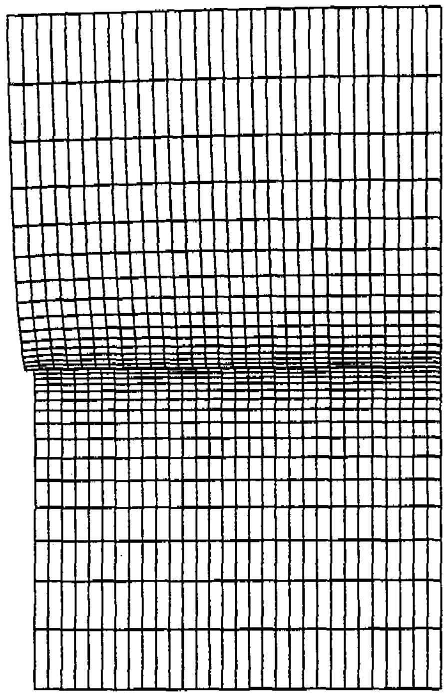

Fig. 4.8. Deformed structure of the model after the brazing process.
(The displacement is magnified by 20 times.)

Fig.4.9 shows the ε_{eq}^{pl} developing at the edge and at the center of the braze layer. These positions are indicated in Fig.4.1 (point A and B). The abscissa ranges from the solidus temperature of the copper (1070 °C) to room temperature. Due to the proportional misfit in thermal expansion, the edge region deformed much more than the center.
At the edge of the braze layer, the history of the strain shows a nearly bilinear behavior. The rapid increase of the plastic strain above 600 °C can be understood from the complete softening of the braze in this temperature range.

The evolution of σ_{eq} is shown in Fig.4.10. The stress field in the braze layer is not much inhomogeneous in spite of the large difference in the integrated local strain. Most of the residual stress is generated below ca. 600°C.

5.2. Uniform thermal cycling simulation

A cyclic thermal loading was simulated to investigate the fatigue behavior of the copper braze in the joint. Fig.4.11 shows the assumed loading history consisting of uniform temperature changes between room temperature and 600 °C. This represents a slow heat cycling in a furnace.

Fig.4.12 shows the change of three stress components at the braze center during the thermal cycling. Due to the finite dimension of the model, the stress state is not uniaxial.

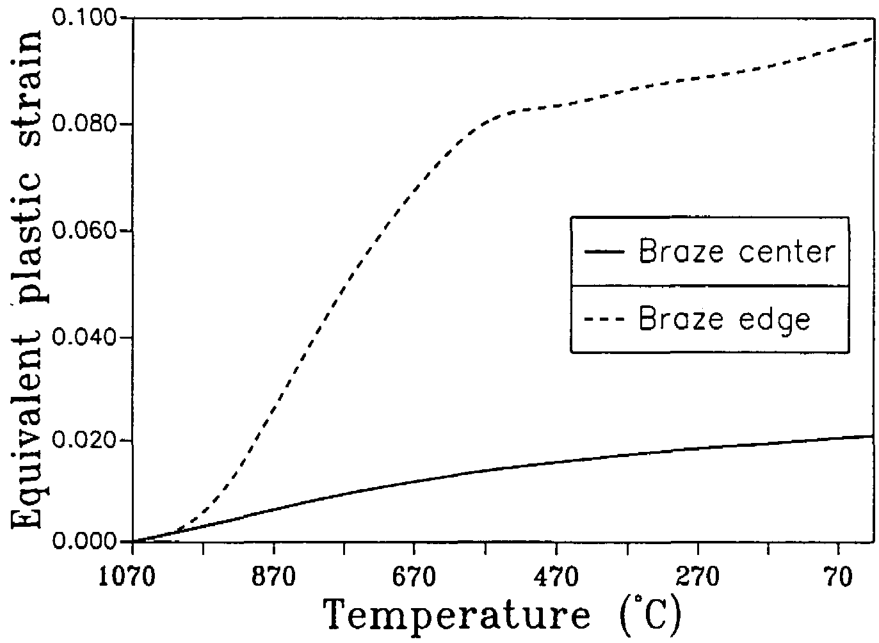

Fig. 4.9. Development of the equivalent plastic strain in the braze layer during the brazing process.

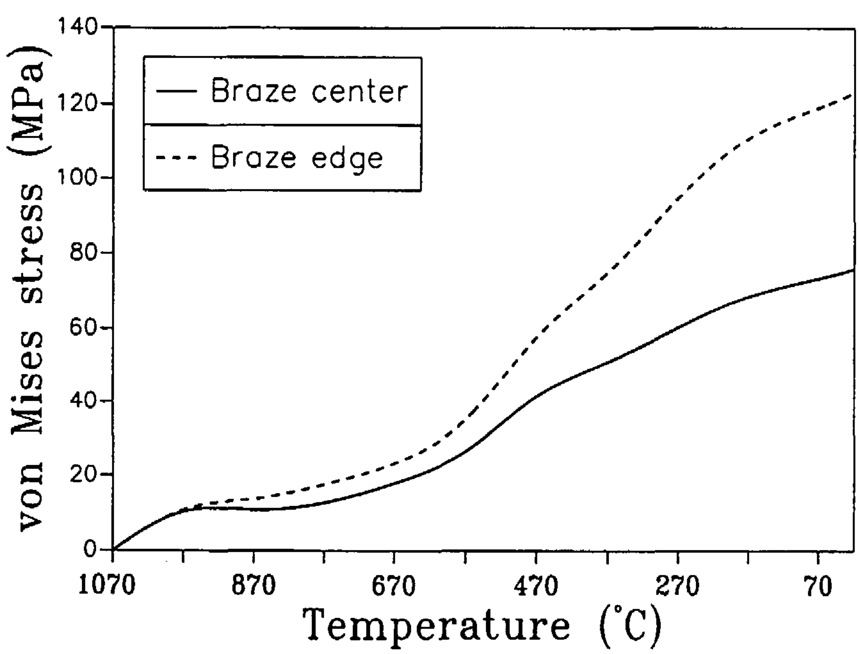

Fig. 4.10. Development of the von Mises equivalent stress in the braze layer during the brazing process.

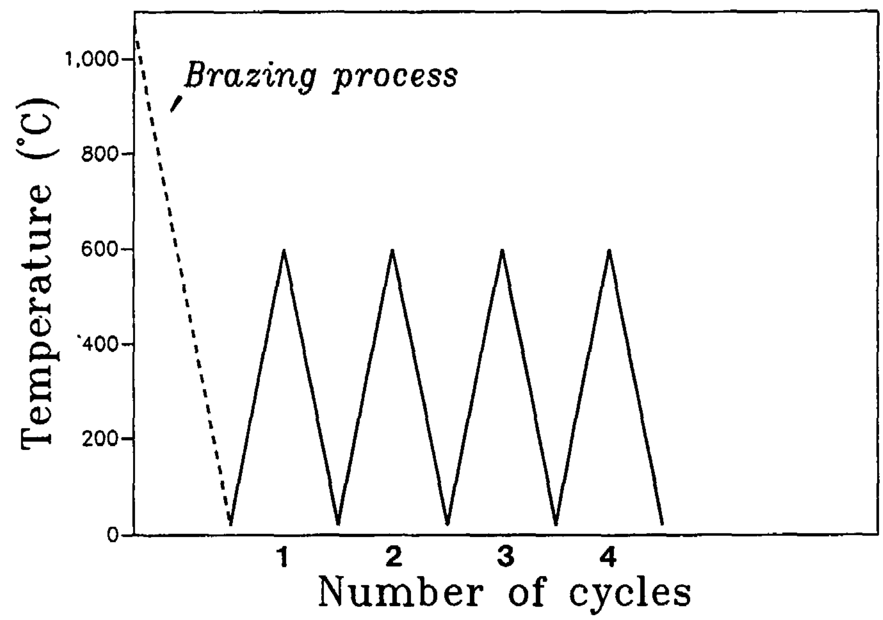

Fig. 4.11. Thermal load history applied for the thermal fatigue analysis.
(uniform thermal cycling. temperature change: 20 °C ⇔ 600 °C)

Since the bulk thermal stress is mainly caused by the mismatch of thermal expansion in axial direction, the axial stress component σ_{xx} is much more dominant than the normal component σ_{yy}. The axial component shows a reversed fatigue mode whereas the normal component shows a repeated fatigue mode. After the first three cycles, the stress amplitudes are almost the same. This premature saturation is thought to result from thermal softening of the braze metal.

Fig.4.13 shows the change of stress components at the free surface edge of the braze. The major contribution stems from the normal stress component. This is due to the deformation geometry of the free surface boundary. The axial component σ_{xx} and the normal component σ_{yy} show a mixed mode of repeated and reversed variations whereas the shear component σ_{xy} shows a nearly repeated mode. The stress amplitude of the three components reached a saturation in three cycles.

It should be noticed that the maximum and the minimum of each stress component in Fig.4.12 and Fig.4.13 do not occur simultaneously. Mismatch of these peak positions causes a complicated cyclic history of von Mises equivalent stress σ_{eq} as shown in Fig.4.14. The σ_{eq} for the braze edge shows a saw-tooth shape where a second peak follows a initial peak after load reversals. This feature is more significant for the case of the braze center resulting in doubled stress cycles.

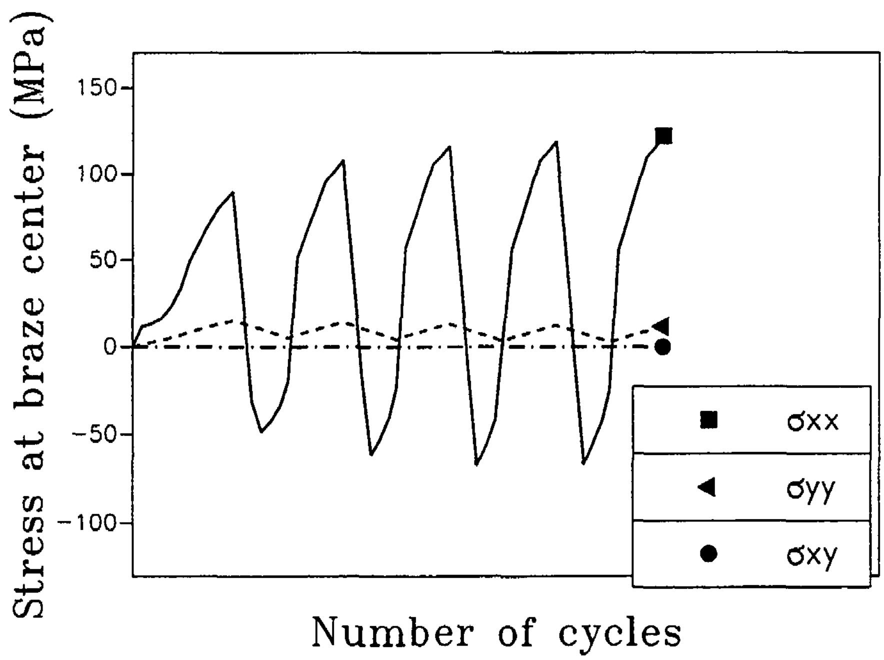

Fig. 4.12. Behavior of the stress components under the uniform thermal cycling. (braze center)

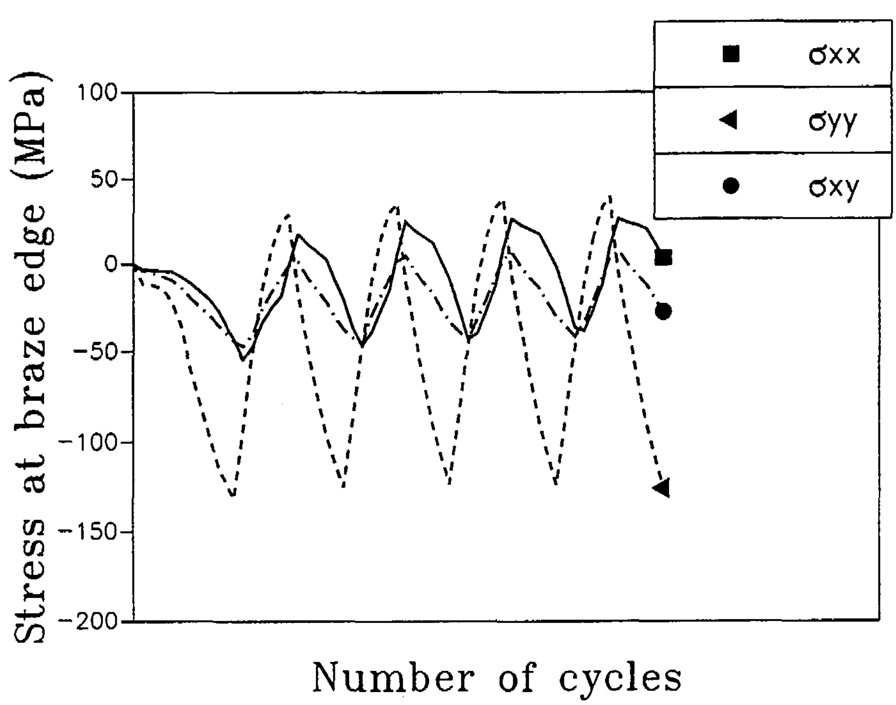

Fig. 4.13. Behavior of the stress components under the uniform thermal cycling. (braze edge)

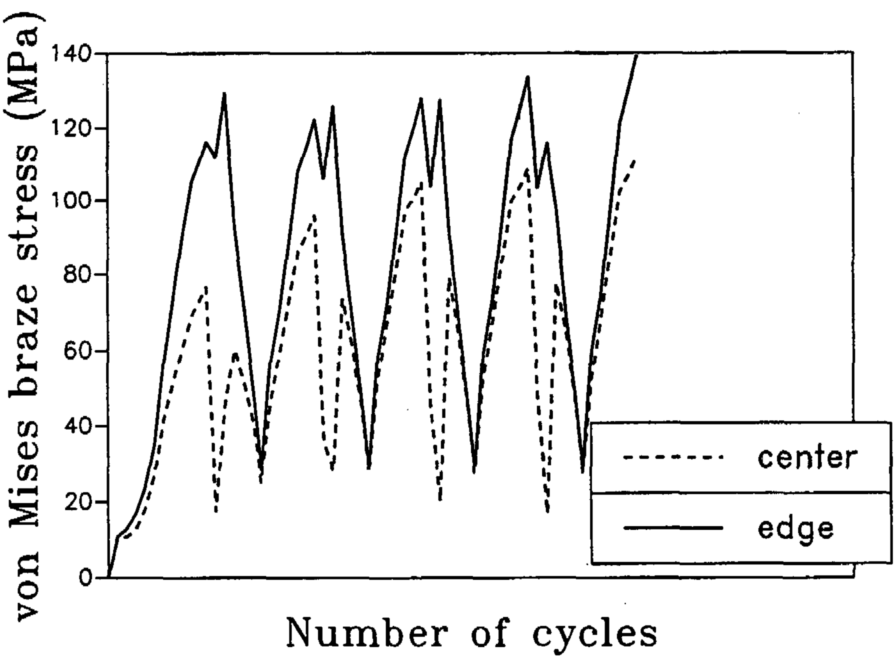

Fig. 4.14. Behavior of the von Mises stress in the braze layer under the uniform thermal cycling.

Fig.4.15 and Fig.4.16 show the time history of principal strain components at the braze center and at the free surface edge of the braze, respectively.
The amplitude of the principal strains for the braze center is nearly constant. This situation corresponds to a strain range controlled fatigue. There occurs no significant change between the cycles.
The principal strains for the braze edge increase cycle to cycle keeping their amplitude constant. This may be due to the ratcheting effect. The magnitude of the principal strains for the edge region is greater than for the center region.
The increment of equivalent plastic strain $\Delta\varepsilon_{eq}^{pl}$ was nearly constant after the first 2 cycles. The numerically determined value of $\Delta\varepsilon_{eq}^{pl}$ was 1 % for the braze edge and 0.59 % for the braze center.

5.3. High heat flux cycling simulation

When the brazed joint is subjected to fusion operations, it experiences characteristic thermal loads consisting of cyclic HHF pulses. The loading nature of the braze layer under such a transient HHF pulse may differ from that of a homogeneous temperature change.
To investigate the loading feature of the braze layer under cyclic HHF loads, a transient thermal cycling condition with four heat pulses of 20 MW/m^2 on the CFC surface for 2.1 seconds was simulated. Active cooling was assumed. The applied thermal loading history is given in Fig.4.17.

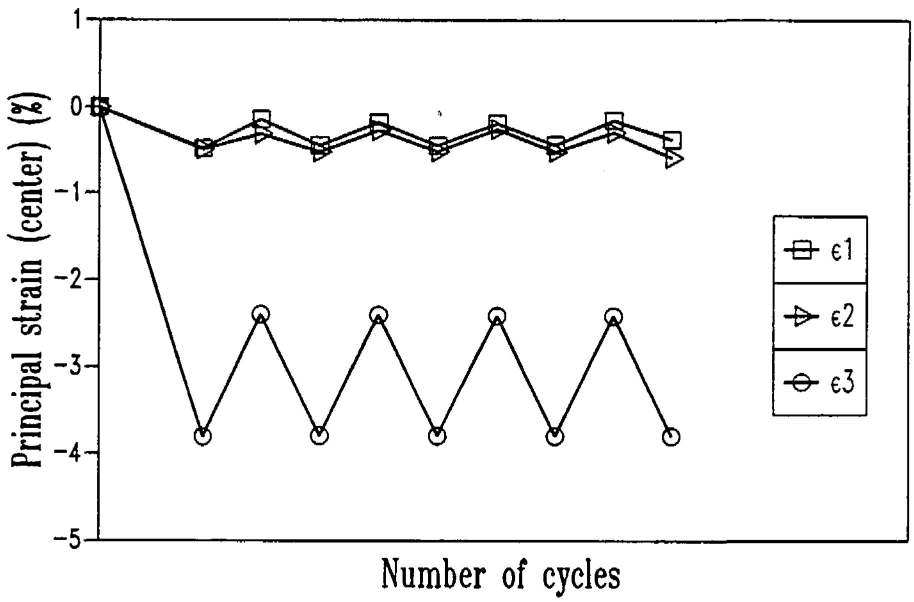

Fig. 4.15. Behavior of the principal strain under the uniform thermal cycling. (braze center)

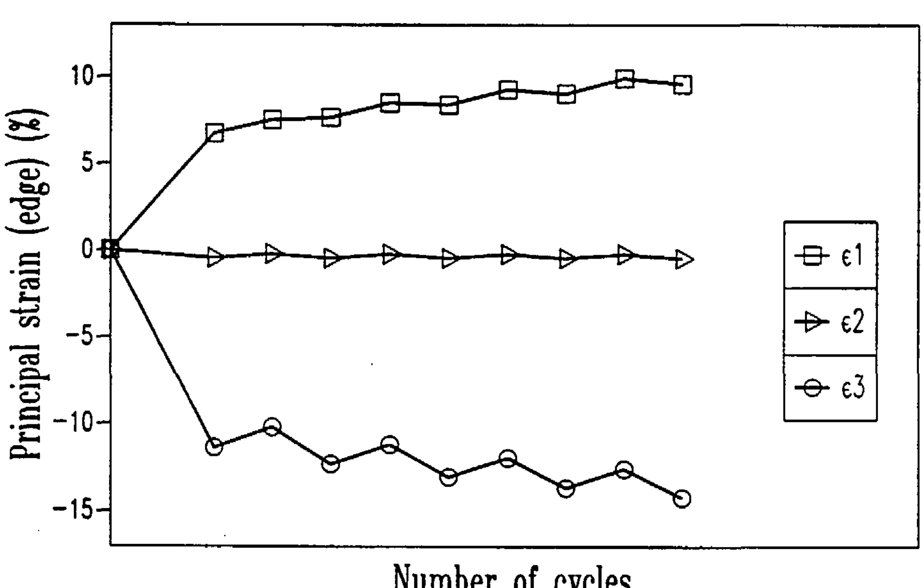

Fig. 4.16. Behavior of the principal strain under the uniform thermal cycling. (braze edge)

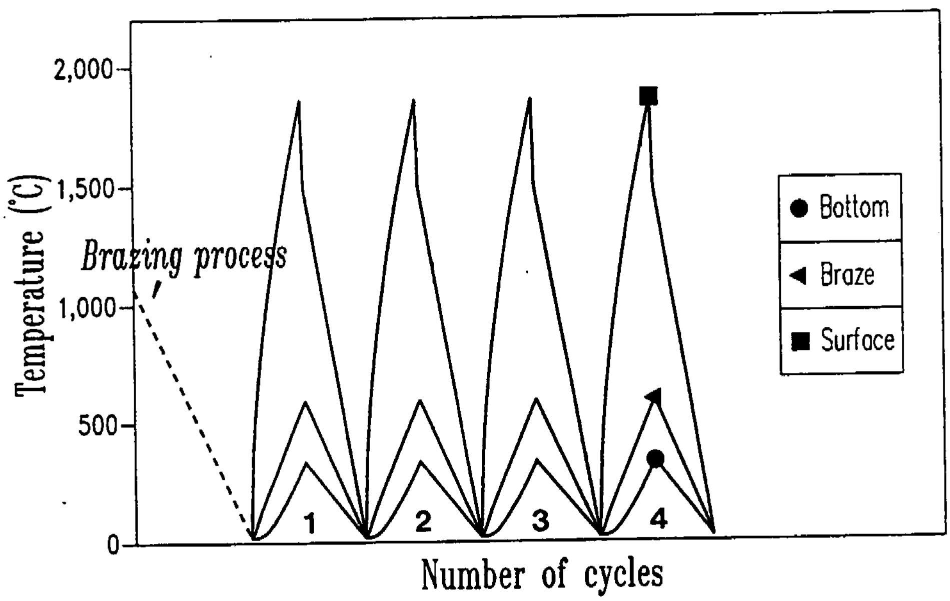

Fig. 4.17. Thermal load history applied for the thermal fatigue analysis. (Transient HHF cycling. Energy density: 20 MW/m^2, Pulse duration: 2.1 s)

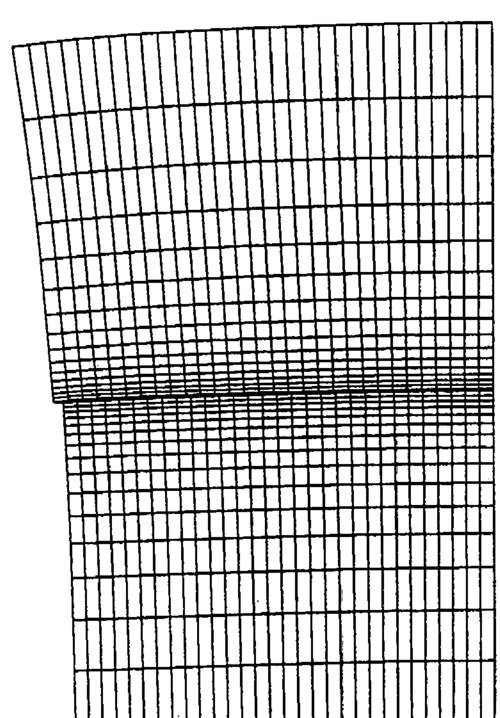

Fig. 4.18. Deformed structure of the model at the moment of peak temperature.

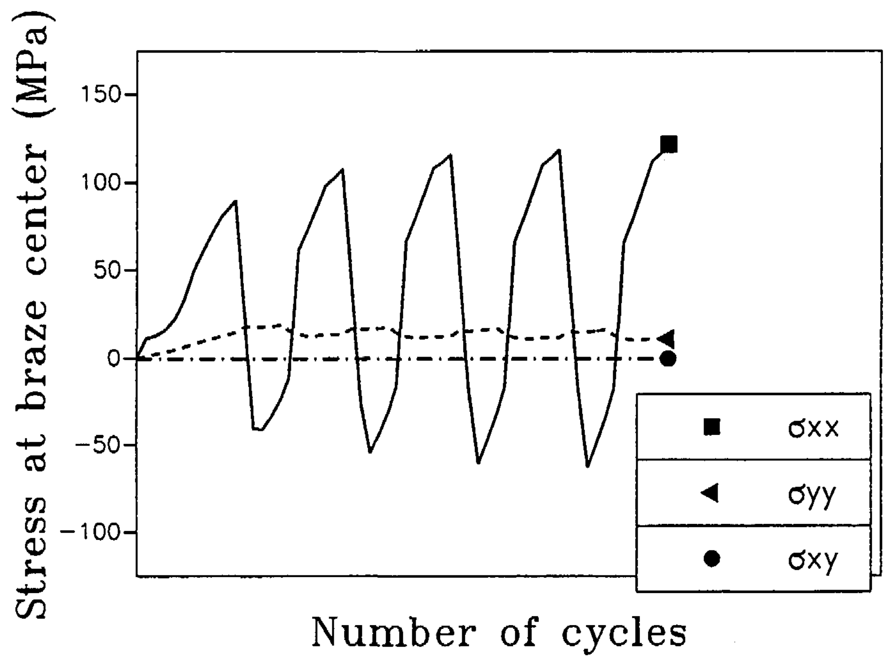

Fig. 4.19. Behavior of the stress components under the HHF thermal cycling. (braze center)

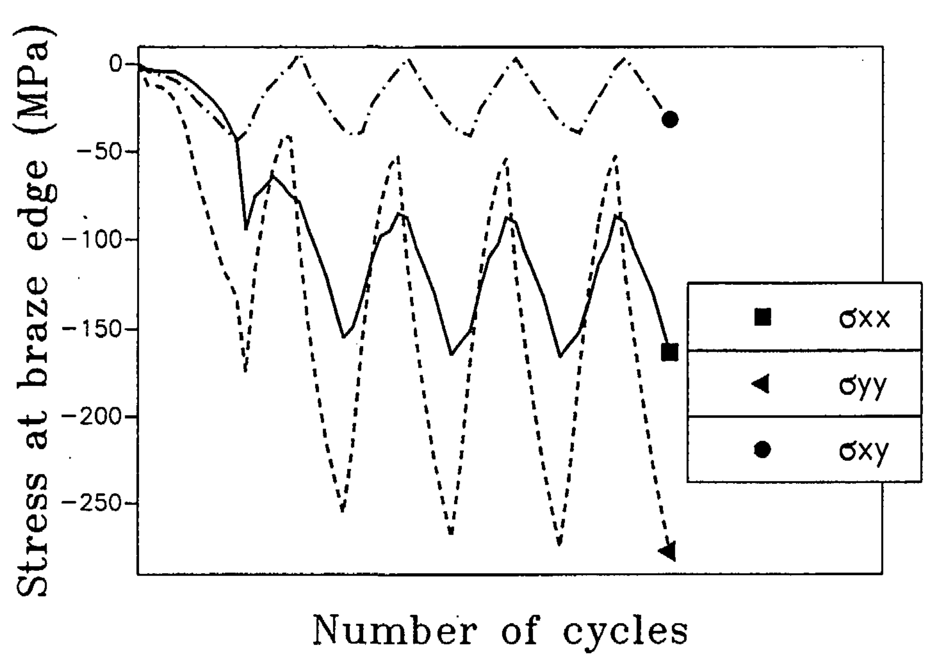

Fig. 4.20. Behavior of the stress components under the HHF thermal cycling. (braze edge)

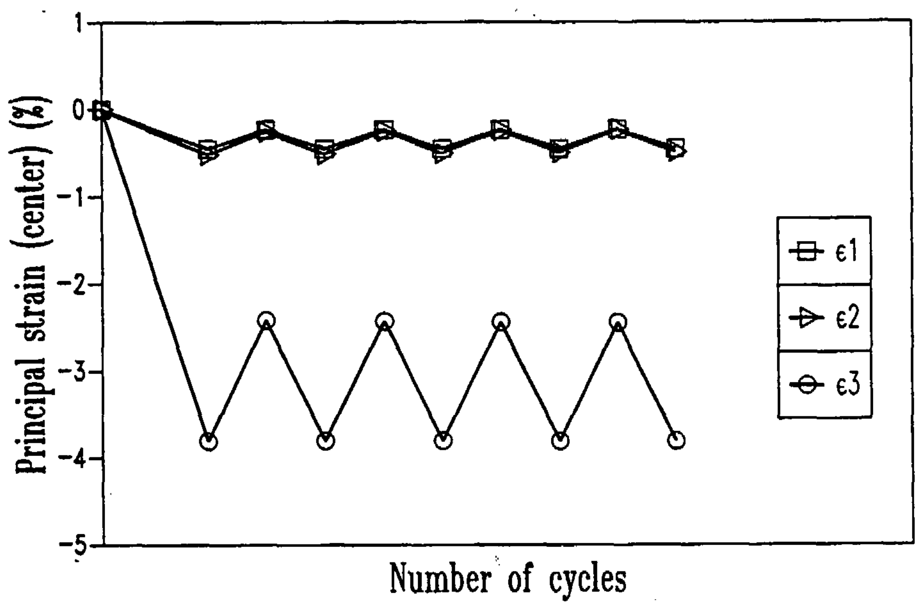

Fig. 4.21. Behavior of the principal strain under the HHF thermal cycling. (braze center)

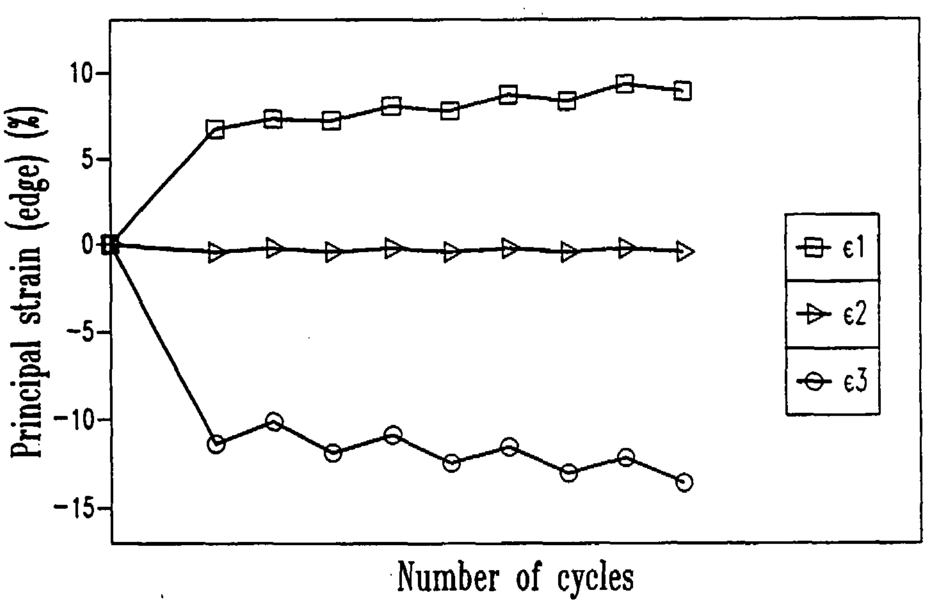

Fig. 4.22. Behavior of the principal strain under the HHF thermal cycling. (braze edge)

The maximum temperature of the braze layer during the HHF cycling is 597 °C, which is nearly the same as in the uniform thermal cycling in Fig.4.11. At the moments when peak temperatures occur, severe temperature gradient develops in vertical direction. The deformed structure at these points is shown in Fig.4.18.

Fig.4.19 shows the change of three stress components at the braze center during the thermal cycling. The time variation of the stresses shows a similar behavior as in Fig.4.12. The normal stress component has a nearly constant value.

Fig.4.20 shows the change of stress components at the free surface edge of the braze. Some differences in the stress change between Fig.4.13 and Fig.4.20 are noticed. In Fig.4.20, the axial-, and the normal component show a pure repeated mode. The whole range of these stress components locates in fully compressive region. The amplitude of the normal component is considerably increased.

In Fig.4.21 and Fig.4.22, the time history of the principal strain components at the braze center and at the free surface edge of the braze are shown, respectively.
The change of the principal strains is not different from that of Fig.4.15 and Fig.4.16.

5.4. Life time estimation

Applying the data for the cyclic change of the principal strains to eq.(4.24), the equivalent strain range can be determined. To calculate the equivalent strain ranges, the initial point of the fourth load cycle was taken for the reference time. With the aid of eq.(4.22) and the strain amplitude values obtained from eq.(4.24), fatigue life can be estimated.
The predicted fatigue life is listed in table 4.2. These results are determined based on the reference temperature of 600 °C for which the values of R_m, E and Z are given in eq.(4.23).

Table 4.2
Predicted fatigue life of braze layer for two loading conditions

	center	edge
$\Delta\varepsilon_{eq}$ (%)*	0.7537	0.9921
$\Delta\varepsilon_{eq}$ (%)**	0.7642	0.8037
Fatigue life* (cycles)	269	243
Fatigue life** (cycles)	290	370

* : uniform thermal cyclings, ** : HHF cyclings

Both thermal loading conditions considered above yield similar lifetime for the bulk region of the braze. The braze edge under the HHF cycling shows longer lifetime than for the braze center in spite of its larger equivalent strain amplitude. This may be due to the effect of mean stress term in eq.(4.23).

5.5. Influence of thermal gradient on the interfacial stresses

The cyclic plastic deformation of the braze can affect the bulk stresses in the CFC and TZM body. In Fig.4.23, the axial component of the interfacial stresses at the symmetry center is plotted for two cases of thermal loadings, i.e. for the transient HHF load in Fig.4.17 and for the uniform heating in Fig.4.11.
The peak stress at the Cu/TZM interface decreases monotonically during the cycling. The peak stress at the CFC/Cu interface is also relaxed slightly. The stress amplitude for both interfaces remains unchanged. This cyclic relaxation of the bulk stresses seems to be related to the cumulative strain hardening of the braze layer. The CFC/Cu interface experiences a identical cyclic stress variation for both loading conditions. The TZM/Cu interface undergoes larger stress amplitudes in case of the HHF cycling.

The spatial distributions of the three interfacial stress components on the CFC side are plotted in Fig.4.24.
It is seen that the axial component σ_{xx} and the shear component σ_{xy} show minute difference in their distribution between the two thermal loading conditions. The normal component σ_{yy}, however, shows a considerable deviation between the two thermal loading conditions.
The normal stress induced by the HHF load exerts more traction onto the whole interface than by the uniform thermal load. The intensification of the normal stress under the HHF load is related to the forced bending of the joint caused by the thermal gradient.
The tensile normal stress in the bulk region can enhance the fatigue crack extension under application of cyclic thermal loads.

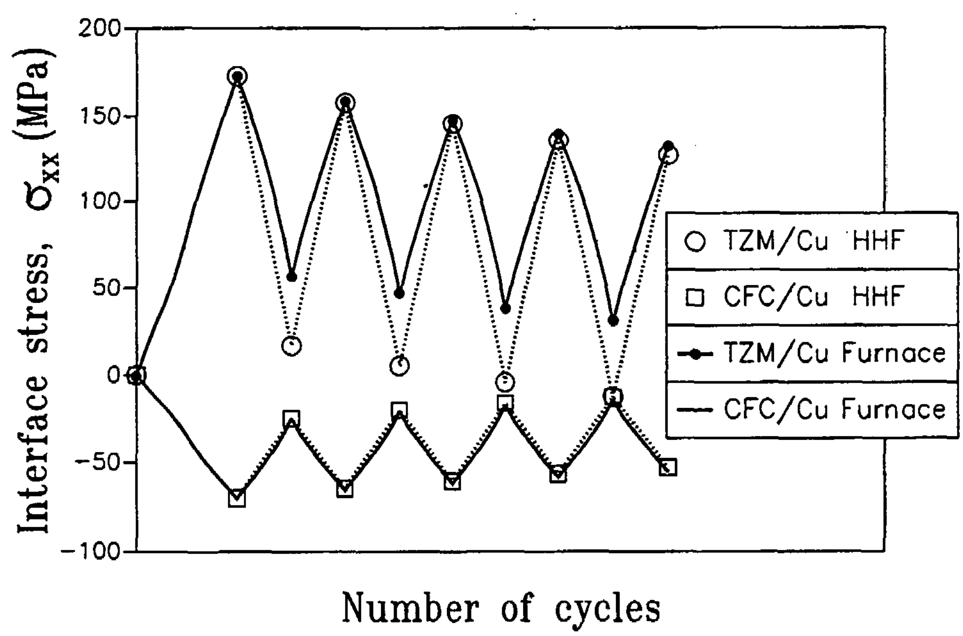

Fig. 4.23. Cyclic evolution of the interfacial stresses under the thermal cycling. (interface center of the CFC side)

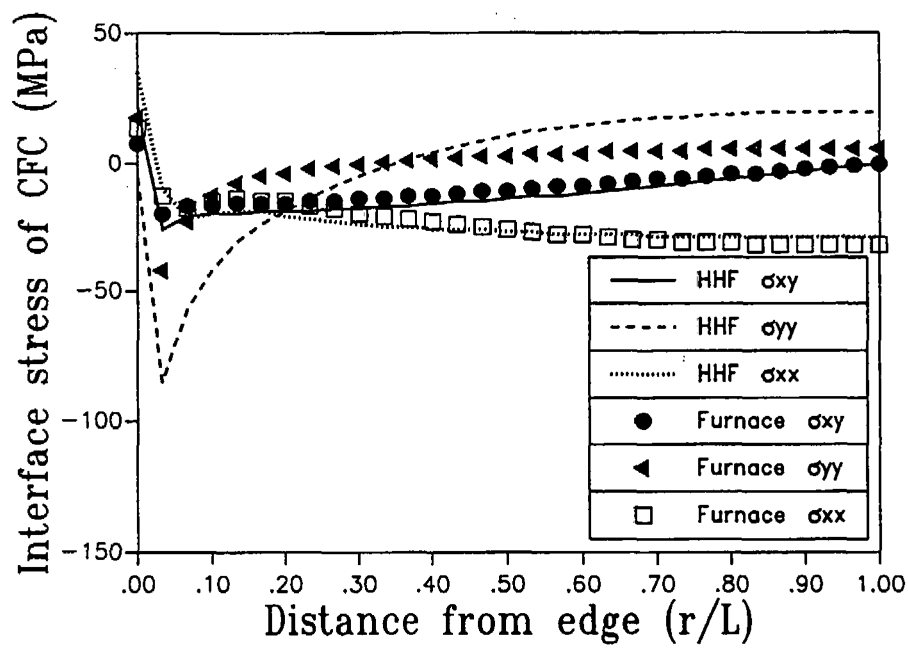

Fig. 4.24. Distribution of the interfacial stresses on the CFC side at the end of the heat pulse.
(The stress components for CFC/Cu/TZM system are plotted with symbol markers whereas the lines represent the stresses calculated considering no braze layer.)

5.6. Microstructures

Microstructures of the copper braze layer after cyclic thermal loads are shown in Fig.4.25. Each line in the micrographs represents the surface step of a dislocation glide plane.

The surface offset of the deformed braze in the center region is shown in Fig.4.25 (a). The structure in this micrograph was obtained under cyclic HHF load with low thermal deposition (Test 1).
It is seen that the flow mechanism is duplex slip where the both primary-, and conjugate slip systems, which are crystallographically equivalent, are operative requiring a lowest activation energy than other slip systems. The well defined slip lines of dislocation glide, that are revealed by parallel straight traces, suggest that the plastic flow under this loading condition would be driven by easy glide.
This is a result of planar glide [13,14]. The planar glide is a dominant deformation pattern when the material has a low stacking fault energy. In this case, dislocations tend to remain separated in partial dislocations. The movement of the two partial dislocations is restricted by the plane of stacking fault. Then, the slip offsets on the surface become straight.
The array of the slip lines in Fig.4.25 (a) can be explained by considering the principal stress orientation. The slip lines in the micrograph represent the surface cut of the shearing planes on which the maximum resolved shear stress acts. Since the plane of the maximum shear stress is rotated from the axis of the principal stress by $\pi/4$ (rad.), the slip offset will cross the principal stress axis with the angle of $\pi/4$ (rad.).

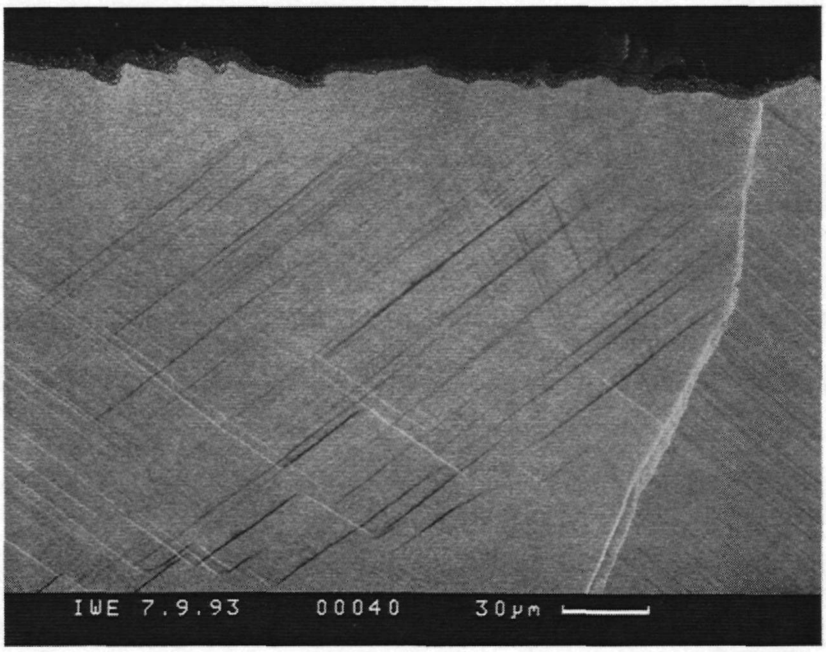

Fig. 4.25 (a) Test 1 (center region)

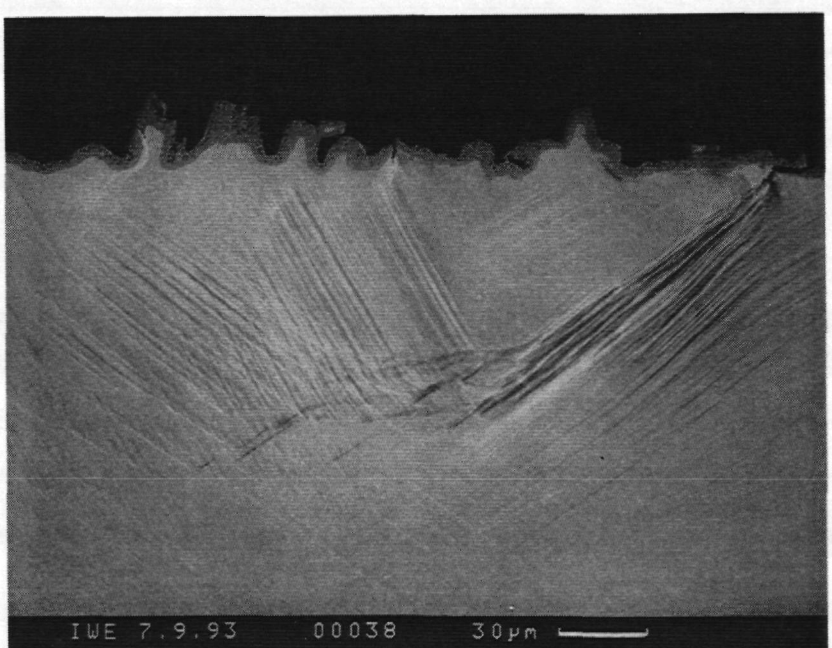

Fig. 4.25 (b) Test 1 (intermediate region)

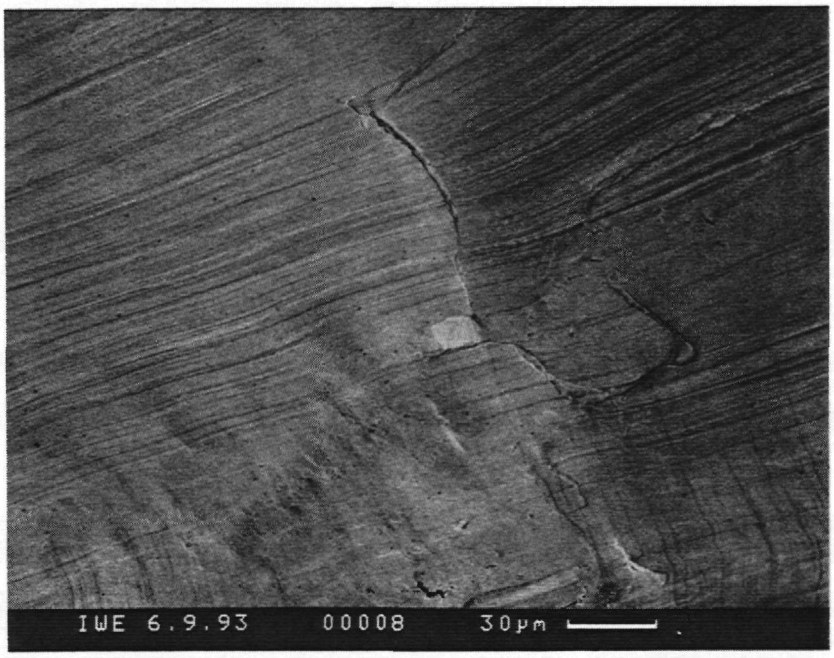

Fig. 4.25 (c) Test 3 (intermediate region)

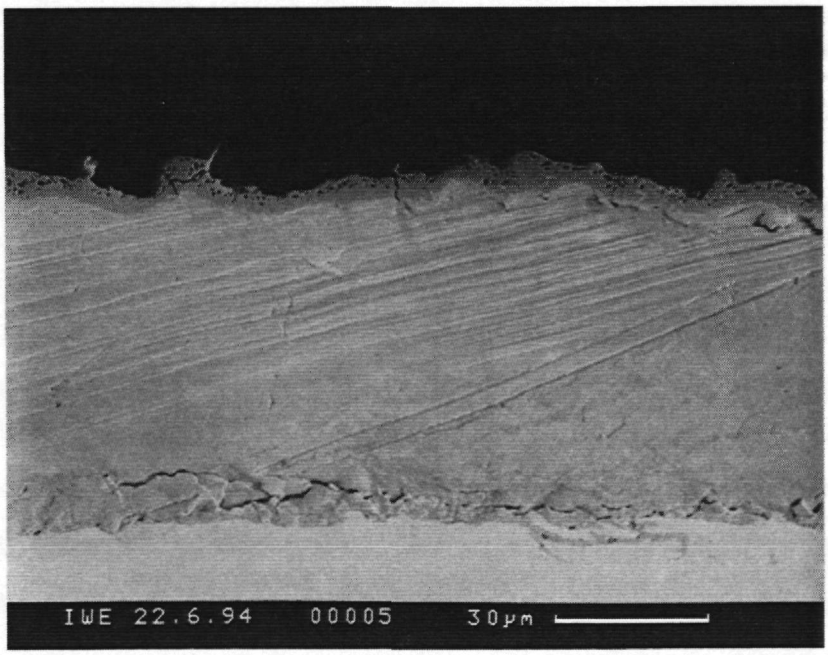

Fig. 4.25 (d) Thermal cycling in a furnace with temperature amplitude of 580 °C.
(20 °C ⇔ 600 °C)

Fig. 4.25. SEM micrographs for the deformed structures of the copper braze.

Fig.4.26 (a) shows the principal stress distribution in the center region of the braze layer. In this plot, only the compressive component is presented to avoid a complicated display. The direction of the maximum principal stress is parallel to the bond interface. This indicates that the slip pattern in Fig.4.25 (a) agrees with the result of the numerical analysis.

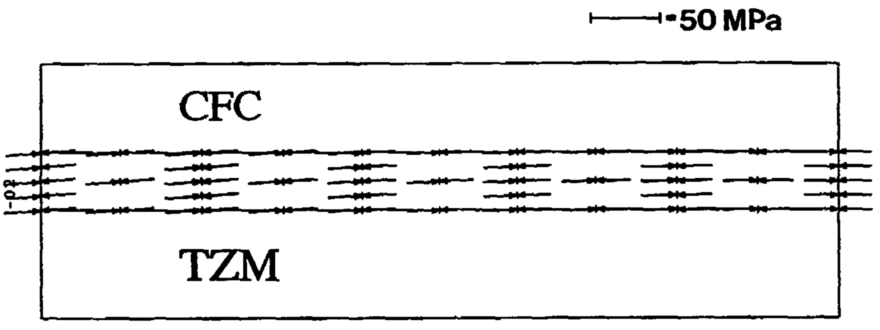

(a) center region

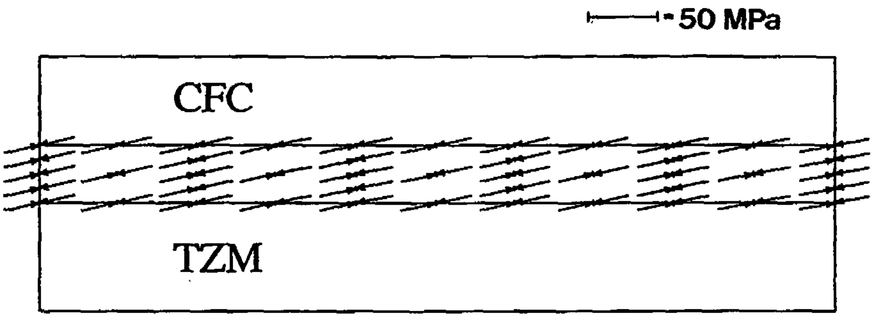

(b) intermediate region

Fig. 4.26. Distribution of the principal stress in the braze layer.
(at the moment of peak temperature in the HHF thermal cycling.)

The surface offset of the deformed braze in the intermediate region is shown in Fig.4.25 (b). In Fig.4.25 (b), a set of slip lines, which are superposed on the primary slip lines, represent a dislocation glide by the secondary slip system.

Fig.4.26 (b) shows the principal stress distribution in the intermediate region of the braze layer. The direction of the maximum principal stress is rotated from the bond interface line. This rotation of the maximum principal stress may induce the activation of a secondary slip system where the resolved shear stress exceeds its critical value for slip.

Fig.4.25 (b) suggests that stress concentration induced by a interfacial crack can be relieved by the plastic dissipation through the ductile braze. The intensified stress field near the crack tip generates a local slip band in the braze in which the slip line density is particularly high. The slip offsets in this enhanced deformation band take on a wavy pattern.
The wavy glide shown in the micrograph is due to the cross slip of the dislocations [13]. By the application of a suitably large stress, which is achieved by the stress concentration near the crack tip in this case, it is possible to squeeze the partial dislocations together against a barrier to form a whole dislocation. If this recombined dislocation has a screw component, it may cross slip.

Under the severe cyclic thermal load producing a peak interface temperature of 900 °C (Test 3), the density of the slip lines increases considerably (Fig.4.25 (c)). Due to the large strain amplitude, much more plastic strain is accumulated.
As the dislocations are multiplicated during the flow, sessile dislocations are frequently generated from dislocation reactions. These products can be a formidable barrier to slip and the dislocations are forced to cross slip [13]. As a result, the fully wavy slip pattern is formed with the aid of thermal activation.

In Fig.4.25 (d), fatigue damage in the copper braze produced by the slow thermal cycling in a vacuum furnace is shown. It should be noticed that the damage occurs near the interface to TZM. In the case of HHF cycling, however, such a damage was not observed.

6. Conclusions

When a brazed joint component is subjected to thermal loads, the mismatch of the thermal expansion generates thermal stress that can exceed the yield point of ductile filler metal.
In this work, flow behavior of the Cu braze layer in a CFC/Cu/TZM joint system was analyzed. To calculate the plastic deformation of the braze interlayer, finite element analysis was performed using a two dimensional model.

The simulation of the brazing process was carried out prior to the thermal cycling steps.
In the cool down phase of the brazing process, the predominant development of the residual stress occurs below 600 °C. The free surface edge and the center of the interlayer show similar stress evolution which differs just in their magnitude.

For a assessment of fatigue behavior, cyclic thermal loadings are simulated for both cases of homogeneous and transient temperature changes.
The stress amplitudes reach the saturation in first four cycles approximately. At braze center, the axial stress component is the predominant component. The axial component shows a reversed fatigue mode with reversing signs. The feature of the stress change is nearly identical in both loading conditions. At braze edge, the major contribution stems from the normal stress component. In this region, the thermal gradient influences on the variation mode and amplitude of the stresses.
Both cyclic thermal loading conditions produce similar cyclic behaviours of stress and strain in the braze layer.

Applying the multiaxial fatigue theory based on the ASME code, the fatigue life of the interlayer is estimated for the two thermal loading conditions.
The thermal gradient generated by the HHF loading has no significant influence on the lifetime as long as the interface temperature is kept unchanged.

HHF cycling tests were conducted on the brazed element consisting of CFC/Cu/TZM joint. From the slip line offset on the surface, the mechanisms of the plastic deformation for various temperature amplitudes can be assessed.
For the temperature amplitude of 580 °C, the copper braze deforms by the planar slip. As the temperature amplitude increases, the high strain amplitude results in the enhanced cross slip causing wavy slip. The stress concentration near the interfacial crack tip is relieved due to the plastic dissipation in the ductile braze.

7. Reference

[1] R. Hill, "The Mathematical Theory of Plasticity", Oxford University Press, London, 1950

[2] S.P. Timoshenko, J.N. Goodier, "Theory of Elasticity" 3rd ed., Mcgraw-Hill Inc., New York, 1970

[3] G.S. Taylor, H. Quinney, Phil. Trans. Roy. Soc. London, Ser. A 230 (1931), pp. 323-362

[4] R. von Mises, "Mechanik der festen Körper im plastisch-deformablen Zustand", Nachrichten der Gesellschaft der Wissenschaften Göttingen, Mathematisch-Physisch Klasse, Göttingen, (1913)

[5] D.C. Drucker, Trans. ASME. J. Appl. Mech., (1959), pp. 101-106

[6] P.O. Charreyron, D.O. Patten, B.J. Miller , Ceram. Eng. Sci. Proc. 10 (11-12) (1989), pp. 1801-1824

[7] J.D. Morrow, Internal Friction, Damping and Cyclic Plasticity, ASTM STP 378, pp. 45, (1965)

[8] M. Seki, T. Horie, T. Tone, K. Nagata, K. Kitamura, Y. Shibutani, M. Shibui, T. Araki, Proc. ICFRM-3 (Karlsruhe, FRG, 1987), J. Nucl. Mater., 155-157 (1988), Part A, pp.392-397

[9] ASME, Boiler and Pressure Vessel Code, Section III, Div. 1, United Energy Center, ASME, New York (1979)

[10] E. Diegele, D. Munz, G. Schweinfurther, "Lifetime Prediction for the First Wall of a Fusion Machine", KfK-Bericht, KfK 5283, Kernforschungszentrum Karlsruhe GmbH, Karlsruhe

[11] "ABAQUS Theory Manual 5.4", Hibbit, Karlson and Sorenson Inc., Providence, RI, USA. (1994)

[12] I. Smid, M. Akiba, M. Araki, S. Suzuki, K. Satoh, "Material and Design Considerations for the Carbon Armored ITER Divertor", JAERI Report, JAERI-M 93-149, Japan Atomic Energy Research Institute (1993)

[13] R.W.K. Honeycombe, "The Plastic Deformation of Metals" 2nd ed., Edward Arnold, London, 1984

[14] A. Seeger (Ed.), "Moderne Probleme der Metallphysik" Band 1, Springer Verlag, Berlin, 1965

Chapter 5. Thermomechanical behavior of actively cooled, brazed divertor components under cyclic high heat flux loads

1. Introduction

In this chapter, thermomechanical performance of divertor components with various material combinations is investigated. Actively cooled divertor mock-ups consisting of different low-Z armor tiles brazed to TZM heat sinks are tested in an electron beam test facility. Five different armor materials are tested.
Thermal response under screening and thermal fatigue tests are estimated.
Microstructural damage under HHF cycling tests is characterized to elucidate the degradation of the joints.

Thermal stress fields are calculated employing the finite element method. The analysis is performed for one thermal load cycle of the simulated HHF test condition.
The time history of the thermal stresses for some critical locations in the module cross section is given and the nature of their cyclic behavior is discussed.
The results of the analysis for five different material combinations are presented.

2. Experiment

2.1. Mock-up description

A set of actively cooled divertor modules with different armor materials was manufactured for the tests. A typical module is shown in Fig.5.1.

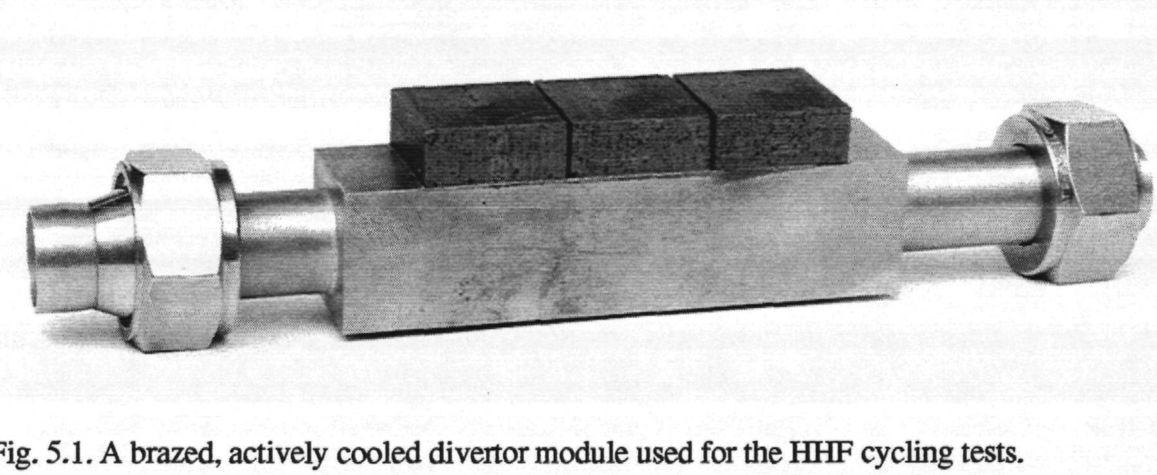

Fig. 5.1. A brazed, actively cooled divertor module used for the HHF cycling tests.

The test mock-up consists of three or four square armor tiles brazed to a metallic heat sink block. Following materials were used.

- armor tiles: Sepcarb N112 (2D CFC), PCC 2S (2D CFC), MFC 1 (1D CFC), RG-Ti (7.5 % Ti doped recrystallized graphite), and SiC 30 (60 % SiC-35 % graphite-5 % Si)
- heat sink block: TZM (Mo-0.5 % Ti-0.1 % Zr)
- coolant tube connectors: ferritic stainless steel

The size of the individual tile is $25 \times 25 \times 10\,(\mathrm{mm}^3)$. The heat sink block has a geometry of $25 \times 25\,(\mathrm{mm}^2)$ in cross section and 100 (mm) in length. The coolant tubes (18 mm in outer diameter, 16 mm in inner diameter) are inserted in both end sides.

A Cu1Cr braze was used to bond the armor tiles to the TZM heat sink whereas the coolant tube was joined to the TZM body with a Au18Ni braze. The thickness of the braze layer was about 150 μm. The orientation of good thermal conductivity in the tiles is parallel to the direction of incident heat flux.

2.2. Test facility

In order to investigate the thermal performance of the divertor mock-ups under HHF loads, the electron beam test facility at Research Centre Jülich was used. The operational parameters of the facility are listed in table 5.1.

Table 5.1
Parameters of test facility JUDITH

Total power	≤ 60 kW
Power density	≤ 15 GW/m^2
Beam current	≤ 400 mA
Particle energy	≤ 150 keV
Used electric voltage	120 kV
Scanning Frequency	≤ 100 kHz
Maximum area to be scanned	$10 \times 10\,(\mathrm{cm}^2)$
Coolant flow rate	1.15 *l*/s

By means of high frequency beam rastering, the surface of the specimens can be irradiated homogeneously with the well defined loading area.
The equipments of the applied diagnostic system are as follows.

- a two-coloured pyrometer (1000 - 3500 °C)
- an optical pyrometer (200 - 1100 °C)
- IR scanner
- CCD camera
- thermocouples
- coolant water calorimetry

The local surface temperature of the tiles was measured by pyrometers and the whole temperature distribution on the surface was measured by IR camera. The temperature of the braze layer and the coolant water was detected by thermocouples.

2.3. Pre-inspection of the mock-up joints

Before the main tests were carried out, the whole divertor mock-ups were subjected to low heat flux to inspect the quality of the bond interface. By use of IR thermography, the temperature distribution on the whole surface was displayed in color shading.
Brazing defects, where the thermal contact is poor, can be detected in form of hot spots due to the local elevation of the temperature. The protection tiles with an intact bond interface were selected and used for further testing.

2.4. Screening test

To estimate the limit of tolerable thermal loads, screening tests were performed.
The incident power levels were increased stepwise from shot to shot. The pulse duration was 30 seconds. The absorbed net power density deposited on the tiles is lower than the nominal power density due to the reflection of electrons. Since the heat flux to be removed by the coolant during steady state conditions is balanced with the heat flux to be deposited on the tile surface, the net energy flux can be calibrated by measuring the heat removed.
The power density was increased until considerable thermal erosion occured or the joint failed due to thermal shock. The tests were terminated to avoid extensive sublimation of carbon although the braze joints presumably could have survived higher power levels.

2.5. Thermal cycling test

To assess the fatigue behavior of the mock-ups under pulsed thermal loads, thermal cycling tests were conducted. The experimental parameters are summarized in table 5.2.

Table 5.2
Test conditions for the thermal cycling tests.

Armor material	Absorbed power density (MW/m^2)	Number of cycles
Sepcarb N112	13.5	50
	12	30
	10.5	50
PCC 2S	10.5	30
MFC 1	7	30
RG-Ti	10.5	*
SiC 30	7	*

(* : The module joints were debonded during 2nd shot.)

The duration of electron beam irradiation for all shots was kept constant as 30 seconds. The period of each thermal pulse including the cooling phase was about one minute. Within a pulse, steady state was achieved both for the heating-, and the cooling phase.
The maximum surface temperature of the tiles in steady state conditions and its change during the cyclic loading were measured. The propagation of interfacial defects was traced by the IR thermography for each beam shot.

3. Calculation

3.1. Model

The thermal-, and elastoplastic stress analysis were performed for the divertor modules in HHF tests using the finite element code ABAQUS [1]. Only half of the geometry was modeled due to symmetry. The two-dimensional finite element mesh includes 296 8-noded quadrilateral elements and 1059 node points. For stress analysis, generalized plane strain elements were used to consider the out-of-plane strain. The thin, ductile braze layer was neglected in the model.
The material combinations selected for the analysis are identical to those of the divertor modules tested for the HHF simulation. The anisotropy and the temperature dependence of the material properties were taken into account.
The time dependent effects were not included. It was assumed that the all five armor materials behave elastically. The applied plasticity of the metals was based on stepwise linear stress-strain relations and the isotropic hardening law.

3.2. Thermal analysis

Thermal analysis precedes the stress analysis to produce the input temperature data for the following stress calculations.
The surface of the armor tiles was subjected to uniform heat flux of 10.5 MW/m^2 for 30 seconds. The coolant water temperature was 20 °C and the flow velocity was 6 m/s. The coolant heat transfer coefficient was computed as a function of the cooling tube wall temperature assuming two phase heat transfer. Cooling by the radiative emission was considered. A cooldown phase of 20 seconds followed the thermal load pulse.

3.3. Stress analysis

The brazing process was simulated prior to the HHF loading step to consider the residual stresses at room temperature. The stress free reference temperature was taken as 1070 °C which was the freezing point of the braze metal. This residual stress is superposed to the subsequent stress fields caused by HHF thermal loads. The stress evolution corresponding to the one load cycle of 50 seconds was calculated.
The internal pressure of the coolant tube was neglected to see the pure thermally induced stress state.

4. Results and discussion

4.1. High heat flux cycling tests

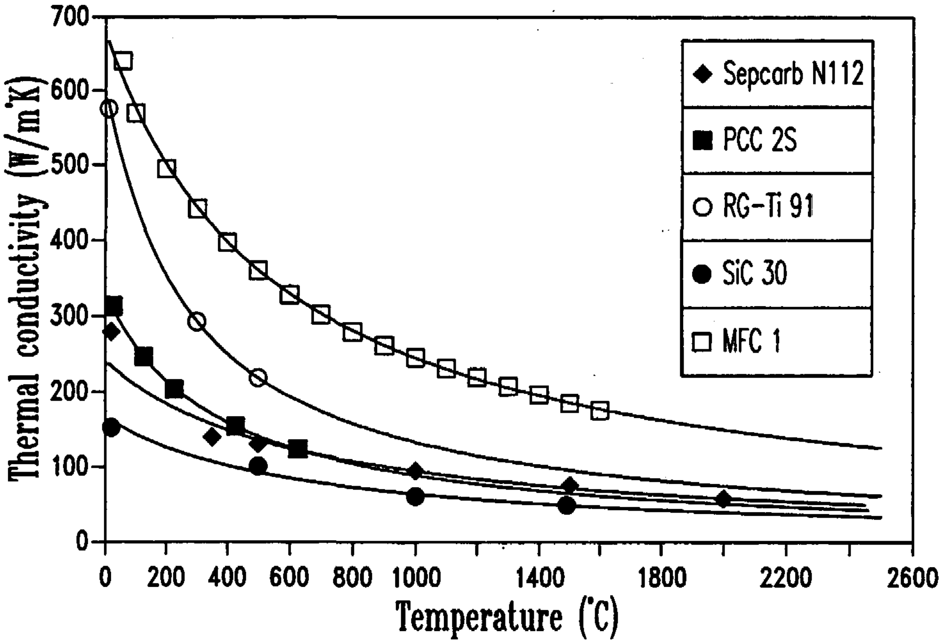

Fig. 5.2. Thermal conductivity of the divertor materials.

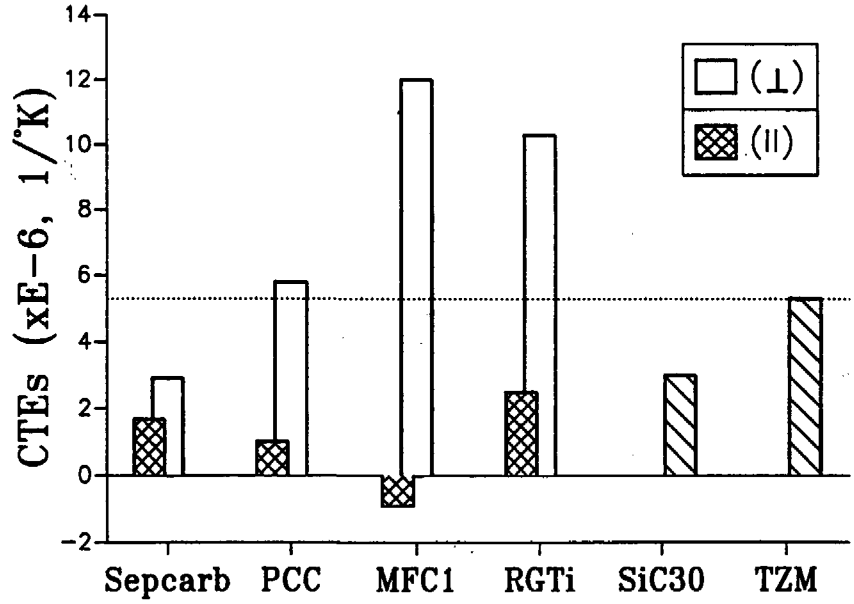

Fig. 5.3. Thermal expansion coefficient of the divertor materials.

In Fig.5.2-5.3, thermophysical properties of materials used for the divertor mock-ups are presented [14-20].

Fig.5.4 shows the thermal response of a divertor mock-up (Sepcarb N112/TZM joint) under thermal power density of 10.5 MW/m^2 with pulse duration of 2 seconds.
The temperature evolution of the armor surface measured by the pyrometer is compared to the numerical result obtained from the finite element analysis. An electric power density of 13 MW/m^2 was needed to generate the net thermal power density of 10.5 MW/m^2 on the divertor armor surfaces. The acceleration time to reach full test power and the time to zero power was one second, respectively.
The steady state condition was achieved after 20 seconds by equilibrium between the input heat flux and the heat removed via coolant. The results show a good agreement in the steady state. In the transient phase, there exists somewhat difference, which indicates that the actual thermal conductivity of the armor material used would be higher than the data used for the numerical analysis. It is seen that the surface region experiences a temperature change of over two thousands degree Celsius in a minute.

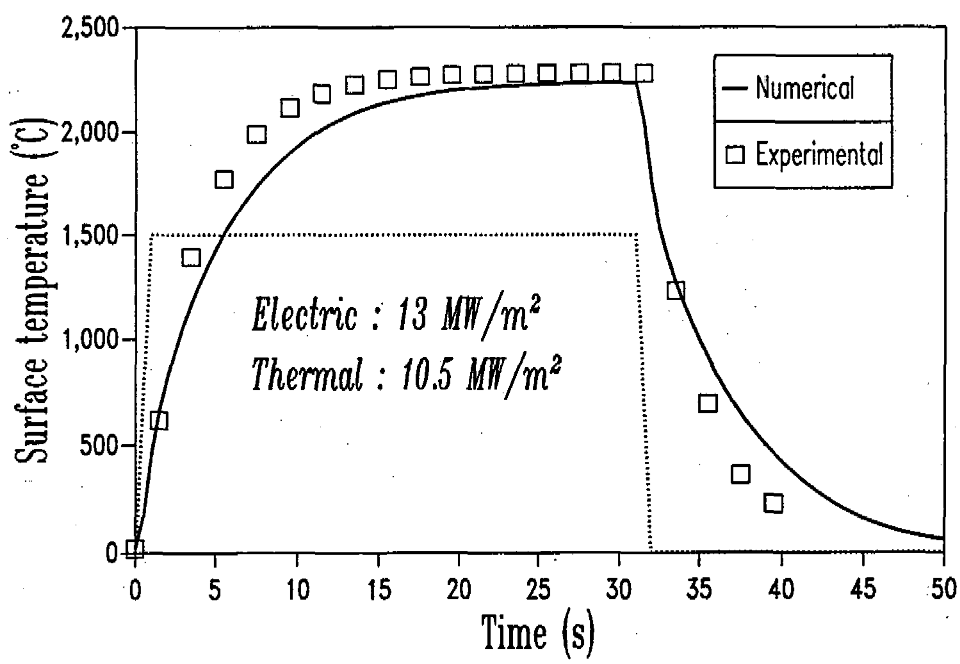

Fig. 5.4. Thermal response of the divertor mock-up.
(Sepcarb N112/TZM joint. power density: 10.5 MW/m^2, pulse duration: 30 s).

The steady state surface temperatures of the five divertor mock-ups under HHF simulation condition are given in Fig.5.5.
The experimentally measured values as well as the numerically calculated results are presented. The SiC30/TZM mock-up was tested for a lower power density of 7 MW/m^2 because it could not survive under higher power density.

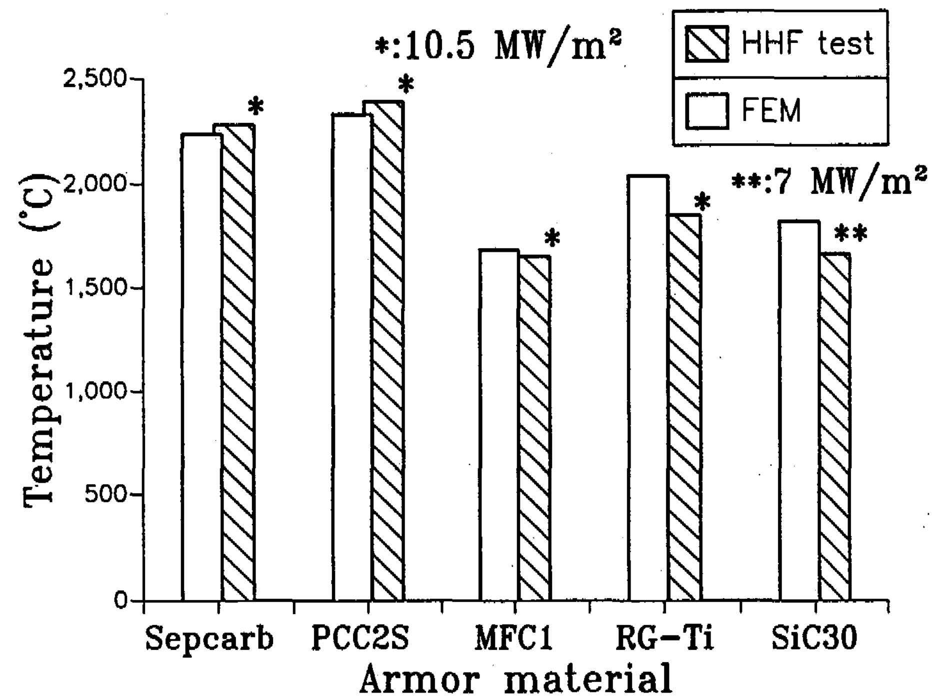

Fig. 5.5. Surface temperature of the divertor mock-ups in the steady state of the HHF loading.
(power density: 10.5 MW/m^2 or 7 MW/m^2, pulse duration: 30 s).

The thermal performance of the mock-ups measured in the screening tests is shown in Fig.5.6. Within the range of applied heat flux which varies from 7.2 MW/m^2 to 12 MW/m^2, the temperature shows a linear proportionality to the power density.
The sequence of the surface temperature values shows a reciprocal relationship with the thermal conductivities in Fig.5.2.
This is clear to understand since the surface temperature depends directly on the ability to transfer the deposited heat to the metallic cooling body. When the thermal conductivity of the metallic body is much lower than that of the armor material, as is the case for TZM, the thermal flow will be retarded at the interface.
In this case, the armor tile with high thermal conductivity undergoes a thermal equilibration where the interface temperature is increased. This effect is demonstrated in Fig.5.6(b) where the interface temperature value increases with increasing thermal conductivity.
The braze interlayer in the mock-up with the MFC1 armor was melted during the shot of 10.5 MW/m^2. Under the power density in which the surface temperature of the armor tiles exceeds approximately 2500 °C, thermal erosion becomes essential.

Fig.5.7 shows the fatigue behavior of the mock-ups under cyclic HHF loads. The individual points in the plot represent the temperature of the tile surface and of the braze interface during the steady state condition in each thermal cycle. The mock-ups with the SiC30 and MFC1 armors were tested under reduced power density (7 MW/m^2) due to the results from the screening tests.

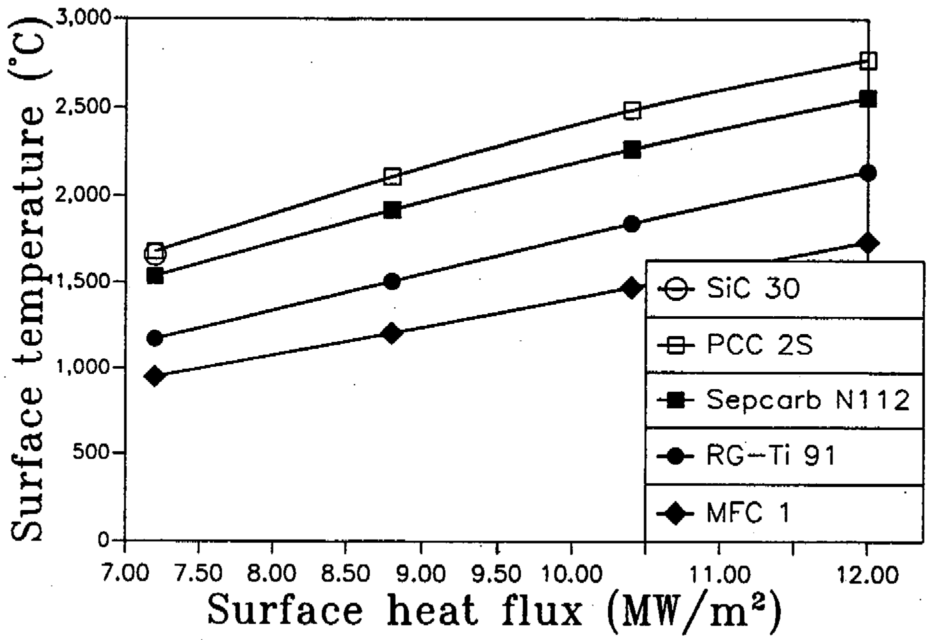

Fig. 5.6 (a) Surface temperature

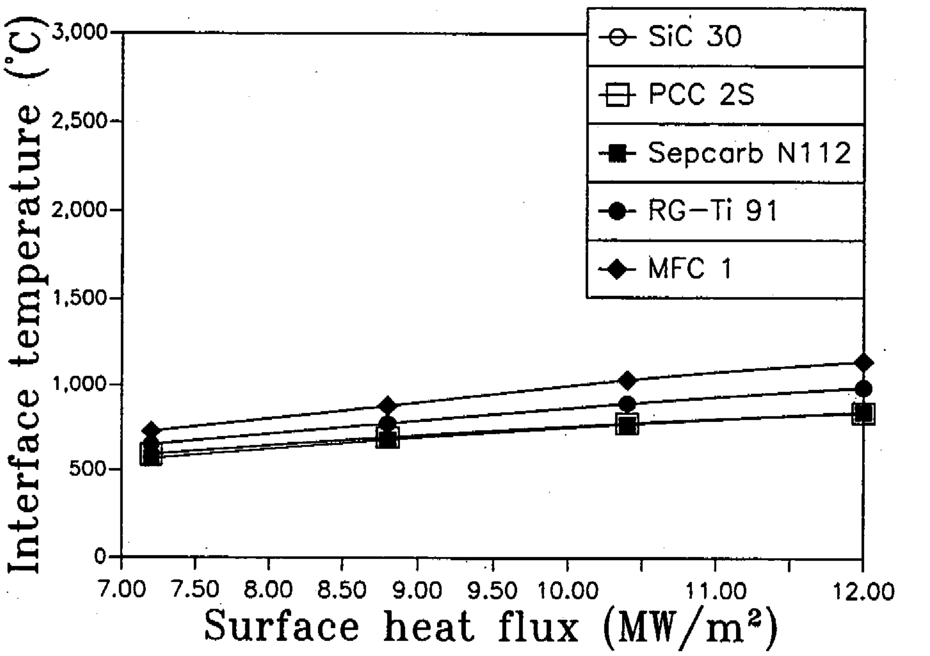

Fig. 5.6 (b) Bond interface temperature

Fig. 5.6. Thermal performance of the divertor mock-ups for various levels of power density. (The temperature was measured in the steady state)

The mock-ups with the SiC30 and RG-Ti armors could survive only the first shot. The interface of theses mock-ups was debonded during the second shot showing abrupt fracture. The mock-ups armored with CFC materials showed good fatigue resistance. The monotonic increase of the surface- and interface temperatures during the HHF cycling is related to the accumulation of microscopic failures in the interface region.
The increment of these temperatures is small and slightly decreasing, which indicates that the density of the interfacial damage is low and their growth is stable.

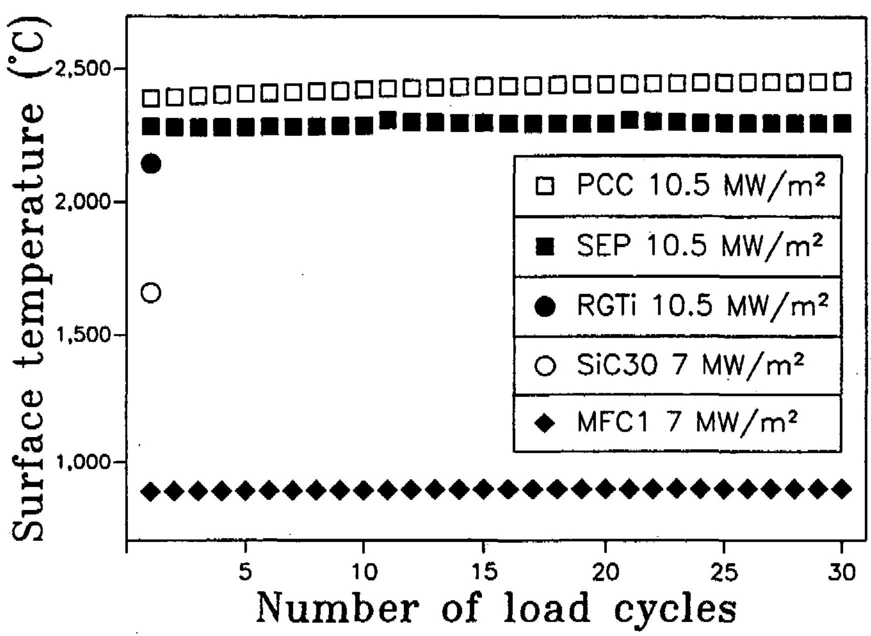

Fig. 5.7. Fatigue behavior of the divertor mock-ups under cyclic HHF loads.

The fatigue behavior of the mock-ups with the Sepcarb N112 armor under three different power densities is shown in Fig.5.8. For the thermal load of 12 MW/m^2, the test was carried out only to 30 cycles since the temperature increase became stable and nearly saturated.
The mock-up cycled with 13.5 MW/m^2 shows a abnormal temperature evolution. After the test, the tile surface of this mock-up was damaged considerably due to thermal erosion. The decrease of the surface temperature is supposed to be related to the massive thermal erosion of the CFC tile.

Fig.5.9 shows the cross sections of the tested divertor mock-ups. The divertor elements were cut by water jet technique.
All mock-up cross sections consisting of CFC/TZM joint do not show any macroscopically observable fatigue damage (Fig.5.9(a)).
On the contrary, the interface of the mock-ups armored with ceramic and graphite tiles was debonded by brittle fracture (Fig.5.9(b)).

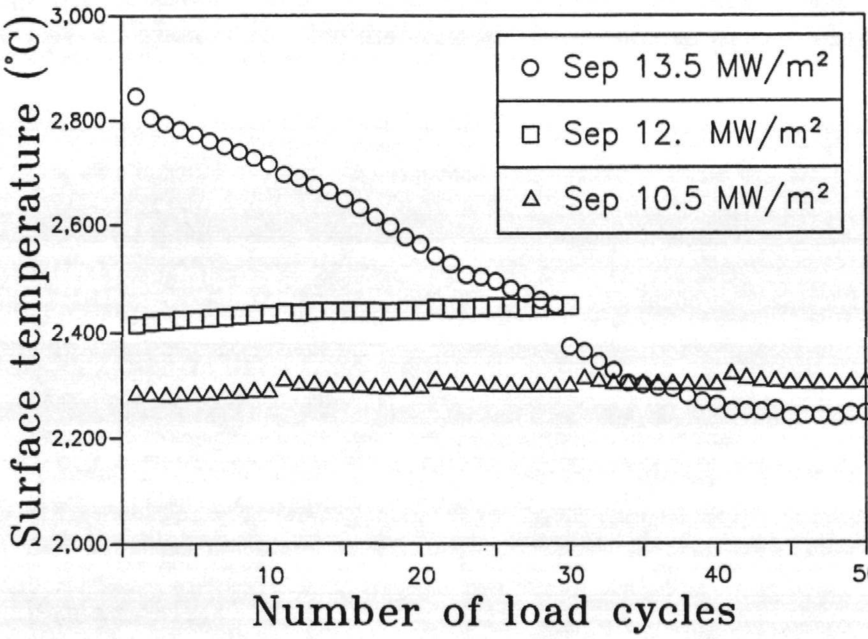

Fig. 5.8. Fatigue behavior of the divertor mock-ups under three different power densities. (Sepcarb N112/TZM joint.)

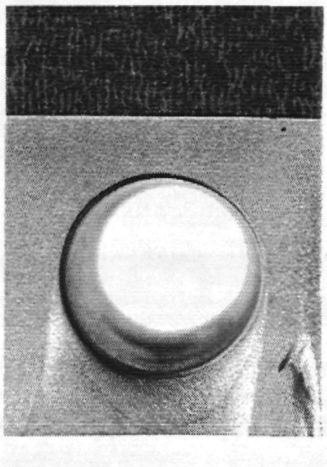

Fig. 5.9 (a)

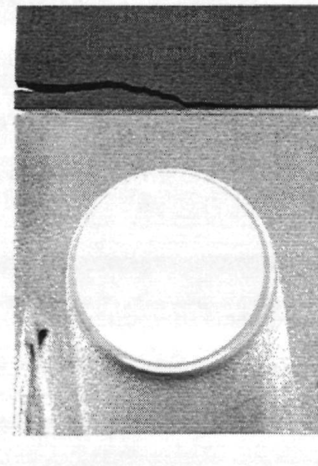

Fig. 5.9 (b)

Fig. 5.9. Cross section of the divertor mock-ups tested in the HHF cycling simulations.

(a) Sepcarb N112/TZM module (13.5 MW/m^2, 50 cycles)

(b) SiC 30/TZM module (7 MW/m^2, 2 cycles)

In microscopic scale of relatively high magnification (1200 times magnification), the damages occuring in the CFC/TZM interface can be observed (Fig.5.10). These microcracks seem to be responsible for the slow increase of the steady state surface temperature from shot to shot during the thermal fatigue.

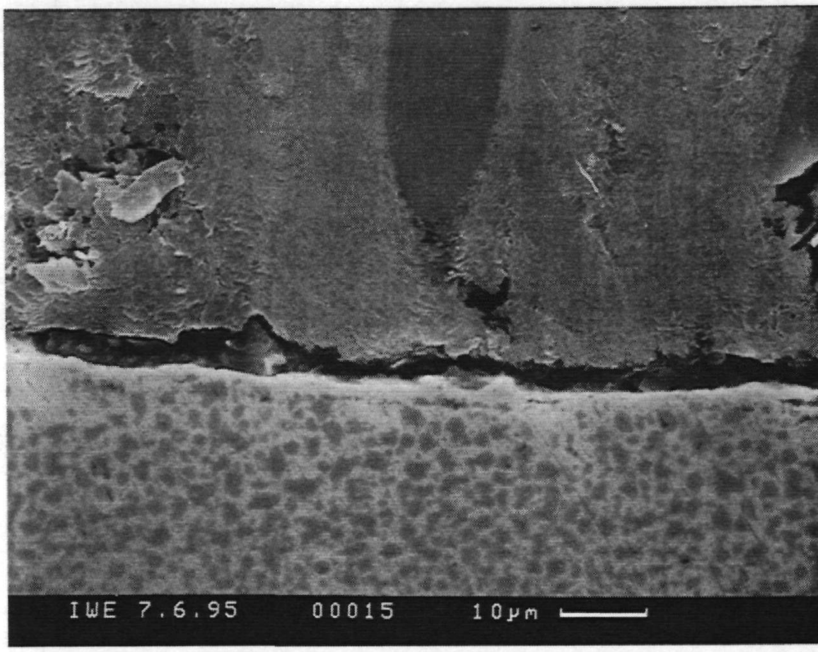

Fig. 5.10 (a) Sepcarb N112/TZM joint (13.5 MW/m^2, 50 cycles)

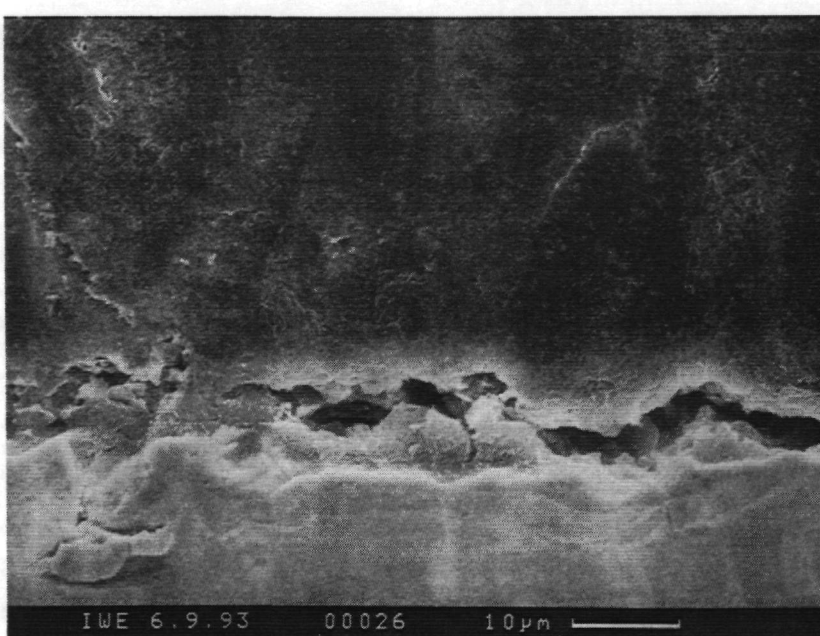

Fig. 5.10 (b) PCC 2S/TZM joint (10.5 MW/m^2, 30 cycles)

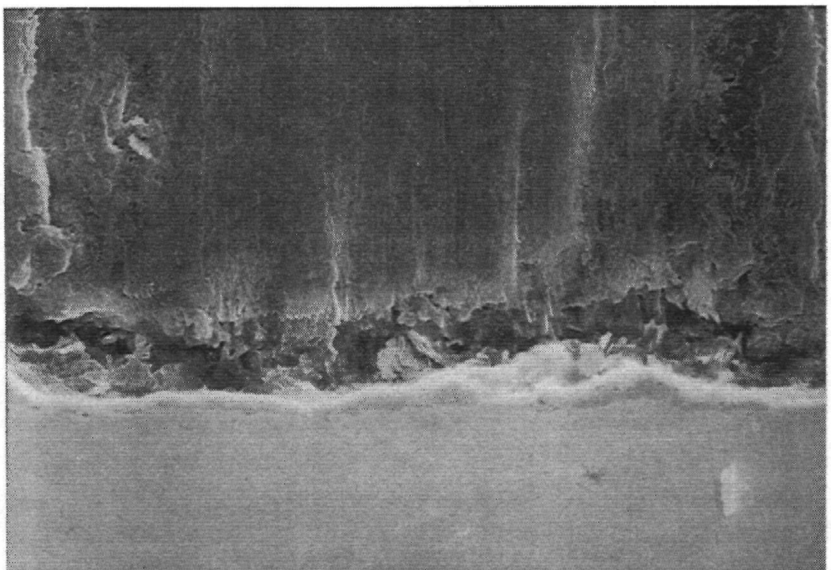

Fig. 5.10 (c) MFC 1/TZM joint (10.5 MW/m^2, 30 cycles)

Fig. 5.10. Microscopic damages near the bond interface of the divertor joints.

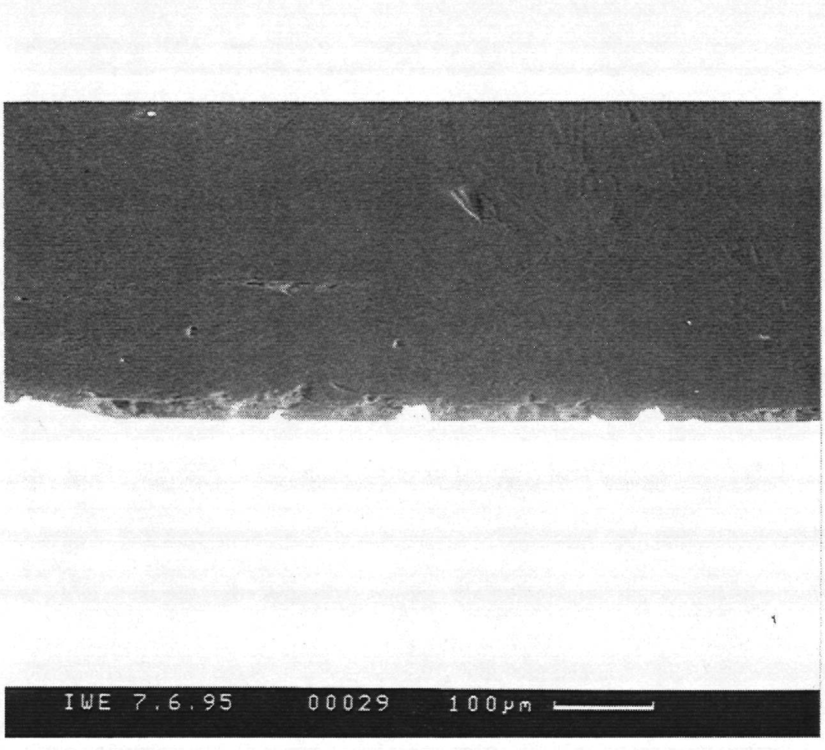

Fig. 5.11 (a) 10.5 MW/m^2, 30 cycles

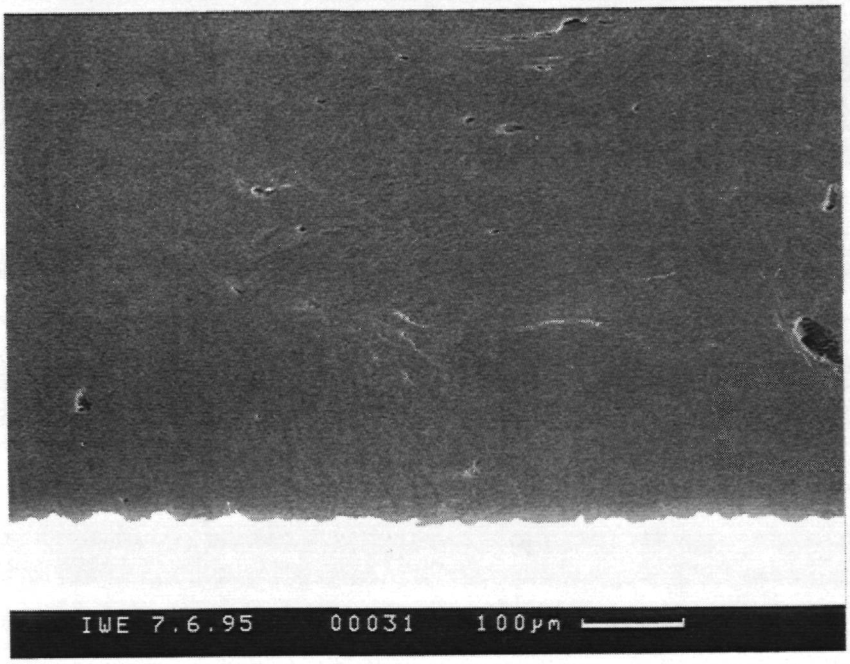

Fig. 5.11 (b) 12 MW/m^2, 30 cycles

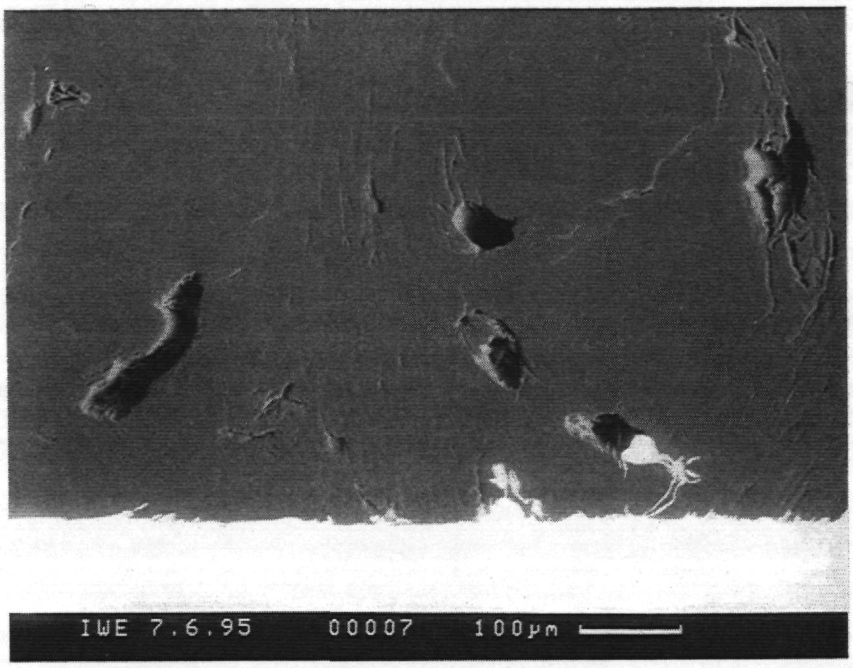

Fig. 5.11 (c) 13.5 MW/m^2, 50 cycles

Fig. 5.11. Microstructural change of the CFC tiles (Sepcarb N112/TZM joint)

Microstructures of Sepcarb N112 tiles after the HHF cycling tests are shown in Fig.5.11. Cyclic thermal loads with power density below 12 MW/m^2 caused no significant microstructural damage in the armor tiles. For the tile subjected to power density of 13.5 MW/m^2, the formation of pores with diameter in the range of 50-100 μm was the dominant microstructural change.
Severe thermal erosion took place on the surface of this tile, which was not the case for power density below 12 MW/m^2.

4.2. Numerical analysis

In the followings, the structure-mechanical response of the divertor test mock-ups is discussed.
The analysis was carried out using the finite element method. The reference HHF load cycle given in Fig.5.4 was taken as the input thermal history for the stress calculation.

As a representative case, the result for the Sepcarb N112/TZM joint is presented in detail. Fig.5.12 shows the deformed structures of the mock-up cross section with a displacement magnification of twenty times.
The cooling tube has contracted markedly. The divertor mock-ups consisting of the other material combinations showed the same feature in the deformed structure except for the MFC1/TMZ joint. The MFC1 tile shrinks more than the TZM body in the residual stress state.

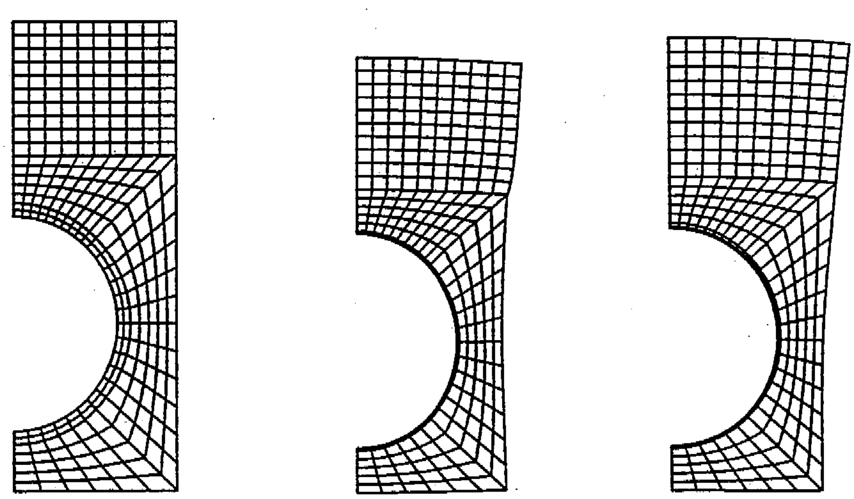

1070 °C (brazing temp.) (a)   20 °C (residual state) (b)   HHF (steady state) (c)

Fig. 5.12. Deformed structure of the divertor cross section (Sepcarb N112/TZM joint).
(a) Stress free state (in brazing temperature)
(b) Residual stress state (in room temperature)
(c) Steady state in the HHF loading (10.5 MW/m^2, 30 s)

The time history of the thermal stress components is plotted in Fig.5.13 for some selected positions in the mock-up cross section. The locations considered are shown in Fig.5.13(a).

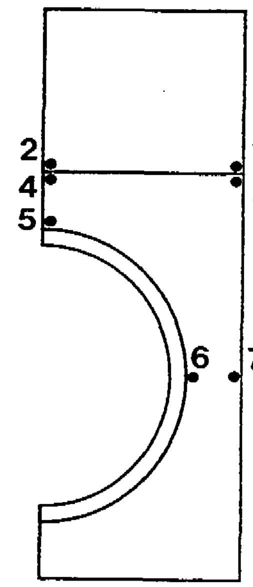

Fig.5.13 (a) Location of the node points.

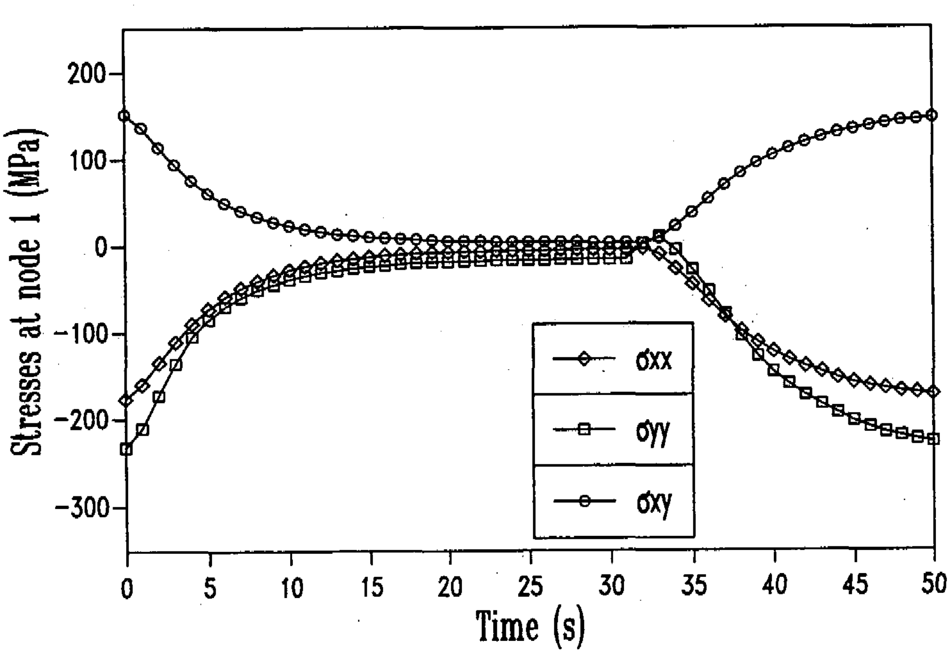

Fig.5.13 (b) Node point 1

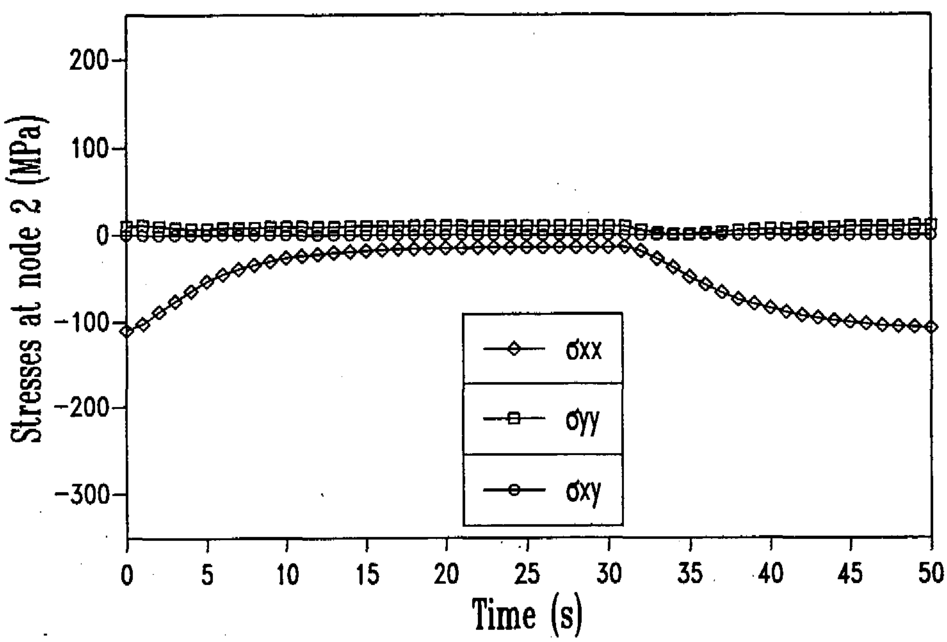

Fig.5.13 (c) Node point 2

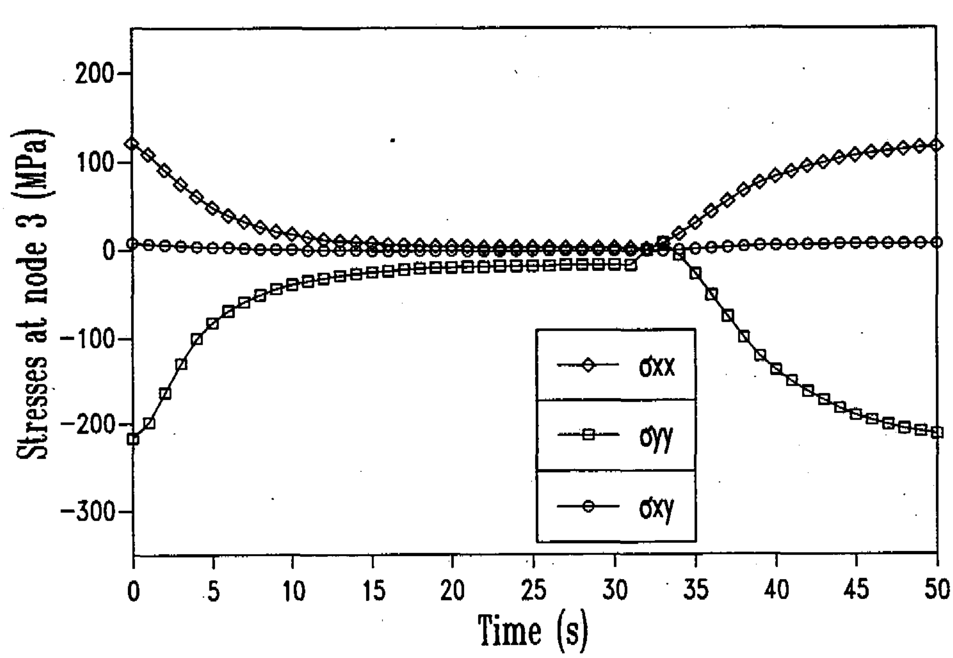

Fig.5.13 (d) Node point 3

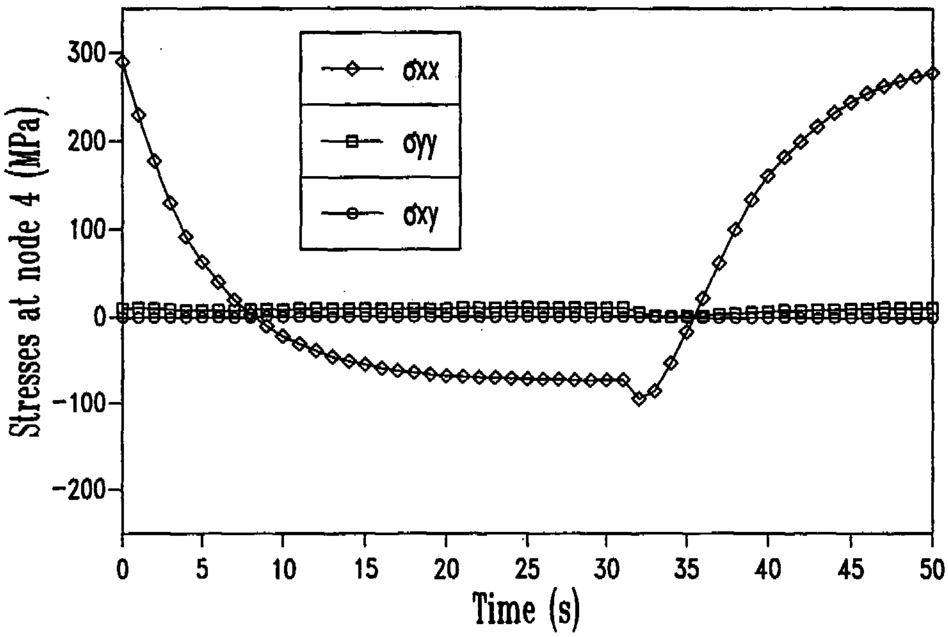

Fig.5.13 (e) Node point 4

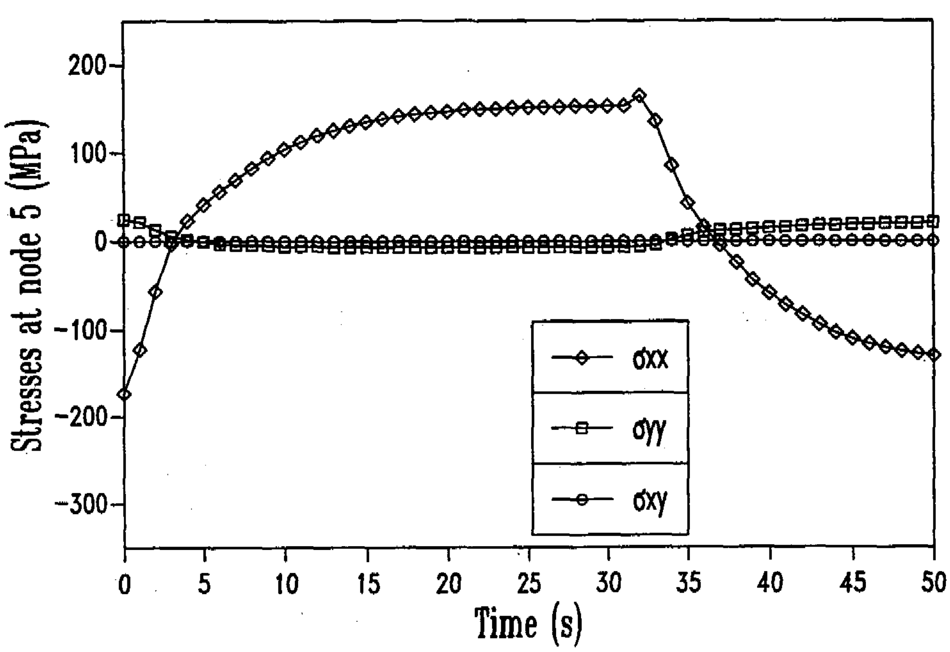

Fig.5.13 (f) Node point 5

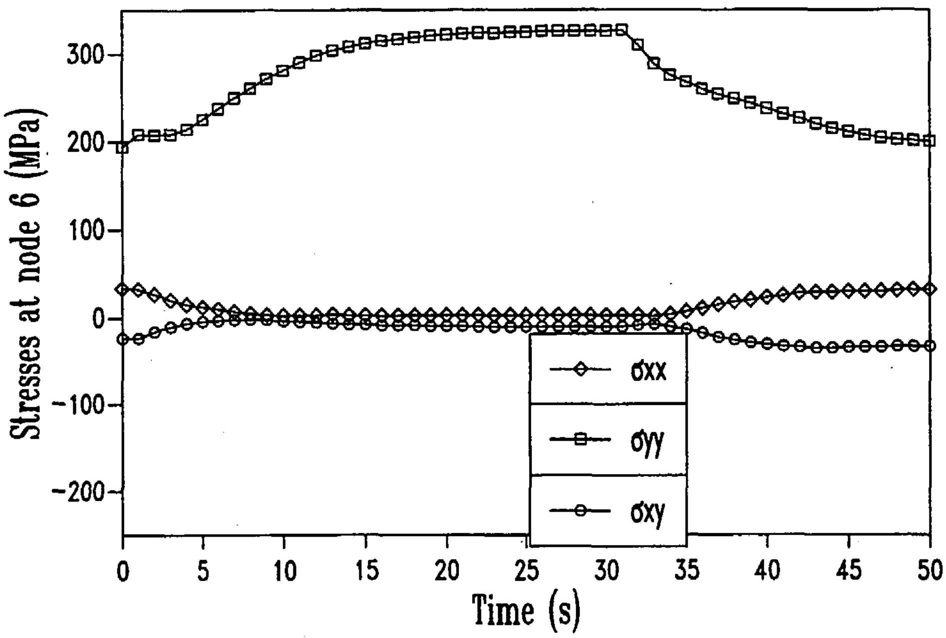

Fig.5.13 (g) Node point 6

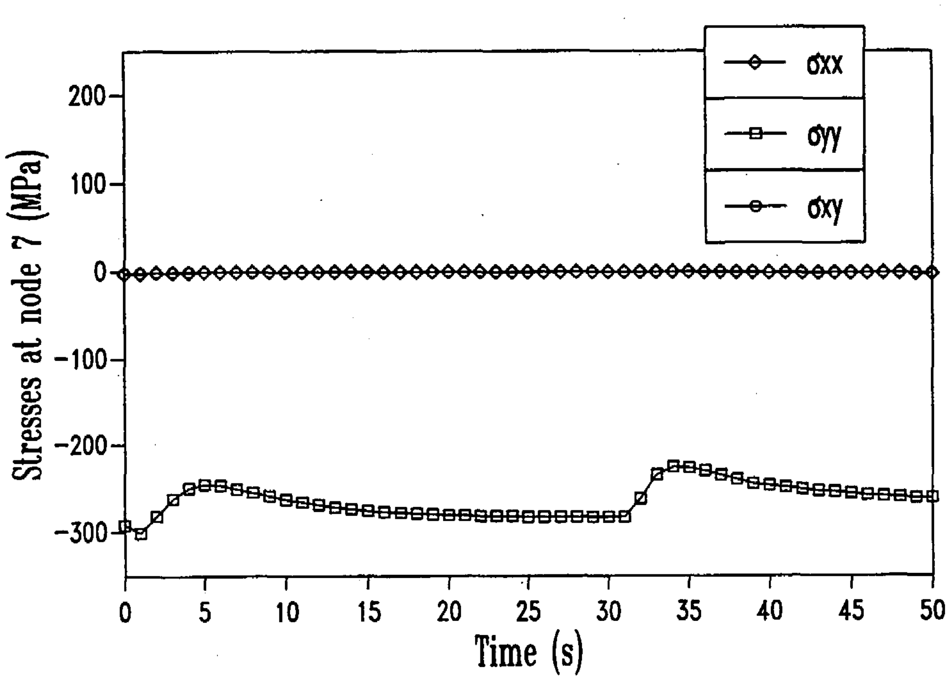

Fig.5.13 (h) Node point 7

Fig. 5.13. Time history of the thermal stress in the TZM body during the HHF load cycle. (Sepcarb N112/TZM joint. 10.5 MW/m^2, 30 s)

For the given reference thermal load cycle, the variation mode of the stresses can be categorized in three groups.
The node points 1, 2 and 3 show a repeated mode, where the stress components vary between the maximum stress state and the stress free state without changing their signs.
The maximum stresses occur in the residual stress state and the stresses are relieved during the thermal loading. The node points 1 and 3 which locate near the free surface edge of the interface experience a multiaxial stress field.
The node points 4 and 5 show a reversed mode, where the sign of the stress components is reversed during the cycle with large range of the stress amplitude.
The cyclic nature of the stress at the node point 6 and 7 is much less conspicuous than the other positions. These points remain highly stressed during the whole load cycle with small stress amplitudes.
Except for the node points 1 and 3, the stress state for the other locations is almost uniaxial during the cycle.

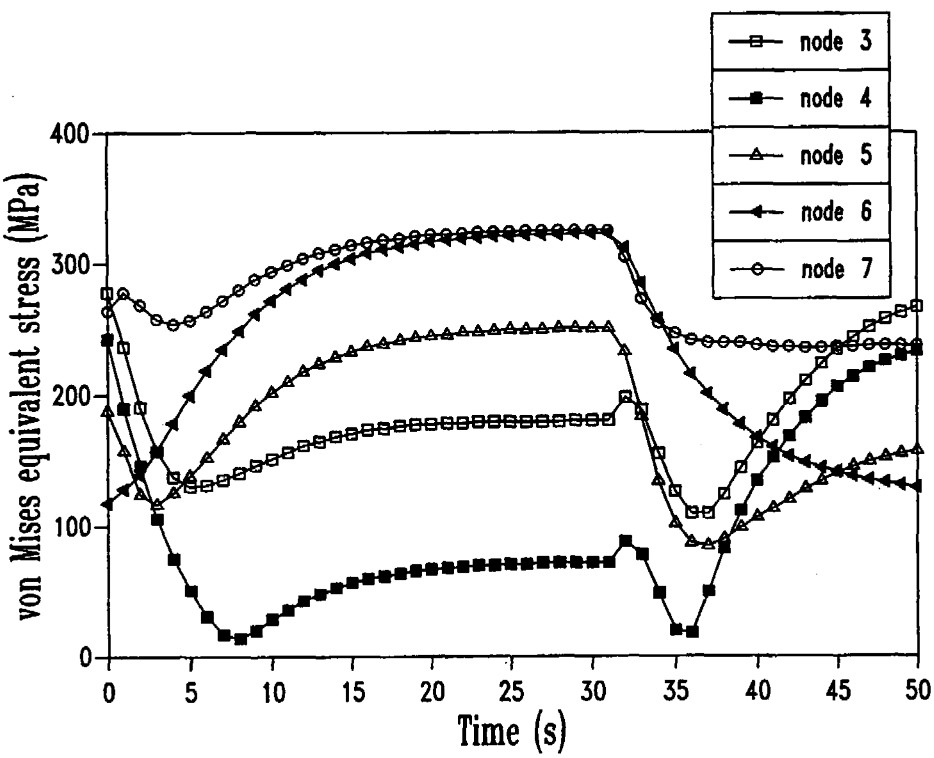

Fig. 5.14. Variation of the von Mises equivalent stress in the TZM body during the HHF load cycle. (Sepcarb N112/TZM joint. 10.5 MW/m^2, 30 s)

The cyclic variation of the von Mises equivalent stress for the five node points in the TZM body is plotted in Fig.5.14. The stress at nodes 3, 4 and 5 show fluctuation after the load pulse. The von Mises equivalent stress at each position does not exceed the elastic limit.
From the equivalent stress range $\Delta\sigma_{eq}$ for the load cycle, an equivalent elastic strain range $\Delta\varepsilon_{eq}^{el}$ can be obtained by [21]

$$\Delta\varepsilon_{eq}^{el} = \frac{2}{3}\cdot\frac{1+\nu}{E}\cdot\Delta\sigma_{eq} \qquad (5.1)$$

where the temperature dependence of the elastic constants should be taken into account. The calculated equivalent strain range is summarized in table 5.3.
The values in table 5.3 are overestimated in comparison to the real situation because the ductile braze layer was neglected in the stress analysis.

Table 5.3
The equivalent elastic strain amplitudes.

Node point	$\Delta\varepsilon_{eq}^{el}$ (%)
3	0.04312
4	0.06606
5	0.05227
6	0.07066
7	0.02830

The consideration of the materials strength may be essential for the estimation of the mechanical performance. The strength data are given in Fig.5.15 [14,17-19].
The data are given for two anisotropic directions (direction parallel to the fiber orientation and normal to the ply plane).
The compressive strength is higher than the tensile strength, which is general for non metallic brittle materials.
The MFC1 has a extreme anisotropy in strength.

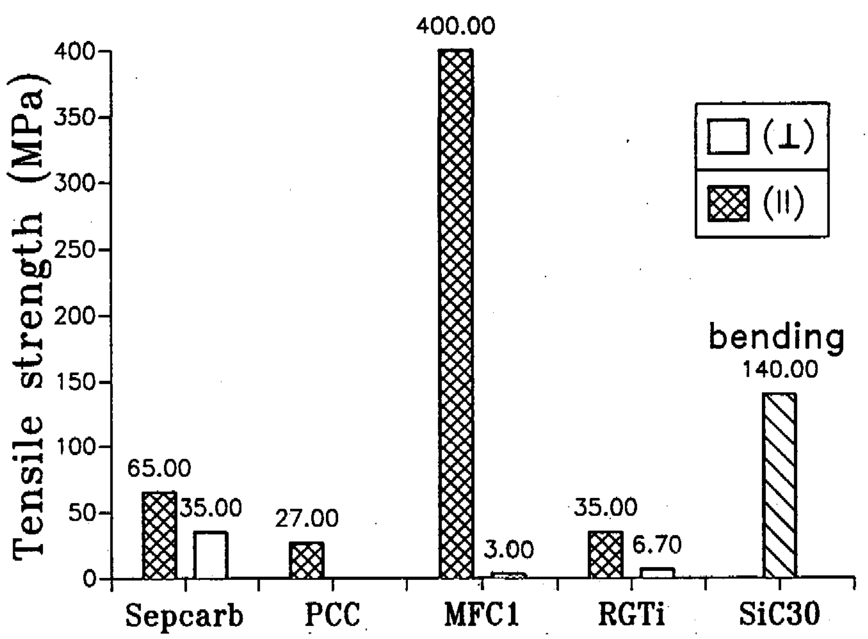

Fig. 5.15 (a) Tensile strength of the materials used.

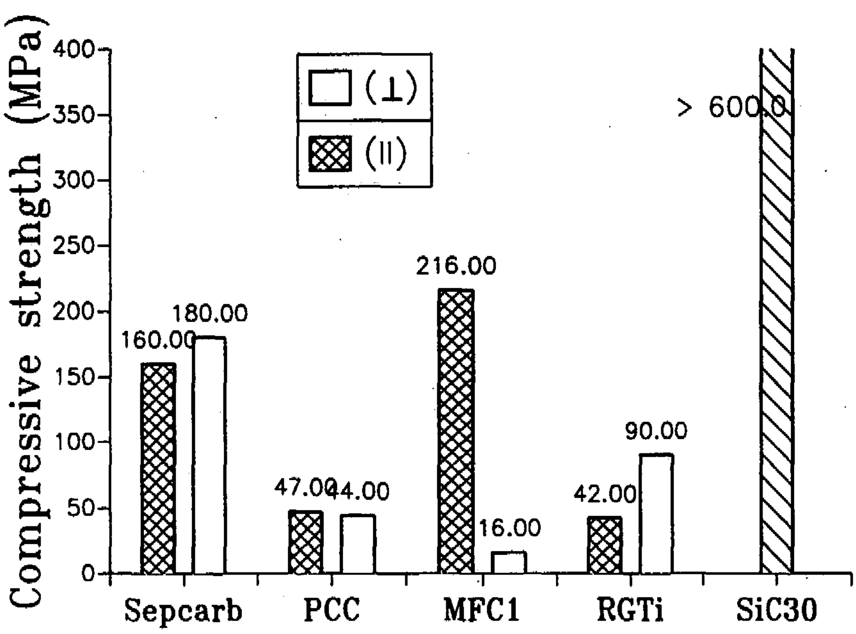

Fig. 5.15 (b) Compressive strength of the materials used.

Fig. 5.15. Strength of the armor tile materials.

One of the important load parameters to assess the fatigue lifetime of fiber reinforced composite materials is the maximum fatigue stress [22,23].

In Fig.5.16, the maximum tensile-, and compressive stresses in the interface of the armor tiles of the five test mock-ups are summarized. The results are given in three stress components both for the residual stress state and for the steady state of the HHF loading.
The tensile stresses are much lower than the compressive stresses. The MFC1 armor tile shows a much higher tensile σ_{yy} component in the residual stress state than the other armors. Since the direction of this stress component is parallel to the fiber orientation, the stress value corresponds only half of the tensile strength in that direction.
The magnitude of the compressive stress given in Fig.5.16(b) is proportionally related to the bulk stress fields. The SiC30 armor tile experiences a severe thermal stress compared to the other armor tiles. It is seen that the interfacial stresses except for the SiC30 armor tile are considerably relieved during the HHF loading.

From the results of Fig.5.15 and Fig.5.16, it is proved that the MFC1/TZM joint provides the most favorable design option. The SiC30/TZM joint is most effectively stressed by the thermomechanical load.

In Fig.5.17, the range of the von Mises equivalent stress in the HHF load cycle is given for three locations in TZM cooling body.

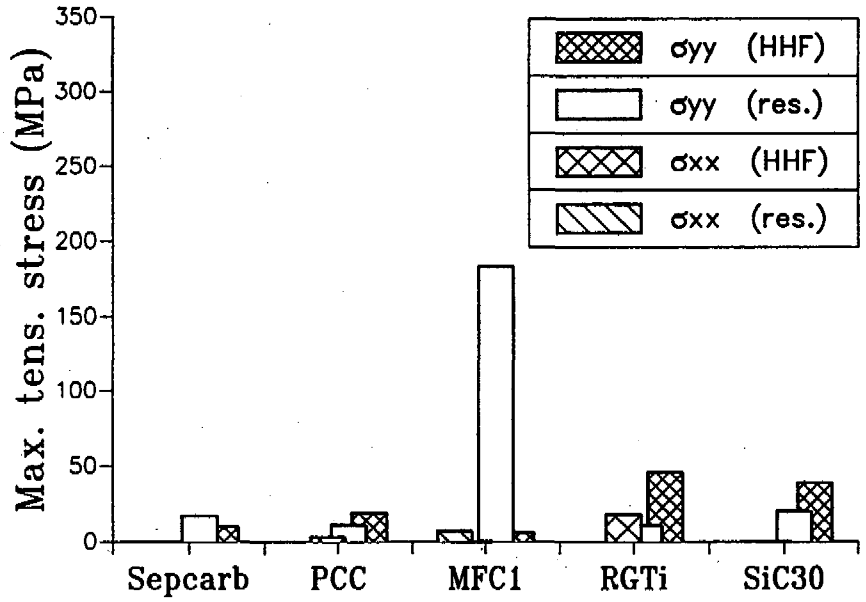

Fig. 5.16 (a) Tensile stress

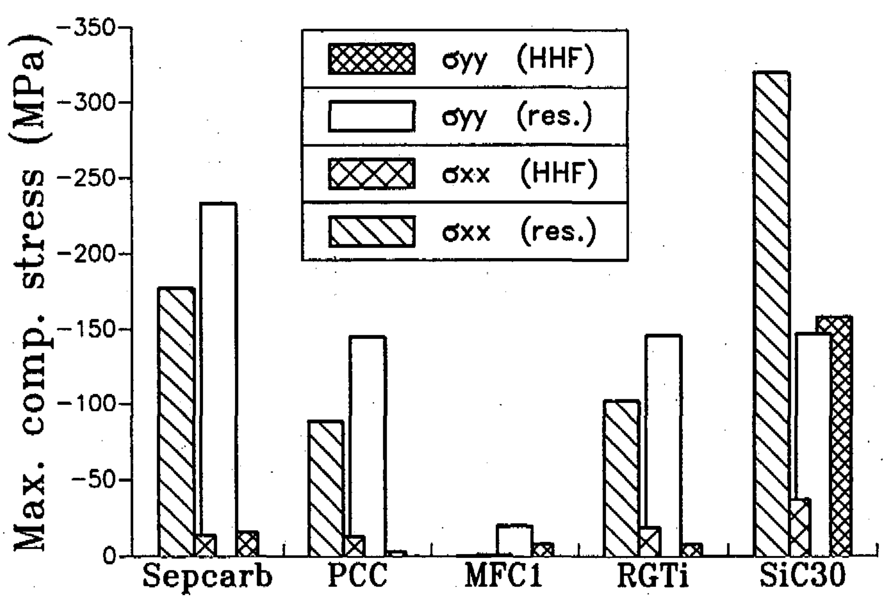

Fig. 5.16 (b) Compressive stress

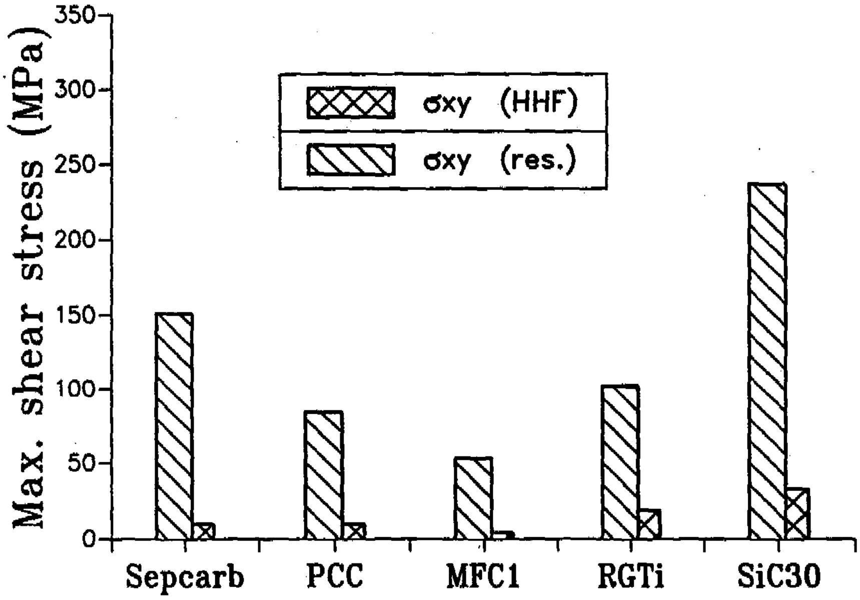

Fig. 5.16 (c) Shear stress

Fig. 5.16. Maximum stress occuring in bond interface of the armor tiles. (10.5 MW/m^2, 30 s)

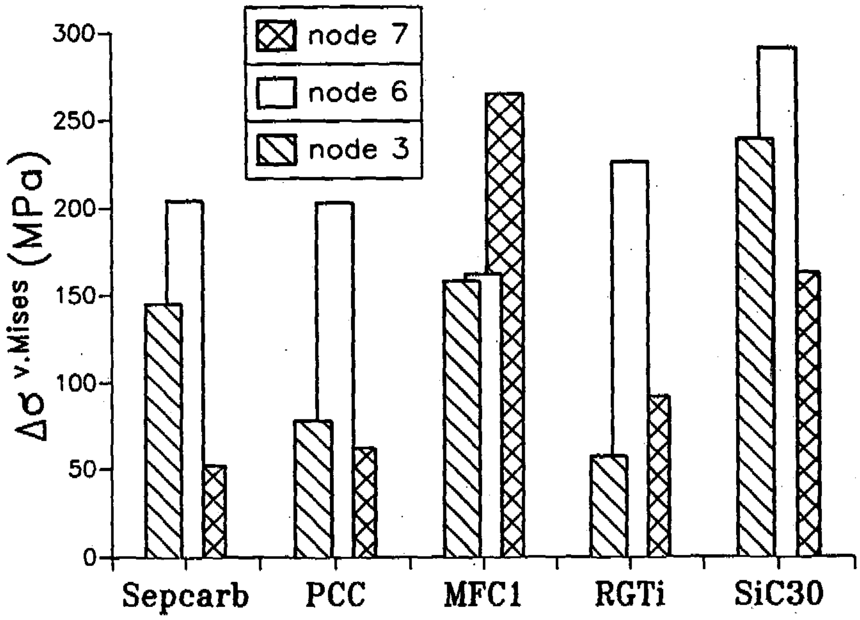

Fig. 5.17. Range of the equivalent stress in the TZM body during the HHF load cycle. (10.5 MW/m^2, 30 s)

The node point 6 undergoes the largest stress range than the other positions except for the MFC1/TZM joint. Considering the mechanical strength, the thermomechanical loading in the TZM body seems to be less serious than that of the armor tiles.

5. Conclusion

To simulate the cyclic HHF operations of the divertor components, actively cooled, brazed joint mock-ups were tested under cyclic electron beam irradiations. Five different armor tile materials with TZM heat sink were used.

For the reference power density of 10.5 MW/m^2, thermal equilibrium was achieved within 20 seconds. The experimental results for the thermal response of the divertor mock-ups showed good agreement with the numerical analysis.

The test mock-up with the MFC1/TZM joint showed an excellent heat removal ability. In the screening tests, the temperatures increased linearly with the input power density ranging from 7 MW/m^2 to 12 MW/m^2. The mock-ups armored with CFC tiles showed a good fatigue resistance and their thermal performance was stable. The electron microscopy revealed some microscopic damages in the bond interface.

On the contrary, the mock-ups with graphite or ceramic tiles could survive only a single shut resulting in a abrupt fracture of the bont interface. The module with the Sepcarb N112/TZM joint showed a substantial thermal erosion under heat flux of 13.5 MW/m^2.

Finite element method is employed to calculate the temperature and stress fields of the test mock-ups. The divertor mock-up with Sepcarb N112/TZM combination was analysed in detail.

In the steady state, the temperature difference of 1200 °C has developed within the armor tile thickness.

The stress evolution for the reference HHF pulse could be categorized in three fatigue modes. These are repeated mode, reversed mode and quasi-static mode.

The interfacial stresses are relieved considerably during the thermal loading. Based on the equivalent stress amplitudes, maximum strain amplitudes were determined.

The thermal stresses of the divertor modules for five different material combinations were investigated. The SiC30 armor tile experiences severe thermal stresses compared to the other armor tiles. The MFC1/TZM combination provides most favorable design options.

6. reference

[1] "ABAQUS User's Manual 5.4", Hibbit, Karlson and Sorenson Inc., Providence, RI, USA., 1994

[2] I. Smid, M. Akiba, M. Araki, S. Suzuki, K. Satoh, "Material and Design Considerations for the Carbon Armored ITER Divertor", JAERI Report, JAERI-M 93-149, Japan Atomic Energy Research Institute (1993)

[3] E. Zolti, "Material Data for Predesign Analysis of In Vessel Components", ITER Internal Report ITER-IN-N/I/3300/5/A (1990)

[4] "Sepcarb N112 - A general presentation", Sep Documentation

[5] JAERI JT-60 Team, JAERI Report, JAERI-M 90-119, Japan Atomic Energy Research Institute (1990)

[6] T.A. Burtseva, O.K. Chugunov, E.F. Dovguchits, I.V. Mazul, Shibkov, V.A. Sokolov, M.I. Persin, P.A. Platonov, Proc. 6th Intern. Workshop on Carbon Materials (Jülich, Germany, 1993), Carbon Materials - Binary Materials for Plasma Facing Components, pp. 43-60

[7] Datenblatt : Werkstoff - SiC30, Schunk Kohlenstofftechnik GmbH, (1991)

[8] L. Binkele, private communication

[9] E. Diegele, D. Munz, G. Schweinfurther, "Lifetime Prediction for the First Wall of a Fusion Machine", KfK-Bericht, KfK 5283, Kernforschungszentrum Karlsruhe GmbH, Karlsruhe

[10] B. Liu, L.B. Lessard, Composite Sci. Tech., 51 (1994), pp. 43-51

[11] A. El-Azab, N.M. Ghoniem, Proc. ISFNT-3 (Los Angeles, CA, USA, 1994), Fus. Eng. Des. 27 (1995), pp. 536-543

Appendix

A. Stress solution for the singular field near free surface edge

$$\sigma_{jrr}(r,\theta)=\sum_{n} r^{-\omega_k}(1-\omega_k)\{A_{jn}(2+\omega_k)\sin(\omega_k\theta)+B_{jn}(2+\omega_k)\cos(\omega_k\theta)$$
$$-C_{jn}(2-\omega_k)\sin[(2-\omega_k)\theta]-D_{jn}(2-\omega_k)\cos[(2-\omega_k)\theta]\} \tag{A.1-a}$$

$$\sigma_{j\theta\theta}(r,\theta)=\sum_{n} r^{-\omega_k}(2-\omega_k)(1-\omega_k)\{A_{jn}\sin(\omega_k\theta)+B_{jn}\cos(\omega_k\theta)$$
$$+C_{jn}\sin[(2-\omega_k)\theta]-D_{jn}\cos[(2-\omega_k)\theta]\} \tag{A.1-b}$$

$$\tau_{jr\theta}(r,\theta)=-\sum_{n} r^{-\omega_k}(1-\omega_k)\{A_{jn}\omega_k\cos(\omega_k\theta)-B_{jn}\omega_k\sin(\omega_k\theta)$$
$$+C_{jn}(2-\omega_k)\cos[(2-\omega_k)\theta]-D_{jn}(2-\omega_k)\sin[(2-\omega_k)\theta]\} \tag{A.1-c}$$

For the special geometry with wedge angle of $\theta_1=-\theta_2=\frac{\pi}{2}$ (see Fig.2.2, Fig.3.1) the coefficients are given as

$$A_{jk}=\frac{A^*_{jk}}{Z},\ B_{jk}=\frac{B^*_{jk}}{Z},\ C_{jk}=\frac{C^*_{jk}}{Z},\ D_{jk}=\frac{D^*_{jk}}{Z} \tag{A.2-a}$$

with

$$Z=\beta\left[\cos^2\left(\frac{\pi}{2}\omega_k\right)+(\omega_k-1)(\omega_k-3)\right]-\alpha(\omega_k-2)(\omega_k-1)-1+\cos^2\left(\frac{\pi}{2}\omega_k\right) \tag{A.2-b}$$

$$A^*_{1k}=Z \tag{A.2-c}$$

$$B^*_{1k}=-\tan\left(\frac{\pi}{2}\omega_k\right)\left\{\beta\left[\cos^2\left(\frac{\pi}{2}\omega_k\right)+(\omega_k-1)^2\right]-\alpha(\omega_k-2)(\omega_k-1)+\cos^2\left(\frac{\pi}{2}\omega_k\right)\right\} \tag{A.2-d}$$

$$C^*_{1k}=\beta\left[\frac{4-3\omega_k}{\omega_k-2}\sin^2\left(\frac{\pi}{2}\omega_k\right)-(\omega_k-2)\omega_k\right]+\alpha\,\omega_k(\omega_k-1)+\sin^2\left(\frac{\pi}{2}\omega_k\right) \tag{A.2-e}$$

$$D^*_{1k} = \tan\left(\frac{\pi}{2}\omega_k\right)\left\{\frac{\beta}{\omega_k - 2}\left[\cos^2\left(\frac{\pi}{2}\omega_k\right)(3\omega_k - 4) - \omega_k(\omega_k - 1)^2\right] + \alpha\omega_k(\omega_k - 1)\right.$$
$$\left.-\cos^2\left(\frac{\pi}{2}\omega_k\right)\right\} \qquad \text{(A.2-f)}$$

$$A^*_{2k} = -\frac{1}{1+\alpha}\left\{\alpha^2(\omega_k - 2)(\omega_k - 1)(2\omega_k - 1) + 2\beta^2\left[(\omega_k - 2)\sin^2\left(\frac{\pi}{2}\omega_k\right) + (\omega_k - 2)^2\omega_k\right]\right.$$
$$+\alpha\beta\left[\cos^2\left(\frac{\pi}{2}\omega_k\right)(2\omega_k - 3) - 4(\omega_k - 2)^3 - 9(\omega_k - 2)^2 - 6(\omega_k - 2) - 1\right]$$
$$+\alpha\left[-\cos^2\left(\frac{\pi}{2}\omega_k\right)(2\omega_k - 3) + (\omega_k - 2)^2 + 3(\omega_k - 2) + 1\right]$$
$$\left.+\beta\left[-\sin^2\left(\frac{\pi}{2}\omega_k\right)(2\omega_k - 3) - (\omega_k - 2)^2\right] + \sin^2\left(\frac{\pi}{2}\omega_k\right)\right\} \qquad \text{(A.2-g)}$$

$$B^*_{2k} = -\frac{\tan\left(\frac{\pi}{2}\omega_k\right)}{1+\alpha}\left\{\alpha^2(\omega_k - 2)(\omega_k - 1)(2\omega_k - 1)\right.$$
$$+2\beta^2\left[-(\omega_k - 1)\cos^2\left(\frac{\pi}{2}\omega_k\right) + (\omega_k - 2)^3 + 3(\omega_k - 2)^2 + 3(\omega_k - 2) + 1\right]$$
$$+\alpha\beta\left[\cos^2\left(\frac{\pi}{2}\omega_k\right)(2\omega_k - 3) - 4(\omega_k - 2)^3 - 11(\omega_k - 2)^2 - 10(\omega_k - 2) - 3\right]$$
$$+\alpha\left[-\cos^2\left(\frac{\pi}{2}\omega_k\right)(2\omega_k - 3) - (\omega_k - 2)^2 - (\omega_k - 2)\right]$$
$$\left.+\beta\left[\cos^2\left(\frac{\pi}{2}\omega_k\right)(2\omega_k - 3) + (\omega_k - 2)^2 + (2\omega_k - 3)\right] + \cos^2\left(\frac{\pi}{2}\omega_k\right)\right\}$$
$$\text{(A.2-h)}$$

$$C^*_{2k} = -\frac{1}{1+\alpha}\left\{\alpha^2\omega_k\left[2(\omega_k - 2)^2 + 3(\omega_k - 2) + 1\right]\right.$$
$$+2\beta^2\omega_k\left[-\cos^2\left(\frac{\pi}{2}\omega_k\right) + (\omega_k - 2)^2 + 2(\omega_k - 2) + 1\right]$$
$$+\frac{\alpha\beta}{\omega_k - 2}\left[\cos^2\left(\frac{\pi}{2}\omega_k\right)(2\omega_k^2 - 5\omega_k + 4) - 4\omega_k^4 + 17\omega_k^3 - 26\omega_k^2 + 17\omega_k - 4\right]$$
$$+\alpha\left[\cos^2\left(\frac{\pi}{2}\omega_k\right)(1 - 2\omega_k) - (\omega_k - 2)^2 - (\omega_k - 2) + 1\right]$$
$$\left.+\frac{\beta}{\omega_k - 2}\left[\cos^2\left(\frac{\pi}{2}\omega_k\right)(2\omega_k^2 - 5\omega_k + 4) + \omega_k^3 - 6\omega_k^2 + 9\omega_k - 4\right] - \sin^2\left(\frac{\pi}{2}\omega_k\right)\right\}$$
$$\text{(A.2-i)}$$

$$D^{*}_{2k} = -\frac{\tan\left(\frac{\pi}{2}\omega_k\right)}{1+\alpha}\left\{\alpha^2\omega_k\left[2(\omega_k-2)^2+3(\omega_k-2)+1\right]\right.$$
$$+2\beta^2\left[-(\omega_k-1)\cos^2\left(\frac{\pi}{2}\omega_k\right)+(\omega_k-2)^3+3(\omega_k-2)^2+3(\omega_k-2)+1\right]$$
$$+\frac{\alpha\beta}{\omega_k-2}\left[\cos^2\left(\frac{\pi}{2}\omega_k\right)\left(2\omega_k^2-5\omega_k+4\right)-4\omega_k^4+19\omega_k^3-34\omega_k^2+27\omega_k-8\right]$$
$$+\alpha\left[\cos^2\left(\frac{\pi}{2}\omega_k\right)(1-2\omega_k)+\omega_k(\omega_k-1)\right]$$
$$\left.+\frac{\beta}{\omega_k-2}\left[\cos^2\left(\frac{\pi}{2}\omega_k\right)\left(2\omega_k^2-5\omega_k+4\right)-\omega_k(\omega_k-1)^2\right]-\cos^2\left(\frac{\pi}{2}\omega_k\right)\right\} \tag{A.2-j}$$

where α and β represent the Dundurs Parameter (see eq.(2.8), eq.(3.19)).

B. Angle functions of the stress singularity

The angle functions in eq.(2.5) and eq.(3.16) have following forms.

$$f_{jrrk}(\theta)=\left\{A_{jk}(2+\omega_k)\sin(\omega_k\theta)+B_{jk}(2+\omega_k)\cos(\omega_k\theta)-C_{jk}(2-\omega_k)\sin[(2-\omega_k)\theta]\right.$$
$$\left.-D_{jk}(2-\omega_k)\cos[(2-\omega_k)\theta]\right\}/\left\{(2-\omega_k)(B_{jk}+D_{jk})\right\} \tag{B.1-a}$$

$$f_{j\theta\theta k}(\theta)=\left\{A_{jk}\sin(\omega_k\theta)+B_{jk}\cos(\omega_k\theta)+C_{jk}\sin[(2-\omega_k)\theta]\right.$$
$$\left.+D_{jk}\cos[(2-\omega_k)\theta]\right\}/\left(B_{jk}+D_{jk}\right) \tag{B.1-b}$$

$$f_{jr\theta k}(\theta)=-\left\{A_{jk}\omega_k\cos(\omega_k\theta)-B_{jk}\omega_k\sin(\omega_k\theta)+C_{jk}(2-\omega_k)\cos[(2-\omega_k)\theta]\right.$$
$$\left.-D_{jk}(2-\omega_k)\sin[(2-\omega_k)\theta]\right\}/\left\{(2-\omega_k)(B_{jk}+D_{jk})\right\} \tag{B.1-c}$$

where the coefficients $A_{jk}, B_{jk}, C_{jk}, D_{jk}$ are given in eq.(A.2).

Thermal stress fields (CFC/Cu/TZM joint) σ_{xx} component

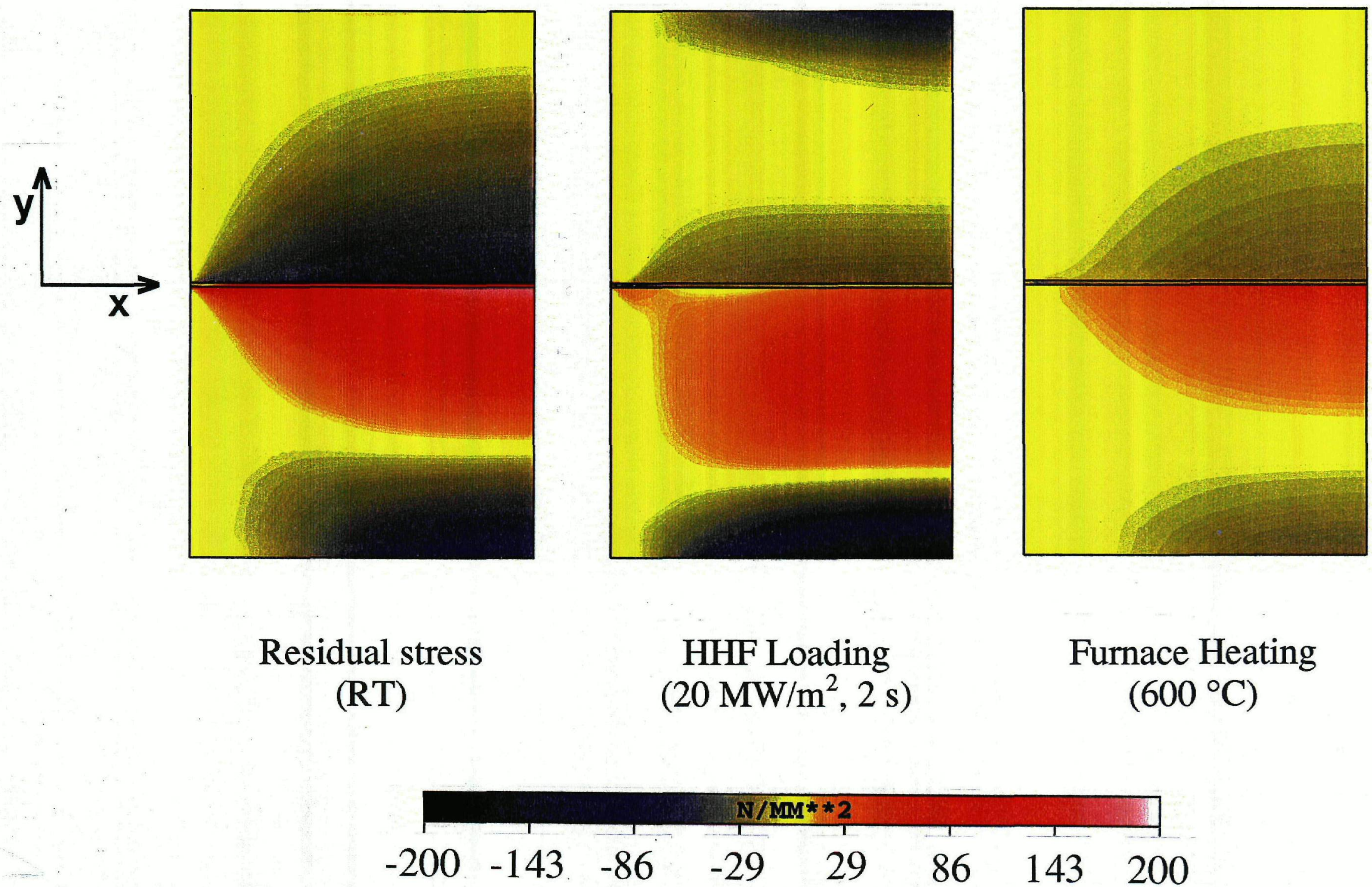

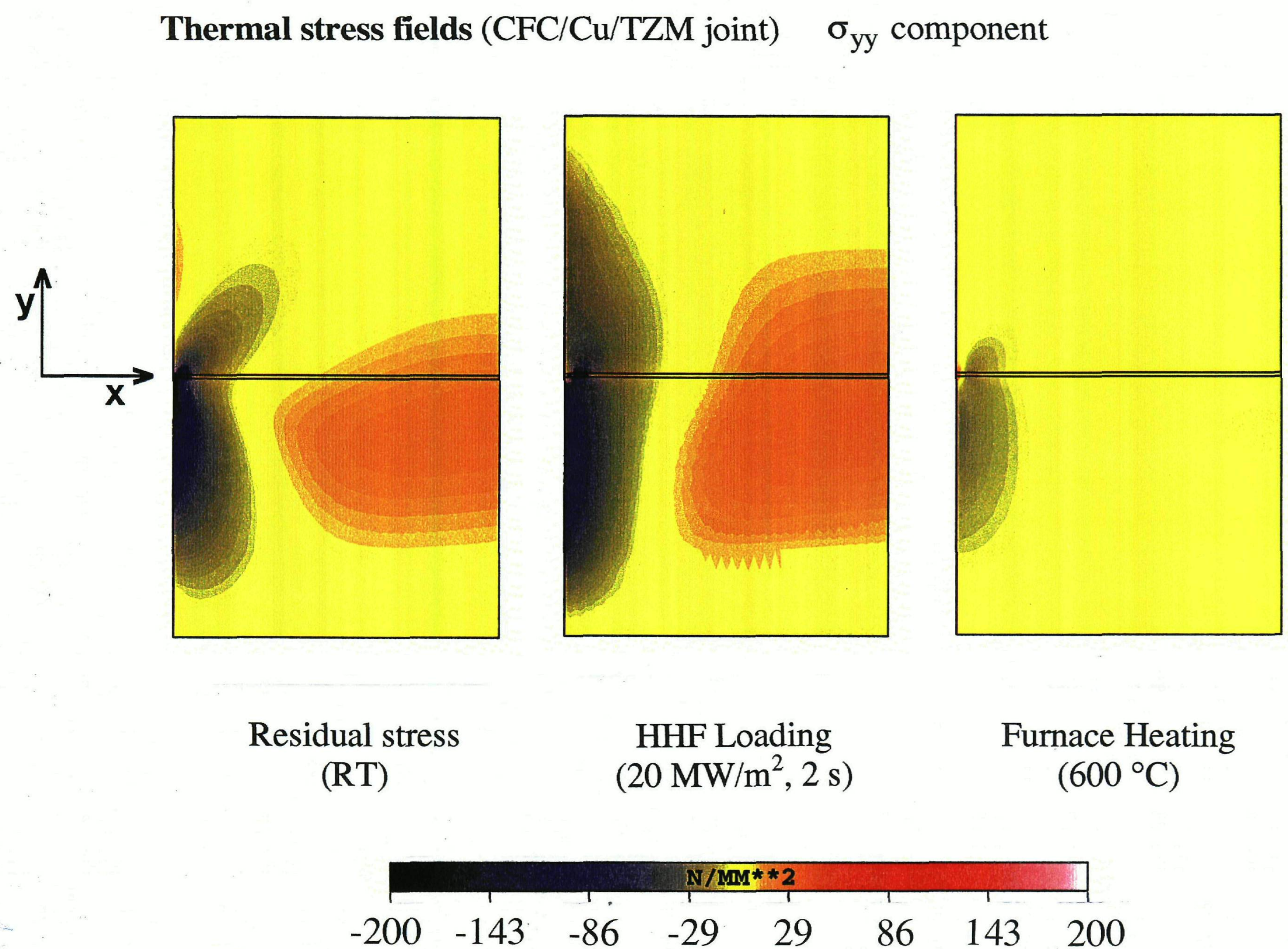

Thermal stress fields (CFC/Cu/TZM joint) σ_{yy} component
y
x
Residual stress
(RT)
HHF Loading
(20 MW/m^2, 2 s)
Furnace Heating
(600 °C)
N/MM**2
-200
-143
-86
-29
29
86
143
200

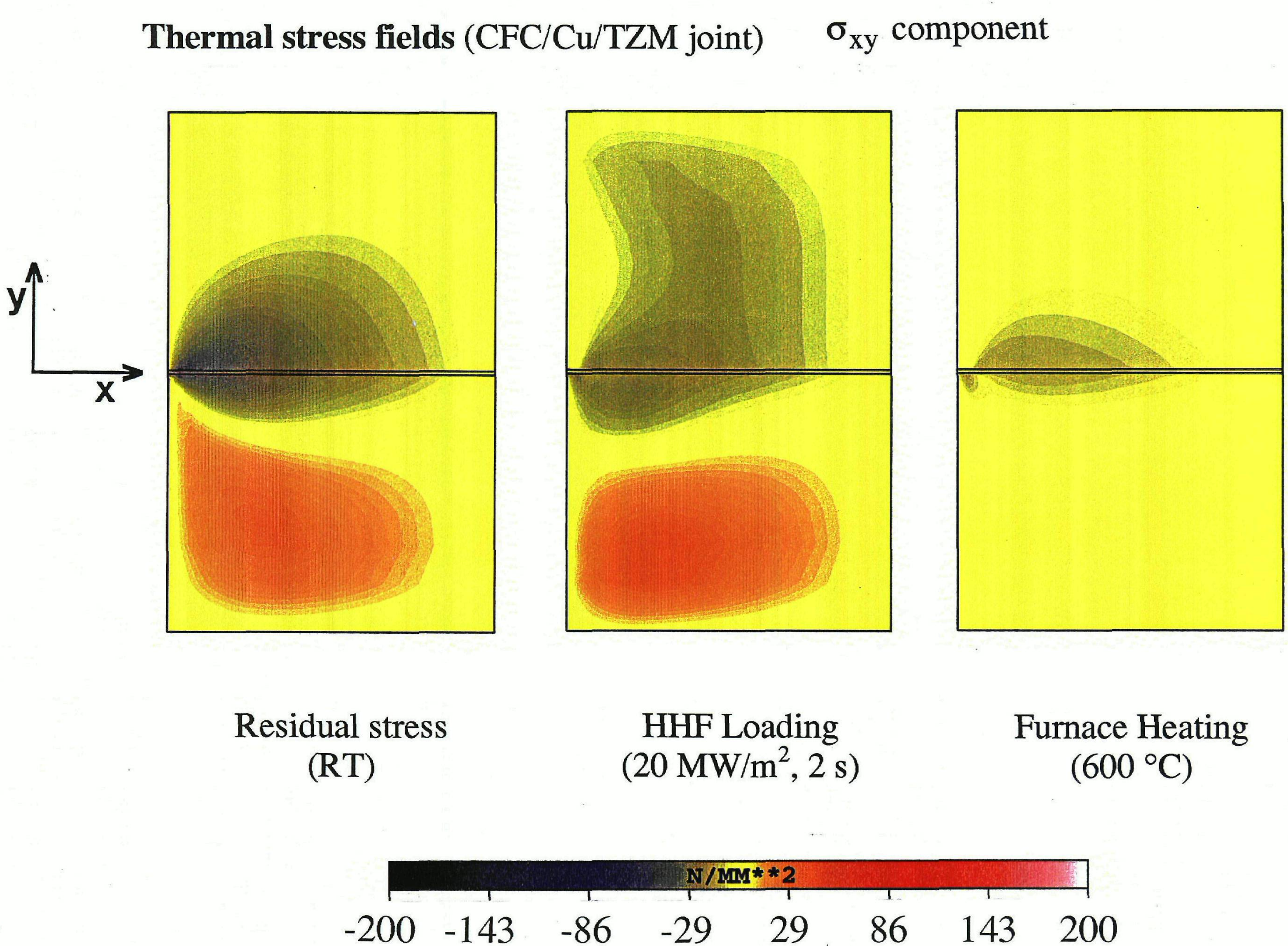
Thermal stress fields (CFC/Cu/TZM joint)
σ_{xy} component
y
x
Residual stress
(RT)
HHF Loading
(20 MW/m^2, 2 s)
Furnace Heating
(600 °C)
N/MM**2
-200 -143 -86 -29 29 86 143 200

Temperature fields (10.5 MW/m^2, steady state)

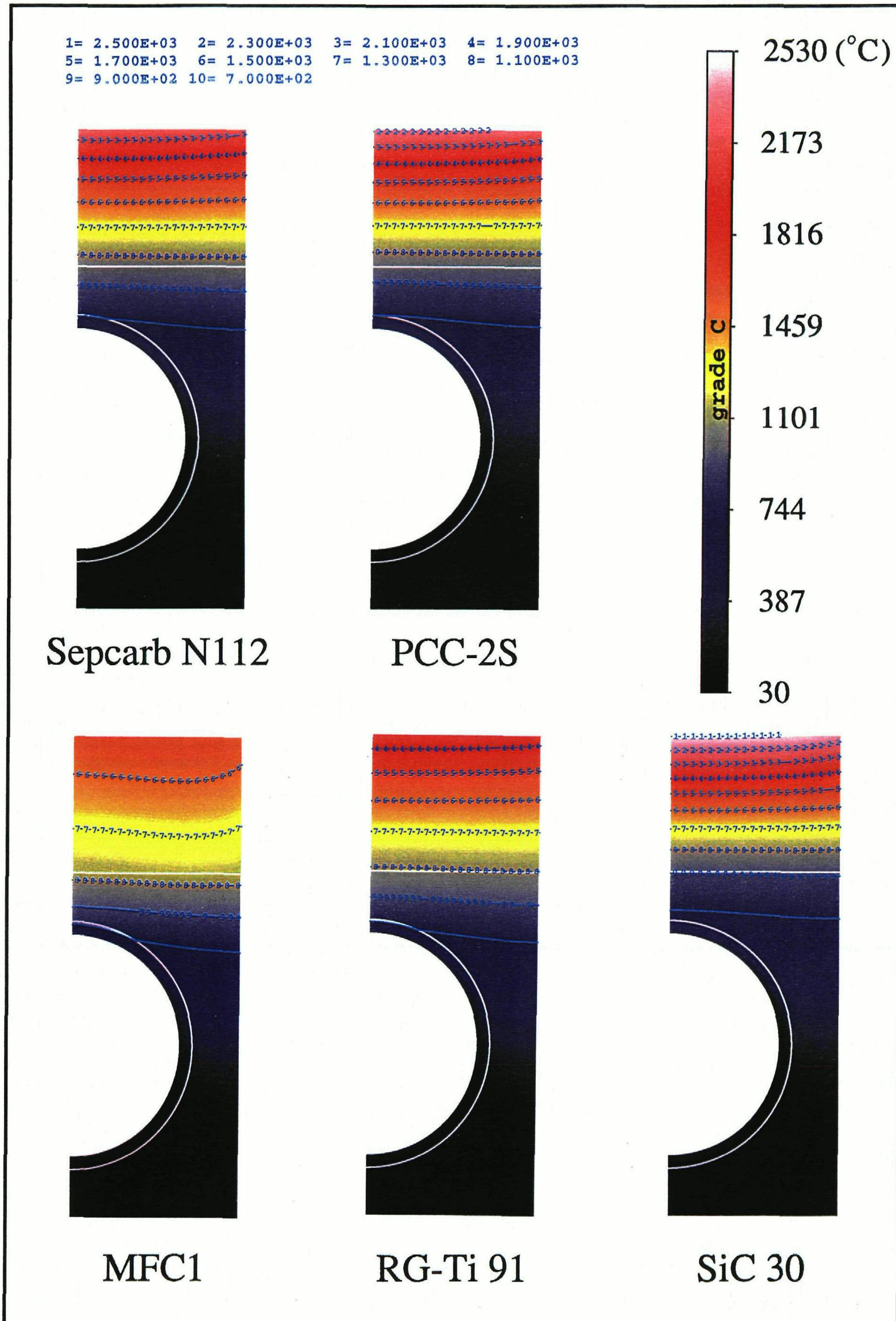

Thermal stress fields
(Sep N112/TZM Mock-up, 10.5 MW/m^2)

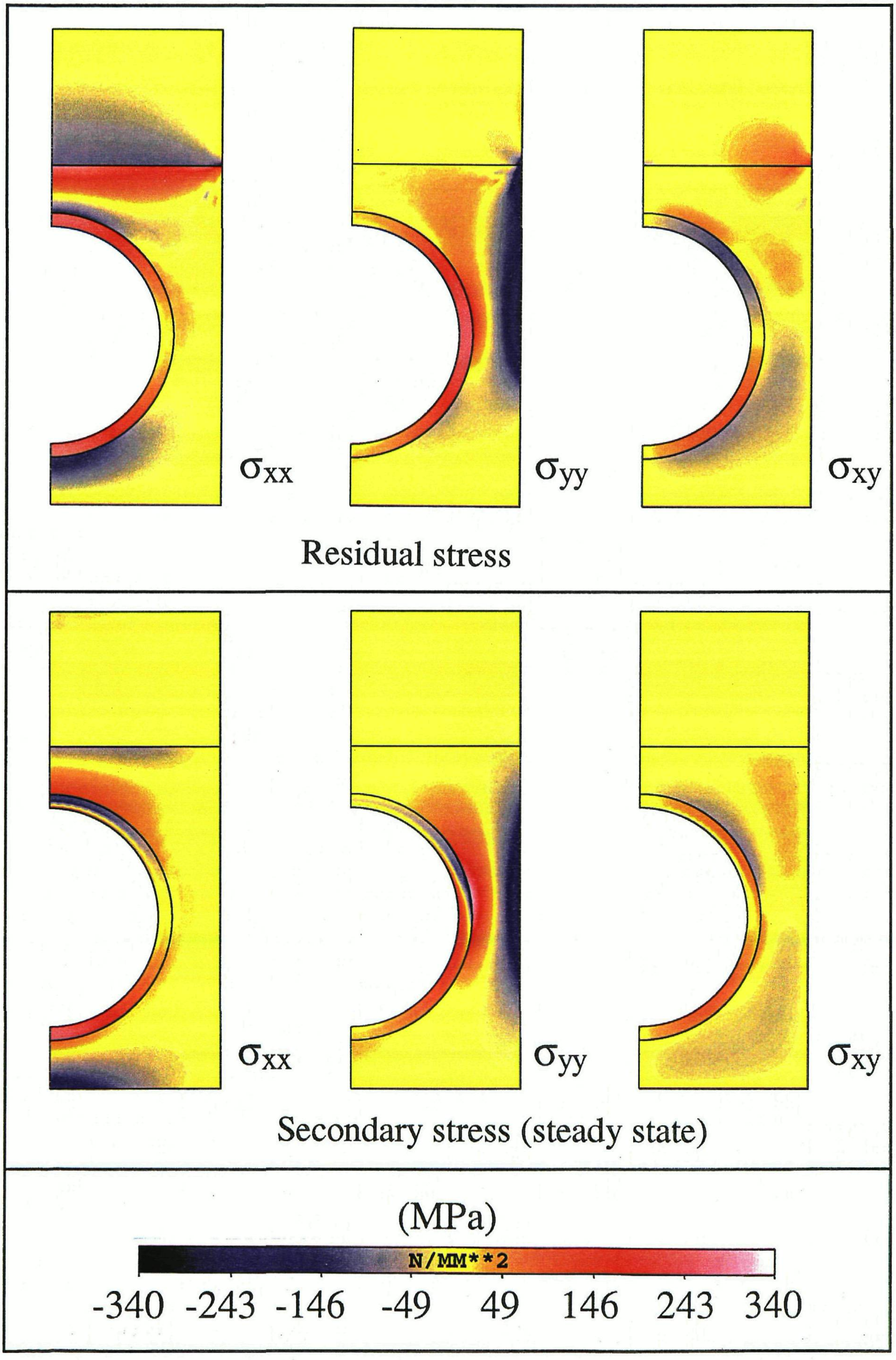

Thermal stress fields - Principal stress
(Sep N112/TZM Mock-up, 10.5 MW/m^2)